

Modeling Voltage Source Converter Interfaced Equipment for Power System  
Harmonic Analysis

by

Bo Gao

A thesis submitted in partial fulfillment of the requirements for the degree of

Doctor of Philosophy

in

Energy Systems

Department of Electrical and Computer Engineering  
University of Alberta

© Bo Gao, 2022

# Abstract

The use of voltage source converter (VSC) has been widely accepted in present power systems for interfacing renewable energy generations, high voltage direct current (HVDC) transmission, flexible alternating current transmission systems (FACTS), and other applications. Due to the converter's power electronic composition, there is a need to evaluate VSC's harmonic impacts using tools such as harmonic power flows and frequency scans. For power system planning, there is a significant need for a harmonic model that can represent the harmonic characteristics of VSC equipment.

This thesis first clarifies the harmonic characteristics of the VSC-interfaced equipment. The main concern regarding VSC-interfaced equipment is their impact on low-order harmonics because such harmonics are more prevalent in current power systems. The main objective of this thesis is to develop models of VSC-interfaced equipment at low-order harmonics based on the response of VSC-interfaced equipment to such harmonics.

This thesis then proposes analytical harmonic models for four types of VSC-interfaced equipment: three-phase VSC, single-phase VSC, doubly-fed induction generator (DFIG), and VSC-HVDC. The results show that all these equipment can be modeled as harmonically coupled impedance matrices. The only exception is the single-phase VSC that has a form of a Thevenin circuit at the 3<sup>rd</sup> harmonic. Methods to determine the model parameters have been developed for each type of equipment. The validity of the proposed harmonic models and the impacts of various VSC

design parameters have been demonstrated using extensive simulation studies and lab experiments. Case studies have demonstrated the effectiveness of the proposed models for harmonic power flow studies.

# Preface

This thesis is an original work by Bo Gao. As detailed in the following, some chapters have been published as scholarly articles, in which Prof. Wilsun Xu is the primary supervisor and has contributed to developing concepts and composing the manuscript. Dr. Yang Wang has contributed to the lab experiments and has also been involved in the discussion and in composing the manuscript.

Chapter 2 and Chapter 3 include submitted papers:

B. Gao, Y. Wang, and W. Xu, "Modeling Voltage Source Converters for Harmonic Power Flow Studies," in *IEEE Transactions on Power Delivery*, vol. 36, no. 6, pp. 3426-3437, Dec. 2021.

B. Gao, Y. Wang, and W. Xu, "An Improved Model of Voltage Source Converters for Power System Harmonic Studies," in *IEEE Transactions on Power Delivery* (early access). doi: 10.1109/TPWRD.2021.3122426

Chapter 5 has been submitted as

B. Gao, Y. Wang, and W. Xu, "An Impedance Matrix of Doubly-fed Induction Generator for Power System Harmonic Analysis," in *International Journal of Electrical Power and Energy Systems*.

# Acknowledgments

I would like to show my sincere gratitude to Dr. Wilsun Xu for his patient guidance, advice, and encouragement throughout my research. It would not have been possible to complete this thesis without his supervision. I will always be proud to say I had the privilege of being his student, and I remain ever grateful to him.

I also want to express my thanks to the other professors from my Ph.D. examining committee, Dr. Yunwei Li, Dr. Gregory Kish, Dr. Venkata Dinavahi, and Dr. Kuo Lung Lian, for reviewing my thesis and providing invaluable comments. Thanks also go to all my colleagues in the PDS Lab, for their kind help, inspiring advice, and friendship. It is my honor to work with these talented and enthusiastic researchers. Special thanks go to Dr. Yang Wang for his selfless help during various stages of this project.

I want to express my gratitude to my parents Jinxu Gao and Hongfeng Gao. There are not enough words to describe how thankful I am to them. Their endless love and great support are what sustained me to the present.

Finally, I dedicate this thesis to my beloved wife, Fangyuan Zhang, who supported me as I pursued a Ph.D., especially during this pandemic period. I would never have made it this far without her love, care, support, and every little effort she is making for me.

# Contents

<b>Chapter 1 Introduction.....</b>	<b>1</b>
1.1 Introduction to VSC Equipment and Associated Harmonic Issues.....	2
1.1.1 Introduction to VSC Equipment .....	2
1.1.2 Harmonic Issues Associated with the VSC Equipment .....	3
1.2 Harmonic Analysis in Power Systems .....	6
1.2.1 Time-domain Harmonic Analysis .....	7
1.2.2 Frequency-domain Harmonic Analysis.....	8
1.2.3 Hybrid Time-Frequency-Domain Harmonic Analysis.....	9
1.3 Harmonic Studies of VSC and Challenges .....	10
1.3.1 Existing Harmonic Studies of VSC Equipment.....	10
1.3.2 Challenges of Harmonic Modeling of VSC Equipment .....	12
1.4 Thesis Scope and Outline.....	13
<b>Chapter 2 Modeling Voltage Source Converters for Power System Harmonic Analysis: Model Development .....</b>	<b>17</b>
2.1 Defining the Problem of Harmonic Modeling of VSC .....	17
2.2 Existing Harmonic Models of VSC .....	18
2.2.1 Analytical Norton Circuit Model.....	19
2.2.2 Analytical Impedance Model.....	20
2.2.3 Frequency Coupling Matrix (FCM) Model .....	21
2.2.4 Norton Model of VSC (Wind Turbine) in IEC Report .....	22
2.3 Harmonic Modeling of the VSC .....	23
2.3.1 Modeling the Impact of the Control Loop .....	26
2.3.2 Modeling the Impact of the Power Loop .....	30
2.3.3 Overall Harmonic Model of the VSC .....	33
2.4 Impact of the PWM on the Developed Model .....	36
2.4.1 Reproduction of the Modulation Signal.....	36
2.4.2 Additional Harmonics Introduced by the PWM .....	38

2.5	Technical Discussions of the Proposed Harmonic model .....	40
2.5.1	Applicable VSC Equipment for the Proposed Model.....	40
2.5.2	Characteristics of Converter Impedance.....	43
2.6	Summary .....	45
<b>Chapter 3 Modeling Voltage Source Converters for Power System Harmonic Analysis: Model Verification and Application.....</b>		<b>47</b>
3.1	Verification of the Proposed Model Via Time-domain Simulations and Lab experiments .....	48
3.1.1	Verification of the Proposed Model Via Time-domain Simulations.....	48
3.1.2	Verification of the Proposed Model Via Lab Experiments .....	49
3.2	Practical Considerations and Simplifications.....	52
3.2.1	Relative Contribution of VSC Operating Segments .....	53
3.2.2	The Impact of the Dc-link Capacitor .....	54
3.2.3	The Impact of the Control Loop .....	57
3.2.4	Strength of the Coupling Effect .....	58
3.2.5	Determination of Model Parameters Using Measurements .....	60
3.3	An Overall Procedure to Construct the Harmonic Model.....	60
3.4	Application of the Proposed Model for Harmonic Power Flow Studies	61
3.5	Summary .....	67
<b>Chapter 4 Extension of the Harmonic Model for Single-phase Voltage Source Converters.....</b>		<b>68</b>
4.1	Harmonic Characteristics of a Single-phase PV system .....	69
4.1.1	Harmonic Response of a Single-phase PV System.....	69
4.1.2	Review of Existing Publications.....	70
4.2	Harmonic Modeling of Single-phase VSC.....	71
4.2.1	abc/dq Conversion in Single-phase VSC .....	71
4.2.2	Modulation Signal of PWM Switching.....	73
4.2.3	Modeling of the Impact of the Power Loop.....	74
4.2.4	Overall Harmonic Model of the Single-phase VSC .....	77
4.3	Verification of the Proposed Model Via Time-domain Simulations .....	80

4.3.1	Verification of Harmonic Impedances at 5 <sup>th</sup> ~29 <sup>th</sup> Harmonics .....	80
4.3.2	Verification of the Thevenin Circuit for the 3 <sup>rd</sup> harmonic .....	83
4.3.3	Impact of the Outer Control Loop .....	86
4.4	Investigation of 3 <sup>rd</sup> Harmonics Produced by VSC in Practical Systems	89
4.5	Summary .....	91
<b>Chapter 5 Modeling Doubly-fed Induction Generators for Power System Harmonic Analysis .....</b>		<b>93</b>
5.1	Review of Harmonic Modeling of the DFIG .....	94
5.2	Operating Characteristics of DFIG .....	95
5.3	Harmonic Model of the DFIG.....	97
5.3.1	Harmonic Coupling Model of RSC and GSC.....	98
5.3.2	Equivalent Harmonic Model of the DFIG .....	105
5.4	Verification of the Proposed Model Via Time-domain Simulations ....	106
5.4.1	Validation of the Proposed Model.....	107
5.4.2	Verification of the Impact of the Dc-link Capacitance .....	108
5.4.3	Significance of the GSC and RSC Block.....	111
5.4.4	Strength of the Coupling Effect Between Different Harmonics ....	112
5.5	Model Verification Based on Lab Experiments .....	113
5.6	Application of the Proposed Model of DFIG for Harmonic Power Flow Analysis.....	116
5.7	An Overall Procedure to Construct a Harmonic Model of the DFIG ...	119
5.8	Summary .....	120
<b>Chapter 6 Harmonic Modeling of the VSC-HVDC for Power System Harmonic Analysis .....</b>		<b>122</b>
6.1	Harmonic Response of the VSC-HVDC .....	122
6.2	Derivation of the Harmonic Model of VSC-HVDC .....	126
6.2.1	Harmonic Model of the VSC-HVDC .....	126
6.2.2	Simplified Model .....	130
6.3	Verification of the Proposed Model Via Time-Domain Simulations ...	132
6.3.1	Verification of the Harmonic Impedance.....	132

6.3.2	Coupling Effect Between Two VSC Terminals .....	133
6.4	An Overall Procedure to Construct the Harmonic Impedance Model of the VSC-HVDC .....	134
6.5	Summary .....	135
<b>Chapter 7</b>	<b>Conclusions and Future Work.....</b>	<b>136</b>
7.1	Thesis Conclusions and Contributions.....	136
7.2	Suggestions for Future Work.....	138
<b>References</b>	<b>.....</b>	<b>140</b>

# List of Tables

Table 3-1 Source of data .....	48
Table 3-2 Measured phase-A impedance of a 2kW VSC under different background harmonics .....	52
Table 3-3 Impact of the dc-link capacitance on the 7 <sup>th</sup> harmonic impedance of the VSC under different dc-link capacitances .....	55
Table 3-4 Parameters of VSC loads .....	62
Table 4-1 Parameters of the studied single-phase PV system.....	80
Table 4-2 3 <sup>rd</sup> harmonic voltage at the PCC obtained using time-domain simulations and the proposed model .....	84
Table 4-3 IHDs of the 3 <sup>rd</sup> harmonic voltage and current involving different dc-link capacitors .....	86
Table 4-4 Parameters of practical single-phase PV systems.....	89
Table 4-5 Range of the voltage source and impedance of the Thevenin circuit ...	89
Table 4-6 Single-phase impedance data collected from various sources.....	90
Table 4-7 3 <sup>rd</sup> harmonic voltage and current at the PCC in practical, single-phase distribution systems .....	90
Table 4-8 Comparisons between the 3 <sup>rd</sup> harmonic currents produced by single-phase and other appliances.....	91
Table 5-1 Parameters of studied DFIG system .....	107
Table 5-2 Comparison between the simulated impedances and calculated impedances of the GSC and RSC ( $Z_{gh,gh}$ and $Z_{rh,rh}$ ) .....	110
Table 5-3 Impact of the dc-link capacitance on the harmonic impedance of the GSC with a dc-link capacitance of 2000 $\mu$ F .....	111
Table 5-4 Impact of the dc-link capacitance on the harmonic impedance of GSC with a dc-link capacitance of 10000 $\mu$ F .....	111
Table 5-5 Measured phase-A impedance of a 3kW DFIG under different background harmonics .....	115
Table 6-1 Parameters of the VSC-HVDC .....	133

# List of Figures

Figure 1-1 Typical structure of two-level three-phase VSC .....	3
Figure 1-2 Waveform of the switching function and its spectrums .....	4
Figure 1-3 Harmonic components of the switching function using different $m_f$ ( $m_f = \omega_c/\omega_1$ ).....	5
Figure 1-4 Harmonic analysis in an exemplary system containing VSC equipment .....	9
Figure 1-5 Equipment that only contains one VSC tied to the grid.....	13
Figure 1-6 Equipment that contains back-to-back VSCs tied to grid .....	14
Figure 2-1 Response mechanism of the VSC to power system harmonics .....	18
Figure 2-2 Norton circuit of the VSC .....	19
Figure 2-3 Small-signal impedance model of VSC .....	21
Figure 2-4 FCM model determination using measurements .....	22
Figure 2-5 Norton circuit model determination using measurements .....	23
Figure 2-6 Structure of a typical two-level, three-phase VSC.....	24
Figure 2-7 The flow of the derivation of the harmonic model for VSC .....	24
Figure 2-8 Illustration of the impact of the dc-link capacitor.....	33
Figure 2-9 Results of the output harmonics for PWM with asymmetrical sampling technique.....	37
Figure 2-10 Harmonic information in VSC considering switching harmonics ....	39
Figure 2-11 The equivalent circuit of a VSC seen from the dc .....	40
Figure 2-12 The equivalent circuit of VSC by assuming the converter is an independent impedance.....	44
Figure 2-13 Calculated converter impedance and corresponding VSC impedance .....	44
Figure 2-14 Equivalent impedance of VSC with the different current control schemes.....	45
Figure 3-1 Studied system for verifying the proposed harmonic model .....	48
Figure 3-2 Comparison between the phase-A harmonic impedances calculated	

using the proposed model and impedances using time-domain simulations .....	49
Figure 3-3 Experimental test of the harmonic impedance of a VSC .....	51
Figure 3-4 Recorded experimental waveforms of phase-A voltage and current at the PCC of VSC when 5% of the 5 <sup>th</sup> , 7 <sup>th</sup> , and 11 <sup>th</sup> harmonics were added.....	52
Figure 3-5 Impact of each operating segment on harmonic impedance .....	53
Figure 3-6 Comparison between the calculated harmonic impedances and simulated harmonic impedances for different dc-link capacitances.....	55
Figure 3-7 Numerical assessment of the impact of the dc-link capacitor.....	56
Figure 3-8 Impact of the outer control loop.....	58
Figure 3-9 Comparison between the diagonal components and nondiagonal impedance in the impedance matrix .....	59
Figure 3-10 Coupling effect in simulations .....	60
Figure 3-11 An industrial system for harmonic power flow studies.....	62
Figure 3-12 Calculated and simulated phase-A voltage and current at the PCC ..	64
Figure 3-13 Calculated and simulated phase-A voltage and current at bus 5.....	65
Figure 3-14 Comparison between the voltage and current spectrum obtained through simulations and the spectrum calculated using the proposed method. ....	66
Figure 3-15 Errors of the spectrum of current at the PCC when assuming the bus 5 load is open .....	66
Figure 4-1 Typical single-phase PV system and the control diagram.....	69
Figure 4-2 Harmonic response of a single-phase VSC.....	70
Figure 4-3 Harmonic model of single-phase VSC.....	79
Figure 4-4 Comparison between the calculated impedances and simulated impedances.....	81
Figure 4-5 Comparison between the calculated impedances for different dc-link capacitors .....	82
Figure 4-6 Harmonic coupling effect in the VSC .....	83
Figure 4-7 Setups for computing the Thevenin circuit .....	84
Figure 4-8 Voltage and current waveforms at the PCC involving different dc-link capacitors .....	85
Figure 4-9 Impedance that connects the harmonic voltage on the dc-link and the	

harmonic current on the ac side of the VSC with the harmonic current at the PCC .....	87
Figure 4-10 Equivalent circuit to compute the 3 <sup>rd</sup> harmonic distortion.....	91
Figure 5-1 Typical DFIG system and the control diagrams of the RSC and GSC	97
Figure 5-2 RSC and GSC response mechanism to the external harmonics .....	97
Figure 5-3 Combined RSC and GSC unit to be modeled. ....	98
Figure 5-4 Equivalent harmonic model of the DFIG system.....	98
Figure 5-5 Flow of the derivation of the harmonic model of RSC&GSC .....	99
Figure 5-6 Equivalent impedance of the whole DFIG.....	106
Figure 5-7 Comparison between the impedances calculated using the proposed model and impedances using time-domain simulations .....	108
Figure 5-8 Comparison between the impedances calculated using the proposed model and the impedances calculated with an infinite dc-link capacitance .....	109
Figure 5-9 The degree of significance of the GSC and RSC impedances .....	112
Figure 5-10 Coupling effect in the GSC .....	113
Figure 5-11 Experimental test of the harmonic impedance of a VSC .....	114
Figure 5-12 Recorded experimental waveforms of phase-A voltage and current at the PCC of the VSC inverter when the 10% 5 <sup>th</sup> , 7 <sup>th</sup> and 11 <sup>th</sup> harmonics were added .....	115
Figure 5-13 Studied system for harmonic power flow .....	116
Figure 5-14 Calculated and simulated phase-A voltage and current at the PCC.	118
Figure 5-15 Calculated and simulated phase-A voltage and current at bus 5.....	119
Figure 5-16 Comparison between the simulated current spectrum and the calculated spectrum ignoring the GSC and RSC .....	119
Figure 6-1 Structure of VSC-HVDC and the control diagram .....	124
Figure 6-2 Harmonic characteristics on the dc side of the VSC-HVDC .....	125
Figure 6-3 Equivalent circuit of VSC-HVDC .....	130
Figure 6-4 Equivalent impedance model of the VSC-HVDC.....	131
Figure 6-5 Simplified decoupled impedance model of the VSC-HVDC .....	132
Figure 6-6 VSC-HVDC system for model verification .....	133
Figure 6-7 Comparisons between the calculated impedances and simulated	

impedances for the VSC-HVDC.....	133
Figure 6-8 Comparison between the impedance of the dc cable and the impedance of the dc-link capacitor .....	134

# List of Symbols

$h_+$	Positive-sequence harmonic order
$h_-$	Negative-sequence harmonic order
$I_{(.)}$	Current
$I_{c1}$	The fundamental frequency current on the ac side of the converter
$I_{ch\pm}$	The harmonic current on the ac side of the converter
$I_{gh\pm}$	The harmonic current at the PCC of a VSC equipment
$V_{(.)}$	Voltage
$V_{g1}$	The fundamental frequency voltage at the PCC of a VSC equipment
$V_{gh\pm}$	The harmonic voltage at the PCC of a VSC equipment
$m_1$	The fundamental frequency component in the modulation signal
$m_{h\pm}$	Harmonic components in the modulation signal
$\theta_{(.)}$	The phase angle of the voltage
$\delta_{(.)}$	The phase angle of the current
$\gamma_{(.)}$	The phase angle of the modulation signal
$C_{dc}$	DC-link capacitor
$L_2$	The inductor of the LCL filter on the converter side
$L_1$	The inductor of the LCL filter on the grid side
$R_{(.)}$	Resistor
$C_f$	The capacitor of the LCL filter
$P_{(.)}$	Active power
$Q_{(.)}$	Reactive power
$Z_{(.)}$	Impedance
$Z_{Lg}$	The impedance of the inductor connected to the GSC
$R_r'$	The rotor resistance of the induction generator referred to the stator side
$X_{lr}'$	The rotor reactance of the induction generator referred to the stator side

$R_s$	The stator resistance of the induction generator
$X_{ls}$	The stator reactance of the induction generator
$X_M$	The magnetizing reactance of the induction generator
$\omega_{(\cdot)}$	Angular frequency
$\omega_1$	Fundamental angular frequency
$\omega_{h\pm}$	Harmonic angular frequency
$\omega_r$	The rotating angular frequency of the induction generator

# List of Abbreviations

VSC	Voltage Source Converter
LCC	Line Commutated Converter
IGBT	Insulated-gate Bipolar Transistor
GTO	Gate Turn-off Thyristor
DFIG	Doubly-fed Induction Generator
HSS	Harmonic State Space
IG	Induction Generator
RSC	Rotor Side Converter
GSC	Grid Side Converter
PMSG	Permanent Magnet Synchronous Generator
PV	Photovoltaic
HVDC	High Voltage Direct Current Transmission
FACTS	Flexible Alternating Current Transmission System
VFD	Variable Frequency Drive
PCC	Point of Common Coupling
PWM	Pulse-width Modulation
FFT	Fast Fourier Transform
DFT	Discrete Fourier Transform
IHD	Individual Harmonic Distortion
PLL	Phase-lock Loop
WT	Wind Turbine
IEC	International Electrotechnical Commission
IHA	Iterative Harmonic Analysis
IPHA	Iterative Harmonic Power Flow
FCM	Frequency Coupling Matrix
EMTP	Electromagnetic Transients Program
EMTDC	Electromagnetic Transients including DC

# Chapter 1

## Introduction

Power electronic equipment has been widely used to meet the evolving requirements of modern power systems. While this equipment provides more efficient control and energy conversion in power systems, it can also lead to concerns about power quality. One of the most significant concerns is harmonic distortion. Therefore, it is necessary to assess the harmonic impact of a power electronic equipment or facility before it can be connected to a power system.

The power electronic converters in service can be broadly classified into two types [1]: a line-commutated converter (LCC) and a voltage source converter (VSC). The LCC is also known as a current source converter (CSC). This type of converter is composed of thyristors. Thus, the LCC's switching process relies on the external circuit. The VSC uses more advanced switching cells such as insulated-gate bipolar transistors (IGBTs) and gate turn-off thyristors (GTOs), for which the switching control operates independently of the external circuit. Due to multiple excellent features such as bidirectional power flow [2] and independent control of the active and reactive power, in recent years, the VSC has become a more attractive choice as the basis of power electronic equipment. Consequently, VSC has been increasingly employed in many energy conversion applications such as variable speed wind turbines (e.g., a doubly-fed induction generator [DFIG] and permanent magnet synchronous generator [PMSG]) [3][4], a PV (photovoltaic) [5], a VSC-based high-voltage direct current (VSC-HVDC) transmission system [6], and a VSC-based variable frequency drive (VFD) [7].

Harmonic analysis of power systems with power electronic equipment requires a computer model of the equipment that shows their harmonic characteristics. Harmonic models of LCCs for harmonic analysis have been established through extensive research conducted from 1990-2010 [8]-[14]. The consensus at present is

that the LCC equipment can be modeled adequately using harmonic current sources. A more advanced model for LCC equipment is the harmonically coupled Y-matrix model [15]. However, harmonic models for VSC equipment are still being researched and developed, and few harmonic models of the VSC have been proposed. The harmonic characteristics of the VSC are quite different from that of the LCC due to the different switching and control schemes, and a new type of harmonic model that represents the harmonic features of VSC equipment is needed. In response to this need, this thesis will present a mathematical analysis of the harmonic characteristics of various types of VSC equipment. And accordingly, harmonic models for several types of VSC equipment that can be used to conduct harmonic analysis in power systems will be developed.

In this chapter, the VSC equipment and associated harmonic issues are introduced in Section 1.1. Section 1.2 looks at the techniques that can be used to conduct harmonic analysis in power systems. In Section 1.3, harmonic studies of VSC equipment in existing publications are reviewed, and the challenges for modeling VSC equipment are outlined. Finally, Section 1.4 summarizes the scope and outline of this thesis.

## **1.1 Introduction to VSC Equipment and Associated Harmonic Issues**

This section presents a brief introduction to the VSC equipment in power systems and the harmonic issues associated with VSC equipment.

### **1.1.1 Introduction to VSC Equipment**

In present power systems, VSCs of different topologies, including two-level VSCs [16] and multiple-level VSCs [17][18], are applied in power electronic equipment. The associated types of harmonics of the two-level VSC and multiple-level VSC are almost the same if the floating or unclamped dc-link capacitor of the multiple-level VSC are well balanced [19]. Hence, the most commonly used two-level VSC can be studied to reveal the harmonic features of general VSCs. The

typical configuration of a two-level, three-phase VSC is presented in Figure 1-1 [20]-[21]. As the figure shows, a three-phase VSC consists of six GTO or IGBT switches, which are turned on and off by the pulse-width modulation (PWM) control technique. The control block of the VSC generates the switching function that drives the switching activities. A filter in the form of L, LC, or LCL is connected on the ac side of the VSC to attenuate the harmonics produced by the VSC [22]. The VSC contains a capacitor on the dc side of the VSC to maintain the dc-link voltage. Note that a dc system is also connected to the dc-link capacitor of the VSC, and the dc system varies for different types of VSC equipment. For example, for a PV system or a VSC-based dc motor, the dc system on the other side of the dc-link is the PV panel or a dc motor. In other VSC equipment, such as PMSG, DFIG, and VSC-HVDC, another VSC is connected to the dc-link capacitor, forming the configuration of back-to-back VSCs.

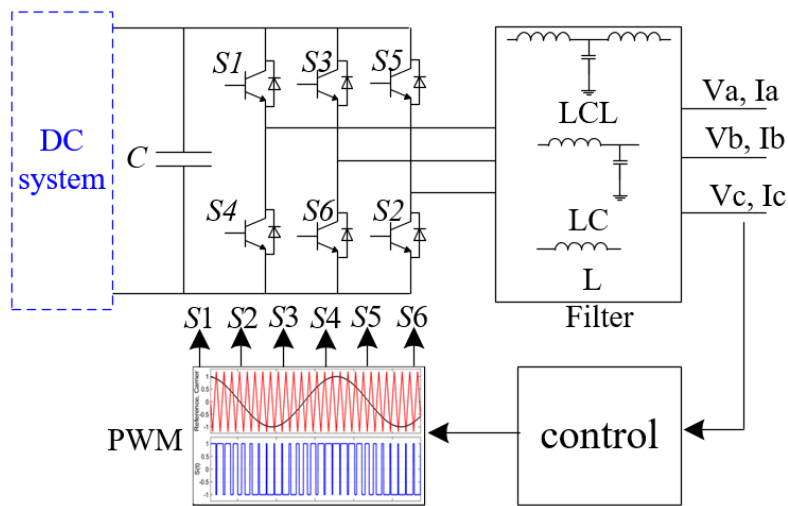


Figure 1-1 Typical structure of two-level three-phase VSC

### 1.1.2 Harmonic Issues Associated with the VSC Equipment

To understand the harmonic characteristics of the VSC, it is essential to understand the types of harmonics associated with VSC equipment. There are three types of harmonics:

- **Switching harmonics**

The primary harmonic emission of the VSC is the switching harmonics that are introduced by the high-frequency PWM switching. The PWM switching function can be established through the double Fourier algorithm [23], as shown in (1.1).

$$S(t) = M \cos(\omega_1 t + \theta_1) + \sum_{\substack{m=1 \\ (\text{even})}}^{+\infty} \sum_{n=\pm 1}^{n=\pm\infty} \frac{4}{m\pi} \times J_n \left( \frac{m\pi M}{2} \right) \times \sin \left( \frac{(m+n)\pi}{2} \right) \times \cos(m(\omega_c t + \theta_c) + n(\omega_1 t + \theta_1)) \quad (1.1)$$

where  $M$  is the modulation index (the ratio of the modulation signal magnitude over the carrier signal magnitude);  $\omega_1$  and  $\omega_c$  are the angular frequencies related to the reference signal and carrier signal, respectively;  $\theta_1$  and  $\theta_c$  are the angles related to the modulation signal and carrier signal, respectively; and  $J_n$  is the Bessel function of the first kind. As noted in (1.1), the main harmonic components in the switching function are the sidebands of multiples of the switching frequency, as shown in Figure 1-2. As a result, the switching harmonics are at very high frequencies (e.g., 2kHz~150kHz) [24]. Due to the high frequencies, the switching harmonics are significantly attenuated by the front-end passive filter, and their propagation to the system is significantly impeded due to the large series impedance. Currently, there is no consensus on whether the switching harmonics pose a significant concern in terms of the power quality [25][26].

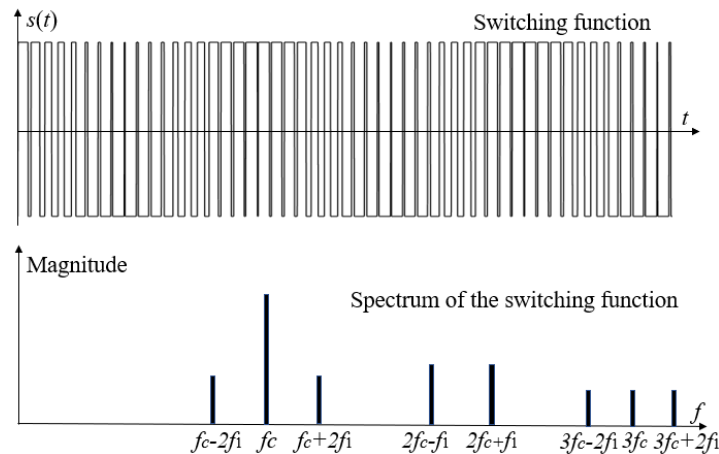


Figure 1-2 Waveform of the switching function and its spectrums ( $f_c$  is the switching frequency and  $f_i$  is the fundamental frequency)

- **Low-order harmonics**

Low order harmonics refer to harmonics produced by conventional nonlinear equipment (e.g., 3<sup>rd</sup>~39<sup>th</sup> harmonics). They are the most common harmonics encountered in present power systems. As shown in (1.1), the primary harmonic emission of the VSC is high-frequency switching harmonics. The emission does not contain low-order harmonics. To check the low-order harmonics in the switching function, the fast Fourier transform (FFT) is applied to the switching function for different switching frequencies. The results are shown in Figure 1-3. The figure shows that the low-order harmonics are almost negligible, which suggests that the VSC does not act as a harmonic source at traditional low-order harmonics.

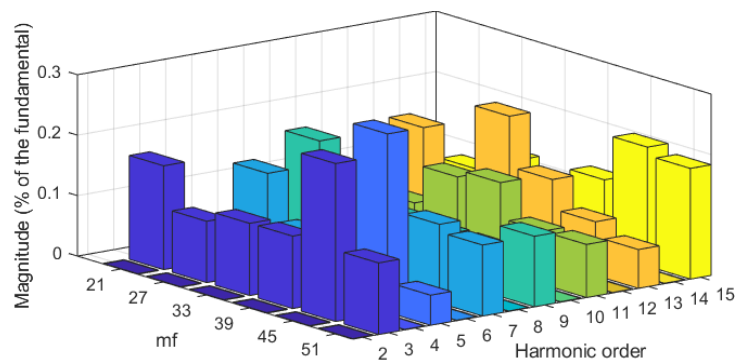


Figure 1-3 Harmonic components of the switching function using different  $m_f$  ( $m_f = \omega_c / \omega_1$ )

Although the VSC does not produce low-order harmonics, it may amplify or attenuate the low-order harmonics that already exist in the power system by interacting with the connected grid. The VSC may even lead to an unexpected harmonic resonance by changing the frequency response of the system. Therefore, it is essential to understand how the VSC responds to low-order harmonics.

- **Non-characteristic harmonics**

The VSC equipment may also produce some non-characteristic harmonics. A typical example is the 3<sup>rd</sup> harmonics induced by the unbalanced voltage of the interconnected grid. The primary mechanism of non-characteristic 3<sup>rd</sup> harmonics is that the unbalanced voltage will cause a double-frequency oscillation power on the

ac side, and because of the power balance between the ac side and dc side, there will be 2<sup>nd</sup> harmonics in the dc voltage [27]. The dc voltage is converted to ac voltage by

$$V_{ac}(t) = S(t) \bullet V_{dc}(t) \quad (1.2)$$

where  $V_{dc}(t)$  is the dc-link voltage. The fundamental frequency components in the switching function and the 2<sup>nd</sup> harmonic in the dc voltage will lead to 3<sup>rd</sup> harmonics in the voltage on the ac side of VSC equipment. The 3<sup>rd</sup> harmonic induced by unbalanced voltages is a positive/negative sequence, which is different from the conventional zero-sequence 3<sup>rd</sup> harmonics [27]. Additionally, the unbalance of harmonics in the supplied voltage will lead to other non-characteristic harmonics. Generally, the unbalanced level is not very significant, especially in transmission systems, so the non-characteristic 3<sup>rd</sup> harmonic is quite small. Therefore, non-characteristic harmonics are not a significant concern in most cases.

In view of the above-mentioned harmonics and industrial needs, this thesis will focus on the research about the model of the VSC at traditional low-order harmonics because: 1) the low-order harmonics have significant impacts on power systems; 2) there are lots of nonlinear loads that produce traditional low-order harmonics; and 3) how the VSC equipment interact with the grid to influence the harmonic distortions in power systems is a critical concern. Consequently, this thesis will investigate the harmonic response of the VSC to external low-order harmonics and build a model that can be used for harmonic power flow analysis. Unless otherwise specified, the term harmonic refers to conventional low-order harmonics in the rest of this thesis.

## 1.2 Harmonic Analysis in Power Systems

Power system harmonic analysis is used to determine the harmonic impact of different power equipment on a power system. Harmonic analysis has been widely used for system planning, equipment design, troubleshooting, and so on. Mainly, the most common applications of power system harmonic analysis are [28]:

- Verifying compliance with harmonic limits.
- Determining harmonic distortion levels for equipment selection.
- Designing harmonic mitigation measures such as harmonic filters.
- Checking if dangerous parallel resonance exists for a given network configuration.

There are two main aspects of concern for harmonic analysis. The first is to determine the frequency response of a system, which will verify whether there are resonance conditions and what can be changed to avoid the resonance. The second is to compute the harmonic voltage and current in a network, to verify if harmonic limits are complied with, and to determine the ratings of the equipment to be installed. Broadly, the approaches used for power system harmonic analysis can be categorized into three types: time-domain techniques, frequency-domain techniques, and hybrid time-frequency-domain techniques [14].

### **1.2.1 Time-domain Harmonic Analysis**

Time-domain harmonic analysis has been extensively used in power systems for decades. This type of method can be conducted using the conventional Brute Force solution [29], which is widely accepted by software tools such as the Electromagnetic Transients Program (EMTP) and Electromagnetic Transients including DC (EMTDC). The voltage and current waveforms are recorded in the time-domain simulations and are used to compute the harmonic contents by the FFT or discrete Fourier transform (DFT) algorithm. The main problem for Brute Force simulations is that they need to wait for the transient to die out before reaching the steady state [30], which is time-consuming, especially for power systems without sufficient damping. Some methods that use iterations to obtain the periodic steady-state solutions are detailed in other publications, which can achieve faster solutions. Typical examples include the Numerical Differentiation Method (ND) [31], Direct Approach Method (DA) [32], Enhanced Numerical Differentiation Method (END) [33], Discrete Exponential Expansion Method [34],

and Sensitivity Circuits [35]. In these techniques, the complete transient is not computed; thus, a faster solution can be achieved [36].

### 1.2.2 Frequency-domain Harmonic Analysis

Frequency-domain harmonic analysis is a direct and simple method that gives solutions at a specific harmonic or frequency. The main frequency-domain harmonic analysis technique is harmonic power flow, which can be carried out using both noniterative and iterative methods. The simplest and most commonly used noniterative method is the direct approach that presents the harmonic penetration to the linear components or systems [14], [37]. In this method, the harmonic current source model of the conventional LCC-based power electronic equipment, which is determined by the fundamental frequency current and the harmonic features of the nonlinear equipment, is applied [37], as shown in Figure 1-4. Other equipment, such as the generator, the transmission line, the transformer, and the linear load, are modeled as impedance. As a result, the nodal harmonic voltage can be computed as

$$V_h = [Y]^{-1} I_h \quad (1.3)$$

where  $V_h$  represents the nodal voltage,  $I_h$  represents the harmonic current vector, and  $[Y]$  represents the admittance of the network. A more advanced noniterative technique proposed in recent years is to apply the coupled Y matrix for the LCC equipment [15]. In this method, the effect of the harmonic voltage on the harmonic current of the nonlinear LCC equipment is also included. Consequently, the results are more accurate.

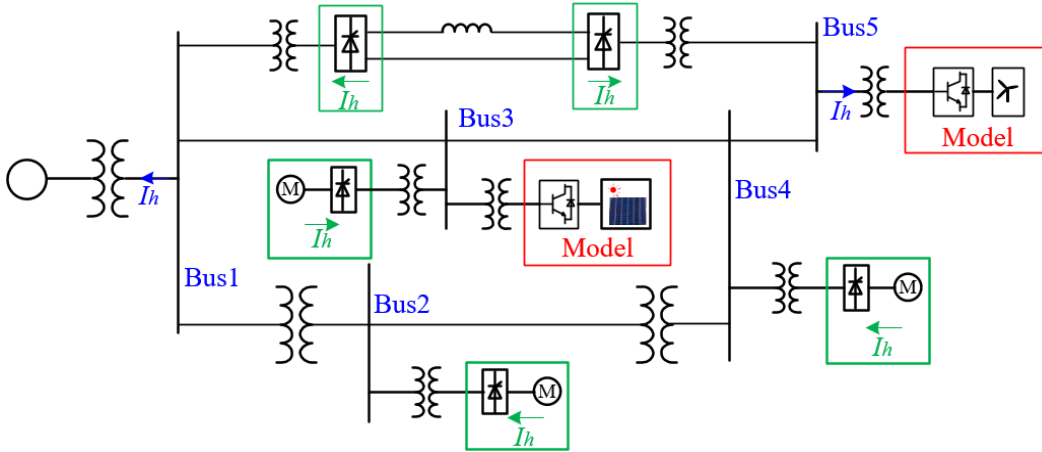


Figure 1-4 Harmonic analysis in an exemplary system containing VSC equipment

Harmonic analysis can also be conducted using the iterative harmonic analysis (IHA) [38][39] or the iterative harmonic power flow (IHPF) methods [40]-[43]. In the IHA methods, the voltage-dependent harmonic current sources are approached using iterations. In each iteration, the nonlinear loads are represented using a constant harmonic current source (same as in Figure 1-4); then the nodal voltage can be computed in the same way as that in the noniterative method. The obtained harmonic voltage is further used to correct harmonic current sources until the changes in harmonic currents are sufficiently small. The main drawback of the IHA is its slow convergence characteristic and narrow stability margin [14], which has limited its application to solving practical power systems. The IHPF methods, on the other hand, take the voltage-dependent nature of the nonlinear components into consideration and solve the harmonic voltage and current equations simultaneously using linearization approaches. The complete IHPF approach is numerically robust and has a good convergence [44]. But the formulation of this method is relatively complex, especially in a large-scale system.

### 1.2.3 Hybrid Time-Frequency-Domain Harmonic Analysis

The hybrid time-frequency-domain harmonic analysis takes advantage of both the time-domain harmonic analysis and frequency-domain harmonic analysis [14]. This method allows the linear components to be modeled in the frequency domain and the nonlinear components modeled in the time domain. The harmonic voltages

on the buses where the nonlinear loads are connected can be obtained using the iterative method. The formulation of the hybrid harmonic analysis is detailed in [45][46].

Among the above-described methods, the harmonic power flow method is the most preferred selection due to its simplicity and rapidity, especially considering that the harmonic models of conventional LCC equipment have been established for this type of method. Therefore, this thesis aims to propose a harmonic model of the VSC equipment that can be integrated into the harmonic power flow tools.

### **1.3 Harmonic Studies of VSC and Challenges**

A harmonic model of the VSC that can be integrated into the above-described harmonic analysis techniques is required to assess the harmonic impact of the VSC, as shown in an exemplary VSC-involved system in Figure 1-4. Once the harmonic model of the VSC is obtained, the harmonic distortions at different buses in the network can be computed by combining the developed harmonic model of VSC-based equipment, the harmonic models of LCC-based nonlinear loads, and other linear loads. In this section, existing work on the harmonic studies of VSC is first presented, and then the challenges on harmonic modeling of VSC equipment are outlined.

#### **1.3.1 Existing Harmonic Studies of VSC Equipment**

To date, modeling the VSC for harmonic studies has been investigated by numerous publications. Typical examples are the small-signal impedance model and the small-signal state-space model of VSC that are widely accepted for harmonic resonance and instability studies [47]-[49]. These methods can hardly be directly implemented for steady-state harmonic distortion assessment because of their small-signal nature. By omitting the nonlinearities of the VSC, the impedance model might be applied for harmonic analysis. For example, an analytical Norton model was proposed in [50], and the harmonic current source of the Norton circuit was directly omitted, leading to a harmonic impedance model for harmonic analysis.

But the justification for ignoring the source was not provided. More importantly, the existing harmonic impedance models were primarily established based on the assumption that the dc-link voltage is harmonic free (i.e., the dc-link capacitor is infinite) [50]-[53]. In practice, the dc-link voltage also experiences harmonic ripples which are introduced by the penetration of the ac side harmonics through the switching process. The harmonic-distorted dc-link voltage, in turn, affects the harmonics on the ac side of the VSC again through the switching process. As a result, the harmonic ripples on the dc-link will affect the harmonic impedance of the VSC equipment. The problem becomes more complex when there are back-to-back VSCs. Analytical justifications are needed to determine how the harmonic ripples affect the harmonic models of two VSCs.

Some methods have also been proposed specifically to model the VSC equipment for harmonic distortion assessment in VSC-involved power systems. One typical example is the VSC models in the harmonic domain [54]-[56]. This type of method combines the three-phase power-flow mismatches and the dc-side current mismatches to characterize a PWM converter through the Newton iterative formulations. Other representative examples include an iteration-based method to include the VSC equipment [55]-[58], a harmonic state-space (HSS) model of VSC equipment [59][60], and a frequency coupling matrix (FCM) model [61]-[63]. The main problem with the harmonic-domain models, iteration-based methods, and HSS methods is that they are very complex and will face computational challenges when implemented for large-scale power systems. Moreover, these methods provide no insights into the harmonic response of the VSC equipment. For example, these methods cannot show the mechanism of the harmonic coupling inside the VSC equipment. The harmonic coupling model in [62][63] is closer to what is needed for power system harmonic analysis. However, [62][63] just investigated the harmonic-coupling effects through measurements, which did not provide an analytical explanation for the harmonic coupling.

In parallel with the above work, an IEC committee suggested using measured harmonic current source models to represent the VSC-based wind turbines [64].

However, this method has been reported to be inaccurate [65]. A recent IEC report suggested using a Norton equivalent model to improve the accuracy [65]. Doing so requires measuring the model parameters. However, the report does not provide technical justifications for this recommendation, and as a result, there is no assurance that the method will always work. In summary, a model that fully represents steady-state harmonic characteristics of the VSC equipment still needs to be developed.

### **1.3.2 Challenges of Harmonic Modeling of VSC Equipment**

Although, as mentioned above, there are some harmonic models for VSC equipment, they haven't solved every problem. The main challenges preventing a complete analytical harmonic model are summarized here:

- Various functional segments of the VSC determine the harmonic response of the VSC equipment to low-order harmonics. The filter, the control block including the inner and outer control loops, the dc-link capacitor, and the dc system connected to the dc-link capacitor jointly determine the harmonic characteristics of the VSC. More importantly, the impacts of these segments may affect each other, so combining the effects of all these segments is challenging.
- The PWM switching does not produce any low-order harmonics in the connected system, but it may affect the harmonic characteristics of the VSC. An issue that needs to be addressed is how to analyze the impacts of the PWM on the harmonic model of the VSC.
- In equipment that contains back-to-back VSCs, the harmonic ripples in the dc-link voltage may affect the harmonic model of the VSC. Furthermore, because two VSCs share the same dc-link, a harmonic coupling effect may exist between VSCs. Therefore, it is important to assess the impacts of the dc-link capacitor on quantifying the models of VSCs.
- It can be challenging to determine how to integrate the developed harmonic

model into the existing harmonic analysis techniques. What types of harmonic analysis techniques can be used depends on the characteristics of the harmonic model.

- The internal parameters of practical VSC equipment may not be attainable. In such cases, how to obtain the harmonic model of VSC equipment can be challenging.

In summary, there are many unsolved issues and challenges in the harmonic modeling of VSC equipment. Novel methods are needed to overcome the challenges and establish a sound harmonic model of VSC equipment.

#### 1.4 Thesis Scope and Outline

The purpose of this thesis is to propose harmonic models of VSC equipment. Considering that the harmonic characteristics of VSC equipment might be different, various harmonic models may need to be established. A number of tasks need to be accomplished in this thesis:

- 1) The first task is to develop an analytical harmonic model for three-phase VSC equipment and integrate the harmonic model to conduct harmonic power flow studies. The proposed harmonic model is expected to be suitable for equipment that only contains one VSC terminal or back-to-back VSCs, but only one VSC is exposed to grid harmonic sources (i.e., only one VSC is connected to the grid), as shown in Figure 1-5. This type of harmonic model can be suitable for the three-phase PV system, PMSG, as well as VSC-VFD.

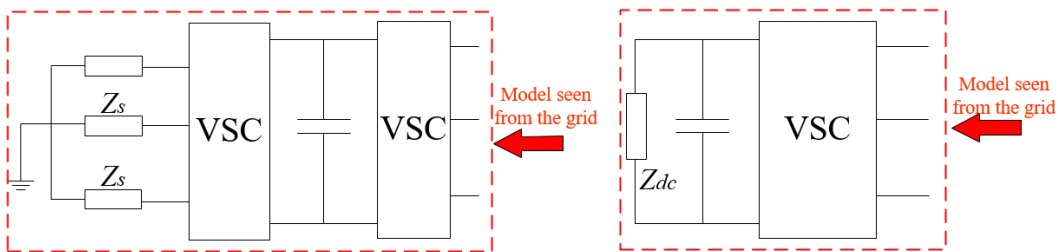


Figure 1-5 Equipment that only contains one VSC tied to the grid

- 2) The second task is to develop an analytical harmonic model for single-phase VSC equipment and integrate the harmonic model to conduct harmonic power flow studies. The unique harmonic features of the single-phase VSC need to be characterized. The main application of such a model will be to assess the harmonic impacts of the single-phase PV in distribution systems.
- 3) The third task is to develop an analytical harmonic model for equipment containing back-to-back VSCs and integrate the harmonic model to conduct harmonic power flow studies. This type of equipment includes the back-to-back VSCs, both of which are exposed to the grid harmonic sources, as shown in Figure 1-6. The proposed harmonic model is expected to be applied in DFIG and VSC-HVDC.

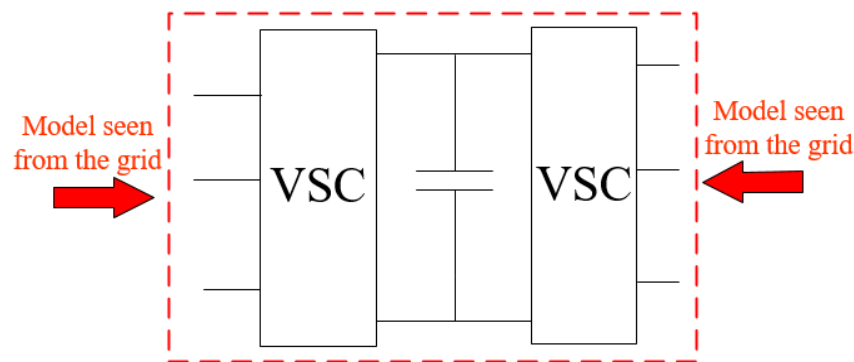


Figure 1-6 Equipment that contains back-to-back VSCs tied to the grid

The following paragraphs summarize the organization of the thesis and describe the main topics and research in each chapter.

Chapter 2 investigates the characteristics of the harmonic response of a two-level, three-phase VSC, and an analytical harmonic model of the three-phase VSC is developed accordingly. In this harmonic model, both the impacts of the control loop and the power loop (i.e., the effect of the dc-link) are established through mathematical derivations. The impacts of the dc system connected to the dc-link capacitor are also discussed. The final results have shown that the three-phase VSC can be represented using a harmonically coupled impedance matrix. The robustness of the proposed model for different PWM switching frequencies is validated in this

chapter. Based on the obtained model, the characteristics of the independent converter impedances are featured.

In Chapter 3, the proposed harmonic model of the three-phase VSC in Chapter 2 is verified through time-domain simulations. The time-domain simulation results show that the proposed model is very accurate. The impact of the power loop has been extensively investigated; it shows that a larger dc-link capacitor will lead to a less noticeable impact on the harmonic impedance of the VSC. The main finding that the three-phase VSC can be modeled using a harmonic impedance is validated using lab experiments. The application of the proposed model for harmonic power flow studies in a VSC-involved power system is also verified via time-domain simulations. Based on extensive studies of the proposed model, the chapter includes a proposal for a practical approach to constructing the developed model.

Chapter 4 extends the proposed model of the three-phase VSC to a single-phase VSC. The single-phase VSC acts as a harmonic source for the 3<sup>rd</sup> harmonic, and it can be modeled as a Thevenin circuit for the 3<sup>rd</sup> harmonic. For other harmonics, the single-phase VSC acts as a harmonically coupled impedance matrix. The proposed model is validated using time-domain simulations. The 3<sup>rd</sup> harmonic distortion caused by a practical single-phase VSC is detailed and compared with other appliances.

Chapter 5 and Chapter 6 focus on the harmonic modeling of the DFIG and VSC-HVDC, which contain back-to-back VSCs. In Chapter 5, the harmonic model of the back-to-back converters is modeled through rigorous mathematical derivations. The back-to-back VSCs can be represented using a coupled impedance matrix which includes the coupling effect between two VSCs and the coupling effect between different harmonics. Further studies show that the coupling effect between different harmonics can be omitted, and the back-to-back VSCs can be represented using a  $2 \times 2$  impedance matrix. This model applies to the rotor side converter (RSC) and grid side converter (GSC) in the DFIG. After integrating the model of RSC and GSC with the linear harmonic model of the induction generator, an impedance model of DFIG at harmonics is obtained. Chapter 6 extends the harmonic model of

the back-to-back VSCs to the VSC-HVDC. The harmonic characteristics of the VSC-HVDC are different from that of the back-to-back RSC and GSC due to the dc transmission line. A long transmission line is usually used, which makes the harmonic coupling between two VSC terminals of the VSC-HVDC very weak. Therefore, two VSC terminals can be decoupled from the dc link. Consequently, the developed harmonic model of the three-phase VSC can be applied for the VSC terminal of VSC-HVDC with confidence.

Chapter 7 contains the main conclusions and suggestions for future research in this field.

## Chapter 2

### Modeling Voltage Source Converters for Power

### System Harmonic Analysis: Model Development

A dramatic penetration of voltage source converter (VSC) equipment into the present power system has resulted in concerns about the harmonic impact of the equipment. To evaluate VSC's effects on low-order harmonics, a model for harmonic analysis is needed. Since the VSC does not produce low-order harmonics, the model is needed to reveal the VSC's response to external harmonics. In this regard, the harmonic model of the VSC can be developed based on the harmonic response mechanism of a VSC, which includes the impacts of both the control function and the ac/dc harmonic interaction (power loop). In this chapter, the mechanism of the harmonic response of a VSC will be explained. The existing harmonic models of VSC are also reviewed. The latter part of the chapter describes a new analytical harmonic model of the VSC developed through mathematical derivations.

This chapter is organized as follows. Section 2.1 describes the problem of harmonic modeling of a VSC. Section 2.2 presents the existing harmonic models of VSC for harmonic analysis. Section 2.3 details the mathematical derivation of the harmonic model. The impact of the PWM on the proposed harmonic model is investigated in Section 2.4. Some technical discussions on the proposed harmonic model are discussed in Section 2.5. Section 2.6 is the chapter summary.

#### 2.1 Defining the Problem of Harmonic Modeling of VSC

The VSC's response to external harmonics can be described using Figure 2-1. The VSC responds to power system harmonics in the form of two feedback loops: the control loop and the power loop. The control loop establishes the modulation

signal for (pulse-width modulation) PWM switching. Since this loop takes the voltage and current at the point of common coupling (PCC) as inputs (i.e.,  $v_g$  and  $i_g$ ), the modulation signal ( $m$ ) and the resulting switching function will be affected by the ac side harmonics. The power loop represents the harmonic interaction between the dc-link voltage ( $V_{dc}$ ) and the ac-side voltage of the converter ( $v_c$ , “c” stands for the converter). The harmonic current on the ac side can propagate into the dc side through the power electronic switches via the switching function, leading to harmonic ripples in the dc-side current. The dc-side harmonic current leads to harmonic ripples in the dc-link voltage. This distorted dc-link voltage, in turn, can affect the harmonic voltage on the ac side of the VSC. Both the control loop and power loop must be taken into account to develop an accurate VSC harmonic model, i.e.,  $i_{g1} \& i_{gh} = f(v_{g1} \& v_{gh})$ , where subscript “1” and “h” stand for components at the fundamental frequency and the harmonic frequency, respectively.  $v_{gh}$  and  $i_{gh}$  represent all harmonic voltage and current from the grid side.

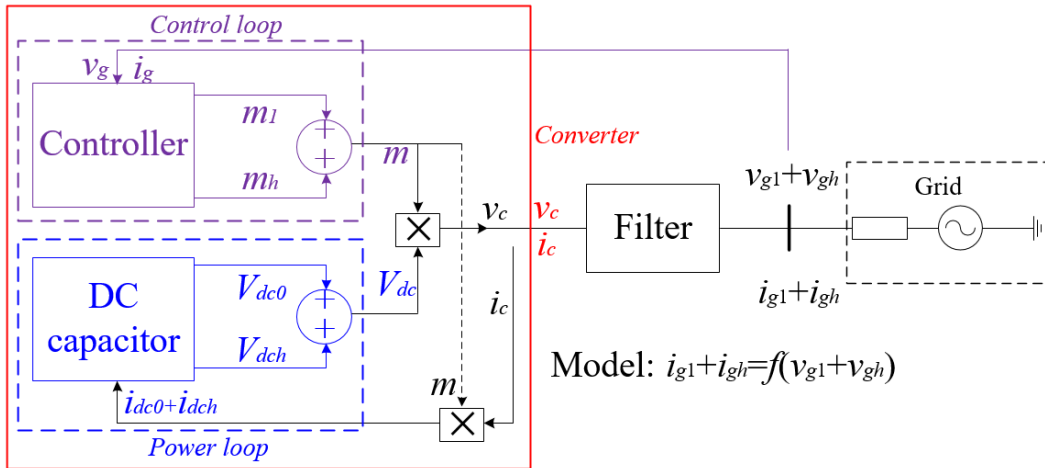


Figure 2-1 Response mechanism of the VSC to power system harmonics

## 2.2 Existing Harmonic Models of VSC

The harmonic model of VSC equipment can be established based on the harmonic response in Figure 2-1. Currently, there are analytical harmonic models and measurement-determined harmonic models of VSC equipment proposed for harmonic analysis. Representative analytical models include the Norton circuit

model and the impedance model, and representative measurement-determined harmonic models include the frequency coupling matrix (FCM) model and the Norton model by the International Electrotechnical Commission (IEC). These methods are introduced in the following.

### 2.2.1 Analytical Norton Circuit Model

Based on the control loop in the VSC's harmonic response to the external harmonics, an analytical Norton circuit model of the VSC that can be used to conduct harmonic analysis in VSC-interfaced systems is proposed in [50]. The basic idea of this model can be explained in Figure 2-2. As shown, the outer control loop yields the reference current for the inner current control loop, and the harmonic component in the reference current is taken as a current source. In contrast, the inner control loop defines an impedance that correlates the harmonic current and voltage on the ac side of the VSC. As a result, the VSC seen from the ac side can be represented as a Norton circuit. This Norton model is a linear harmonic model that can be easily integrated into the harmonic analysis techniques. But there are a few drawbacks. The first is that the model does not take the power loop into consideration and, as a result, fails to reveal the complete harmonic characteristics. The second is that the outer control loop is taken as a harmonic current source but is directly ignored without further justifications. In fact, the current source of the Norton circuit ( $i_{ref}$ ) is not independent of the voltage and current ( $v_c, i_c$ ) on the ac side of the VSC. Therefore, the assumption that the outer control loop behaves as a harmonic current source might be inaccurate.

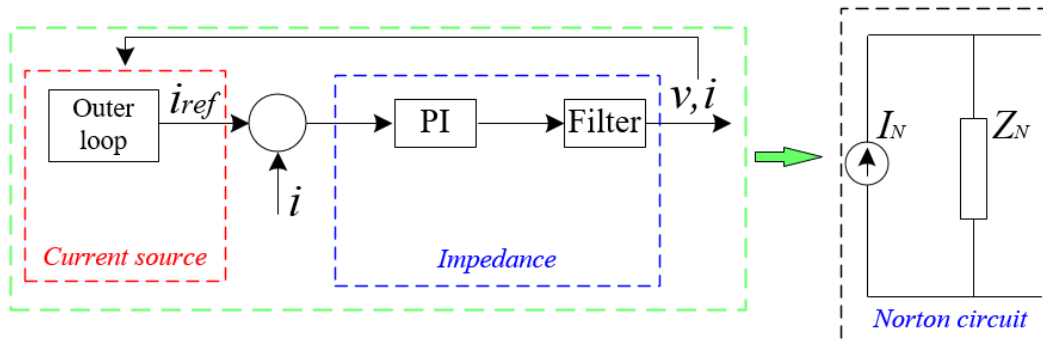
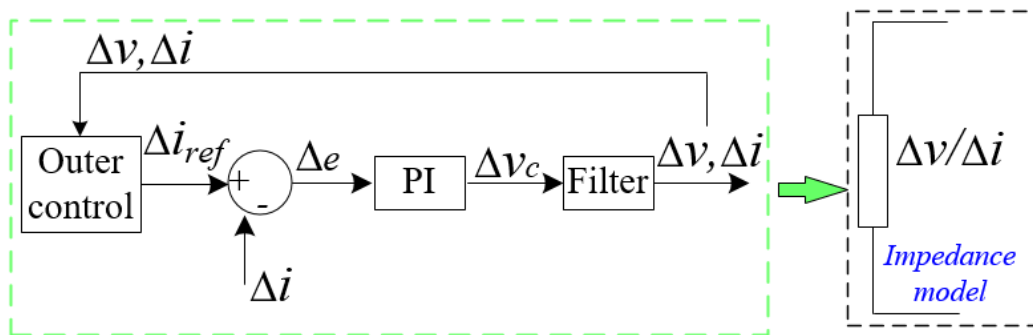


Figure 2-2 Norton circuit of the VSC

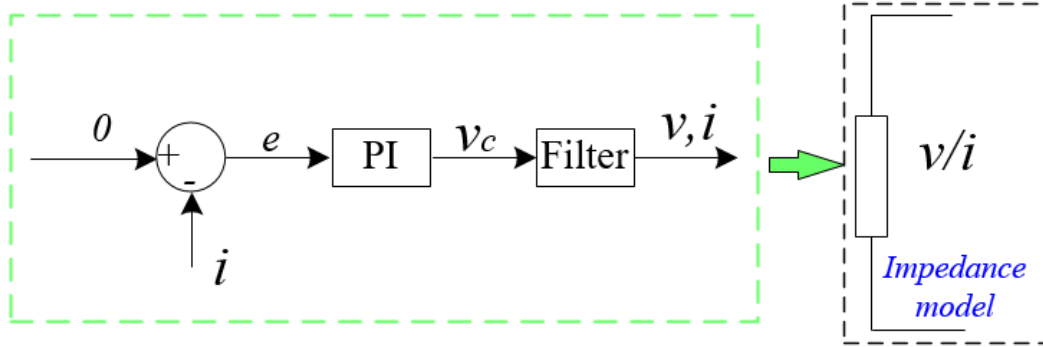
### 2.2.2 Analytical Impedance Model

The impedance model has been widely accepted as representing the VSC for harmonic studies in existing publications. Two types of impedance models have been used for harmonic studies of VSC. The first is the small-signal impedance model [47]-[52]. It can be established upon the small-signal representation of the control loop, as shown in Figure 2-3 (a). The main advantage of this method is that it can include the impact of the outer control loop and take the phase-lock loop (PLL) impact into consideration to accurately show the VSC's response to small-signal disturbance. Still, this impedance method overlooks the effect of the power loop and, as a result, the model fails to reveal the impact of the VSC's dc-link on the harmonic response. Another problem with this small-signal method is that it cannot be integrated into harmonic power flow tools, especially for those non-iterative methods that need a linear model.

The second type of impedance model is the linear model that only considers the inner current control loop of the VSC while the outer control loop is omitted [53], as shown in Figure 2-3 (b). The outer control loop of this model has a much slower response, which means it is not involved with the harmonic analysis. The harmonic voltage and current on the ac side of the VSC have a linear relationship through the inner current control loop. Consequently, the VSC has a linear impedance. This linear impedance model can be used to conduct the harmonic analysis of the VSC-interfaced systems. However, this model may be insufficient since the impacts of the outer control loop and the power loop are not included.



(a) small-signal impedance model of VSC



(b) linear impedance model

Figure 2-3 Small-signal impedance model of VSC

### 2.2.3 Frequency Coupling Matrix (FCM) Model

The frequency coupling matrix is a harmonic coupling matrix that models the admittance of a VSC at harmonic frequencies and the cross-coupling of different frequencies. The frequency coupling matrix can generally be represented as (2.1)

$$I_{th} = [M]V_{th} + [W]V_{th}^* \quad (2.1)$$

where  $I_{th}$  represents the harmonic current at the terminal of equipment and  $V_{th}$  represents the background harmonic voltage at the terminal of equipment; M and W are the frequency coupling impedance matrix; superscript “\*” means the operation of the complex conjugate. In [61], the computation of the FCM model has been proposed. But this method mainly addresses the impact of the switching function for low switching frequency (e.g.,  $9f_1$ ). Furthermore, the frequency coupling effect induced by other parts such as the control loop and power loop has not been fully revealed.

The computation of the FCM model requires the detailed internal parameters of the VSC and the precise switching function, which may not be attainable for practical VSC equipment. Therefore, in [62][63], the determination of the parameters of the FCM model using measurements has also been described. This method does not require detailed internal parameters, which makes it a practical method for commercial VSC equipment. The test can be conducted as shown in

Figure 2-4, in which the ac supply imposes harmonics to the VSC, and the harmonic impedance can be computed. The test results show that inverter-based PV behaves as an impedance at harmonic frequencies. However, the main shortcoming of this method is that this measurement-determined model does not provide analytical justifications on the mechanism of the FCM model. Consequently, the model cannot show all the harmonic characteristics of the VSC. For example, it cannot disclose the contributions of each operating segment of the VSC, and as a result, the impacts of the parameters of the VSC cannot be fully understood.

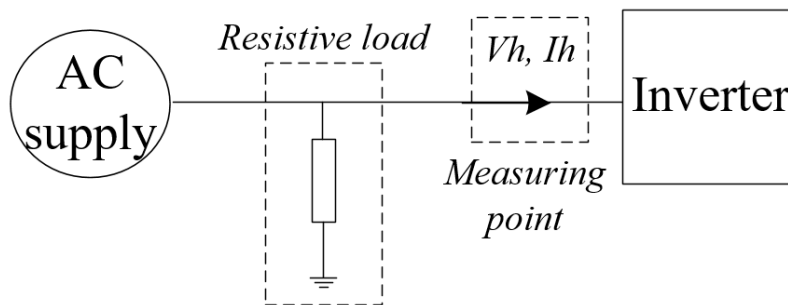


Figure 2-4 FCM model determination using measurements

#### 2.2.4 Norton Model of VSC (Wind Turbine) in IEC Report

In addition to the above methods, an IEC committee has also proposed the determination of the harmonic model of VSC-based wind turbines. Previously, the IEC committee suggested using measured harmonic current source models to represent the VSC-based wind turbines [64]. This current source can be easily used for harmonic power flow analysis. But the method has been reported to be inaccurate [65] since the harmonic current emission of a wind turbine is affected by the background harmonic voltage. A recent IEC report [65] has suggested a Norton equivalent model to improve the accuracy. Model parameters need to be measured. The main procedures for determining the model parameters using measurements can be illustrated using Figure 2-5. First, conduct a measurement when the wind turbine is connected to a standard source (no harmonics in the ac supply system). Measuring the harmonic current and voltage of the wind turbine gives the harmonic emission of the wind turbine. Second, conduct a measurement

when the wind turbine is connected to the ac supply system with harmonics, and the harmonic voltage and current of the wind turbine are measured. Third, disconnect the wind turbine from the ac supply and immediately measure the harmonic voltage. The harmonic emission from the VSC and the response of the wind turbine to background harmonics can be obtained by combining these measurements.

The main problem with this method is that the report does not provide technical justifications why this method is reliable. As a result, there is no assurance that the method will always work. Also, this method does not provide detailed insights into the harmonic features of the wind turbine.

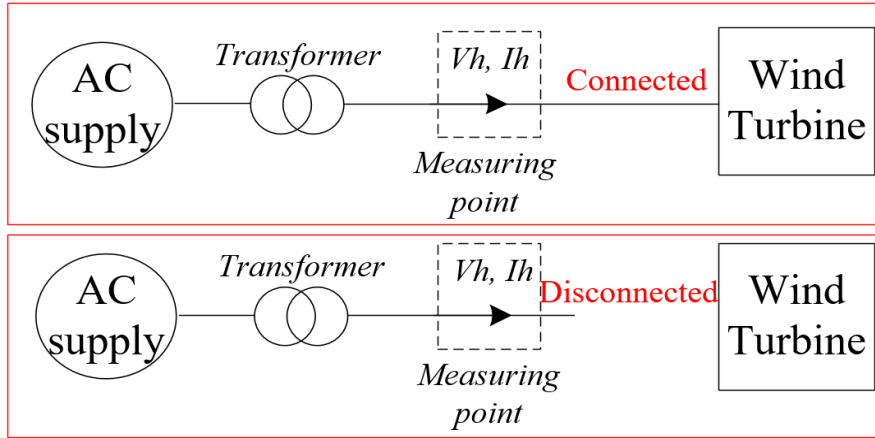


Figure 2-5 Norton circuit model determination using measurements

### 2.3 Harmonic Modeling of the VSC

The typical two-level, three-phase VSC equipment shown in Figure 2-6 is often used to derive the harmonic model of VSC equipment since this is the most common type of VSC [2]. The control strategy of the VSC is also shown in the figure where the active power and reactive power ( $P, Q$ ) ejected into the system by the VSC are maintained to specific values ( $P_{ref}, Q_{ref}$ ) through the outer control loop [66]. The constant power control of the VSC can be achieved by maintaining the current at the point of common coupling (PCC), which is the inner control loop. PI regulators are used for both the outer and inner loops. The current control is

designed in the synchronously rotating  $dq$  frame. Thus, a PLL is used to track the angle of the fundamental frequency voltage at the PCC, which will be used for  $abc/dq$  and  $dq/abc$  conversions. An LCL filter is connected at the front of the VSC to attenuate the switching harmonics. A capacitor on the dc side of the VSC contains the dc-link voltage. The system on the other side of the dc-link capacitor varies depending on the type of VSC equipment, which can be a source that transfers dc power to the VSC or can be a load that absorbs dc power from the VSC.

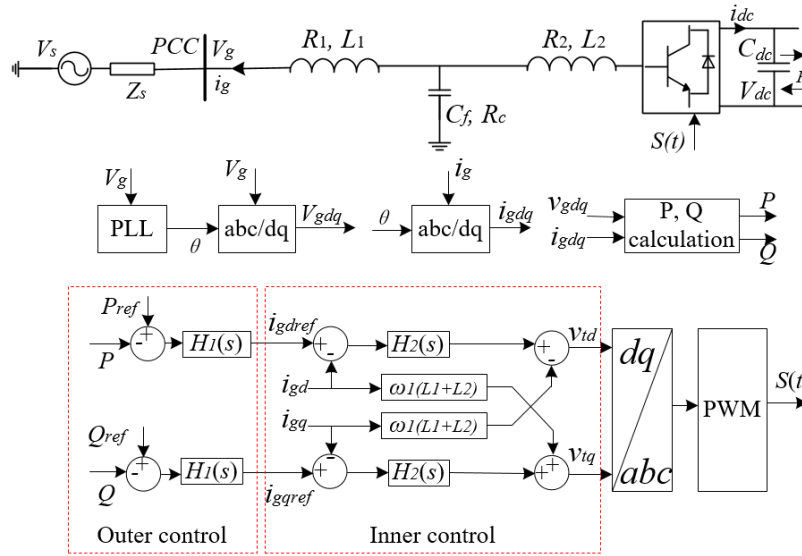


Figure 2-6 Structure of a typical two-level, three-phase VSC

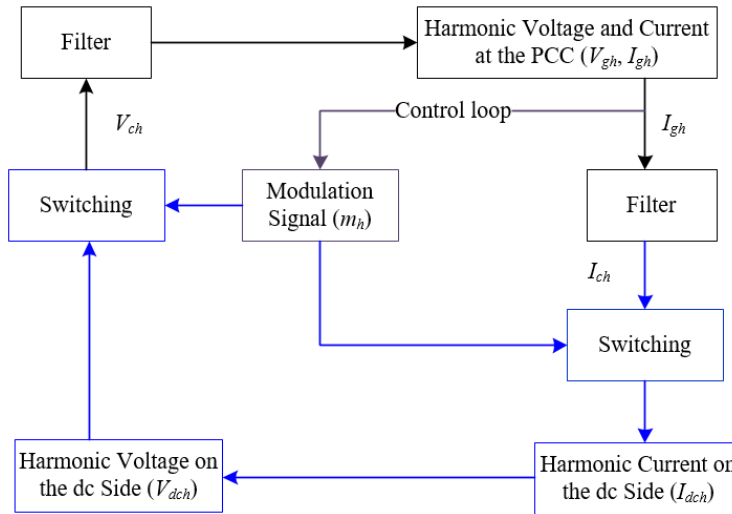


Figure 2-7 The flow of the derivation of the harmonic model for VSC

According to the above analysis of the harmonic response of VSC, the flow of the derivation of VSC's harmonic model is shown in Figure 2-7. As one can see, the flow of the derivation of the harmonic model can give a close-loop representation of the harmonic response of the VSC, which can lead to an equation that contains the harmonic voltage and current at the PCC. Solving this equation can lead to the relationship between the harmonic voltage and current at the PCC, which is the final harmonic model of the VSC. The detailed steps to establish the harmonic model are summarized as below:

- The power system has harmonic voltage and current at the PCC ( $v_{gh}$ ,  $i_{gh}$ ). The harmonic voltage and current affect the modulation signal ( $m$ ) through the control loop. The spectrum components in the modulation signal ( $m_1$  and  $m_h$ ) and the resulting switching function, as functions of  $v_{gh}$ ,  $i_{gh}$ , can be derived analytically.
- The low-order harmonic components in the dc-side current ( $I_{dch}$ ) can be computed using the above switching function and the ac-side current of the converter ( $i_c$ ). The harmonic components in the dc-link voltage ( $V_{dch}$ ) can be derived analytically as well based on the dc-side current. The product of the aforementioned switching function and dc-link voltage gives the voltage on the ac side of the VSC ( $v_{ch}$ ).
- Accordingly, one equation is established in which the voltage on the ac side of the VSC ( $v_{ch}$ ) can be represented as a function of the harmonic voltage and current at the PCC ( $v_{gh}$ ,  $i_{gh}$ ).
- Since the voltage on the ac side of the VSC relates to the harmonic voltage and current at the PCC through the LCL filter, another equation can be established relating the voltage on the ac side of the VSC, the current at the PCC, and the voltage at the PCC.
- The above two sets of equations can lead to an equation that contains the harmonic voltage and current at the PCC, i.e.,  $f(v_{gh}, i_{gh})=0$ . Solving this equation results in the harmonic model of the VSC.

### 2.3.1 Modeling the Impact of the Control Loop

In the steady-state, the voltage and current at the PCC of a balanced three-phase system that contains positive-sequence and negative-sequence harmonics can be expressed as

$$\begin{aligned} v_{ga} &= V_{g1} \cos(\omega_1 t + \theta_{g1}) + \sum V_{gh+} \cos(\omega_{h+} t + \theta_{gh+}) + \sum V_{gh-} \cos(\omega_{h-} t + \theta_{gh-}) \\ i_{ga} &= I_{g1} \cos(\omega_1 t + \delta_{g1}) + \sum I_{gh+} \cos(\omega_{h+} t + \delta_{gh+}) + \sum I_{gh-} \cos(\omega_{h-} t + \delta_{gh-}) \end{aligned} \quad (2.2)$$

and phase-B and phase-C voltages and currents are a  $120^\circ$  shift from phase-A voltage and current. In (2.2), “1” represents the components relating to the fundamental frequency,  $\theta$  is the angle of voltage,  $\delta$  is the angle of current,  $\omega$  is the angular frequency, and “ $h+$ ” and “ $h-$ ” stand for positive-sequence and negative-sequence harmonic order. The zero-sequence harmonic is zero in the  $dq$  frame, so there is no need to include this type of harmonic in the analysis of the control loop. The control is designed in the synchronously rotating  $dq$  frame, and the  $d$ -axis voltage is aligned with the space vector of voltage; thus, voltage and current are converted into  $dq$  frame as follows:

$$\begin{aligned} [V]_{dq} &= T[V]_{abc} \\ [I]_{dq} &= T[I]_{abc} \end{aligned} \quad (2.3)$$

where

$$T = \begin{bmatrix} \cos(\omega_1 t + \theta_{g1}) & \cos(\omega_1 t + \theta_{g1} - 120^\circ) & \cos(\omega_1 t + \theta_{g1} + 120^\circ) \\ -\sin(\omega_1 t + \theta_{g1}) & -\sin(\omega_1 t + \theta_{g1} - 120^\circ) & -\sin(\omega_1 t + \theta_{g1} + 120^\circ) \end{bmatrix} \quad (2.4)$$

The transformation in (2.4) is obtained by the phase-lock loop (PLL) in Figure 2-6. Because we focused on the steady-state harmonic analysis and the bandwidth of the PLL is generally very low (e.g., 100Hz), the steady-state harmonic components do not affect the PLL [2]. Substituting (2.2) to (2.3) leads to

$$\begin{aligned} v_{gd} &= V_{g1} + \sum V_{gh+} \cos(\omega_{h+} t + \theta_{gh+} - \omega_1 t - \theta_{g1}) + \sum V_{gh-} \cos(\omega_{h-} t + \theta_{gh-} + \omega_1 t + \theta_{g1}) \\ v_{gq} &= \sum V_{gh+} \sin(\omega_{h+} t + \theta_{gh+} - \omega_1 t - \theta_{g1}) - \sum V_{gh-} \sin(\omega_{h-} t + \theta_{gh-} + \omega_1 t + \theta_{g1}) \end{aligned} \quad (2.5)$$

$$\begin{aligned}
i_{gd} &= I_{g1} \cos(\delta_{g1} - \theta_{g1}) + \sum I_{gh+} \cos(\omega_{h+}t + \delta_{gh+} - \omega_1t - \theta_{g1}) \\
&\quad + \sum I_{gh-} \cos(\omega_{h-}t + \delta_{gh-} + \omega_1t + \theta_{g1}) \\
i_{gq} &= I_{g1} \sin(\delta_{g1} - \theta_{g1}) + \sum I_{gh+} \sin(\omega_{h+}t + \delta_{gh+} - \omega_1t - \theta_{g1}) \\
&\quad - \sum I_{gh-} \sin(\omega_{h-}t + \delta_{gh-} + \omega_1t + \theta_{g1})
\end{aligned} \tag{2.6}$$

To represent the outer control loop in Figure 2-6, the active power and reactive power for the outer control loop are computed based on the voltage and current in (2.5) and (2.6). The results are shown as (2.7) and (2.8)

$$\begin{aligned}
P &= \frac{3}{2} (v_{gd} i_{gd} + v_{gq} i_{gq}) = \\
&\left\{ \begin{aligned}
&V_{g1} I_{g1} \cos(\delta_{g1} - \theta_{g1}) + \sum V_{gh+} I_{gh+} \cos(\theta_{gh+} - \delta_{gh+}) \\
&+ \sum V_{gh-} I_{gh-} \cos(\theta_{gh-} - \delta_{gh-}) + V_{g1} \sum I_{gh+} \cos(\omega_{h+}t + \delta_{gh+} - \omega_1t - \theta_{g1}) \\
&+ V_{g1} \sum I_{gh-} \cos(\omega_{h-}t + \delta_{gh-} + \omega_1t + \theta_{g1}) + I_{g1} \sum V_{gh+} \cos(\omega_{h+}t + \theta_{gh+} - \omega_1t - \delta_{g1}) \\
&+ I_{g1} \sum V_{gh-} \cos(\omega_{h-}t + \theta_{gh-} + \omega_1t + \delta_{g1}) + \sum_{x,y \in h+} V_{gm} I_{gn} \cos(\omega_x t + \theta_{gx} - \omega_y t - \delta_{gy}) \\
&+ \sum_{x,y \in h-} V_{gx} I_{gy} \cos(\omega_x t + \theta_{gx} - \omega_y t - \delta_{gy}) + \sum_{x \in h+, y \in h-} V_{gx} I_{gy} \cos(\omega_x t + \theta_{gx} + \omega_y t + \delta_{gy}) \\
&+ \sum_{m \in h-, n \in h+} V_{gx} I_{gy} \cos(\omega_x t + \theta_{gx} + \omega_y t + \delta_{gy})
\end{aligned} \right\} \tag{2.7}
\end{aligned}$$

$$\begin{aligned}
Q &= \frac{3}{2} (-v_{gd} i_{gq} + v_{gq} i_{gd}) \\
&= \frac{3}{2} \left\{ \begin{aligned}
&V_{g1} I_{g1} \sin(\theta_{g1} - \delta_{g1}) + \sum V_{gh+} I_{gh+} \sin(\theta_{gh+} - \delta_{gh+}) + \sum V_{gh-} I_{gh-} \sin(\theta_{gh-} - \delta_{gh-}) \\
&+ V_{g1} \sum I_{gh+} \sin(\omega_1t + \theta_{g1} - \omega_{h+}t - \delta_{gh+}) + V_{g1} \sum I_{gh-} \sin(\omega_1t + \theta_{g1} + \omega_{h-}t + \delta_{gh-}) \\
&+ \sum V_{gh+} I_{g1} \sin(\omega_{h+}t + \theta_{gh+} - \omega_1t - \delta_{g1}) - \sum V_{gh-} I_{g1} \sin(\omega_{h-}t + \theta_{gh-} + \omega_1t + \delta_{g1}) \\
&+ \sum_{x,y \in h+} V_{gx} I_{gy} \sin(\omega_x t + \theta_{gx} - \omega_y t - \delta_{gy}) + \sum_{x,y \in h-} V_{gx} I_{gy} \sin(\omega_x t + \theta_{gx} - \omega_y t - \delta_{gy}) \\
&+ \sum_{x \in h+, y \in h-} V_{gx} I_{gy} \sin(\omega_x t + \theta_{gx} + \omega_y t + \delta_{gy}) \\
&- \sum_{x \in h-, y \in h+} V_{gx} I_{gy} \sin(\omega_x t + \theta_{gx} + \omega_y t + \delta_{gy})
\end{aligned} \right\} \tag{2.8}
\end{aligned}$$

The active power and reactive power are fed into the outer control loop and yield a reference current of

$$\begin{aligned}
I_{dref} &= H_1(s)(P_{ref} - P) \\
I_{qref} &= H_1(s)(Q_{ref} - Q)
\end{aligned} \tag{2.9}$$

Substituting (2.7) and (2.8) to (2.9) can lead to the reference current for the inner current control loop. The three types of power in the active power and reactive power are: 1) fundamental frequency power determined only by the fundamental frequency voltage and current; 2) harmonic power determined only by the voltage and current of the same harmonic order; 3) interaction power determined by the voltage and current of different frequencies. Among these three types of powers, fundamental frequency power and harmonic power are dc quantities. The difference between these dc quantities and the  $P_{ref}$  and  $Q_{ref}$  through the PI regulator leads to the dc components in the reference current. These components are only related to the fundamental current in the  $abc$  frame. As a result, only the ac components (interaction power) in  $P$  and  $Q$  can lead to harmonics in the reference currents. The expressions are given in (2.10) and (2.11)

$$\begin{aligned}
I_{dref\_harmonic} &= -\frac{3}{2} H_1(s) \times \\
&\left\{ \begin{aligned}
&V_{g1} \sum I_{gh+} \cos(\omega_{h+}t + \delta_{gh+} - \omega_1t - \theta_{g1}) + V_{g1} \sum I_{gh-} \cos(\omega_{h-}t + \delta_{gh-} + \omega_1t + \theta_{g1}) \\
&+ I_{g1} \sum V_{gh+} \cos(\omega_{h+}t + \theta_{gh+} - \omega_1t - \delta_{g1}) + I_{g1} \sum V_{gh-} \cos(\omega_{h-}t + \theta_{gh-} + \omega_1t + \delta_{g1}) \\
&+ \sum_{x,y \in h+, x \neq y} V_{gx} I_{gy} \cos(\omega_x t + \theta_{gx} - \omega_y t - \delta_{gy}) + \sum_{x,y \in h-, x \neq y} V_{gx} I_{gy} \cos(\omega_x t + \theta_{gx} - \omega_y t - \delta_{gy}) \\
&+ \sum_{x \in h+, y \in h-} V_{gx} I_{gy} \cos(\omega_x t + \theta_{gx} + \omega_y t + \delta_{gy}) + \sum_{x \in h-, y \in h+} V_{gx} I_{gy} \cos(\omega_x t + \theta_{gx} + \omega_y t + \delta_{gy})
\end{aligned} \right\}_F \tag{2.10}
\end{aligned}$$

$$\begin{aligned}
I_{qref\_harmonic} &= -\frac{3}{2} H_1(s) \times \\
&\left\{ \begin{aligned}
&V_{g1} \sum I_{gh+} \sin(\omega_1t + \theta_{g1} - \omega_{h+}t - \delta_{gh+}) + V_{g1} \sum I_{gh-} \sin(\omega_1t + \theta_{g1} + \omega_{h-}t + \delta_{gh-}) \\
&+ \sum V_{gh+} I_{g1} \sin(\omega_{h+}t + \theta_{gh+} - \omega_1t - \delta_{g1}) - \sum V_{gh-} I_{g1} \sin(\omega_{h-}t + \theta_{gh-} + \omega_1t + \delta_{g1}) \\
&+ \sum_{x,y \in h+} V_{gx} I_{gy} \sin(\omega_x t + \theta_{gx} - \omega_y t - \delta_{gy}) + \sum_{x,y \in h-} V_{gx} I_{gy} \sin(\omega_x t + \theta_{gx} - \omega_y t - \delta_{gy}) \\
&+ \sum_{x \in h+, y \in h-} V_{gx} I_{gy} \sin(\omega_x t + \theta_{gx} + \omega_y t + \delta_{gy}) - \sum_{x \in h-, y \in h+} V_{gx} I_{gy} \sin(\omega_x t + \theta_{gx} + \omega_y t + \delta_{gy})
\end{aligned} \right\}_F \tag{2.11}
\end{aligned}$$

where lower subscript “ $F$ ” represents the frequency domain. Accordingly, the output signal of the inner control loop can be written as

$$\begin{aligned} u_{d\_harmonic} &= H_d(s)(H_2(s)[I_{dref\_harmonic} - I_{dh}] - \omega_1(L_1 + L_2)I_{qh}) \\ u_{q\_harmonic} &= H_d(s)(H_2(s)[I_{qref\_harmonic} - I_{qh}] + \omega_1(L_1 + L_2)I_{dh}) \end{aligned} \quad (2.12)$$

Converting the above  $dq$  voltage back to the  $abc$  frame leads to

$$\begin{aligned} V_{ta\_harmonic} &= H_d(s - j\omega_1)(-H_2(s - j\omega_1)I_{sah+} - j\omega_1(L_1 + L_2)I_{gah+} \\ &\quad - H_2(s - j\omega_1)I_{gah-} + j\omega_1(L_1 + L_2)I_{gah-} \\ &\quad - \frac{3}{2}H_1(s - j\omega_1)H_2(s - j\omega_1) \left\{ \begin{aligned} &V_{g1} \sum I_{gah+} \cos(\omega_{h+}t + \delta_{gh+} - 2\omega_1t - 2\theta_{g1}) \\ &+ V_{g1} \sum \dot{I}_{gah-} \cos(\omega_{h-}t + \delta_{gh-} + 2\omega_1t + 2\theta_{g1}) \\ &+ I_{g1} \sum \dot{V}_{gah+} + I_{g1} \sum \dot{V}_{gah-} \\ &+ \sum_{x,y \in h+, x \neq y} V_{gx} I_{gy} \cos(\omega_x t + \theta_{gx} - \omega_y t - \delta_{gy} + \omega_1 t + \theta_{g1}) \\ &+ \sum_{x,y \in h-, x \neq y} V_{gx} I_{gy} \cos(\omega_x t + \theta_{gx} - \omega_y t - \delta_{gy} - \omega_1 t - \theta_{g1}) \\ &+ \sum_{x \in h+, y \in h-} V_{gx} I_{gy} \cos(\omega_x t + \theta_{gx} + \omega_y t + \delta_{gy} + \omega_1 t + \theta_{g1}) \\ &+ \sum_{x \in h-, y \in h+} V_{gx} I_{gy} \cos(\omega_x t + \theta_{gx} + \omega_y t + \delta_{gy} - \omega_1 t - \theta_{g1}) \end{aligned} \right\} \end{aligned} \quad (2.13)$$

and the phase-B and phase-C voltages can be given similarly. Since we consider a balanced system, only phase-A is discussed. It has to be noted that the harmonic components in (2.13) that are introduced by the interaction between different harmonics can be ignored due to the small magnitudes. The modulation signal is related to the above voltage via the following equation

$$m_{ah} = (\sqrt{2/3}V_{nom} / V_{dc0})u_{ta\_harmonic} \quad (2.14)$$

where  $V_{nom}$  is the nominal line-line voltage, and  $V_{dc0}$  is the desired dc voltage.

### 2.3.2 Modeling the Impact of the Power Loop

The above analysis has shown that due to the existence of the harmonic components in the ac-side voltage and current, there will also be harmonic components in the modulation signal. The modulation signal of VSC can thus be written as

$$m_a = m_1 \cos(\omega_1 t + \gamma_1) + \sum m_{h^+} \cos(\omega_{h^+} t + \gamma_{h^+}) + \sum m_{h^-} \cos(\omega_{h^-} t + \gamma_{h^-}) \quad (2.15)$$

and the modulation signals for phases B and C have a 120-degree angle shift from the voltage and current in (2.15). In (2.15),  $\gamma$  is the angle of the modulation signal. Similarly, the steady-state current on the ac side of the converter can be expressed as

$$I_{ca} = I_{c1} \cos(\omega_1 t + \delta_{c1}) + \sum I_{ch^+} \cos(\omega_{h^+} t + \delta_{ch^+}) + \sum I_{ch^-} \cos(\omega_{h^-} t + \delta_{ch^-}) \quad (2.16)$$

and currents for phases B and C have a 120-degree angle shift from (2.16), and  $\delta_c$  is the angle of the converter side current. The dc side current can be computed using the switching function and the ac side current. The switching function, i.e., the output signal of the PWM, can reproduce the modulation signal but it also introduces additional high-frequency harmonics. The switching harmonics are omitted here. The validation for doing this will be discussed in Section 2.4. Accordingly, the current on the dc side of the converter can be written as

$$\begin{aligned} I_{dc}(t) &= m_a(t)I_{ca}(t) + m_b(t)I_{cb}(t) + m_c(t)I_{cc}(t) \\ &= \frac{3}{2} m_1 I_{c1} \cos(\gamma_1 - \delta_{c1}) + \frac{3}{2} \sum I_{c1} m_{h^+} \cos(\omega_{h^+} t - \omega_1 t + \gamma_{h^+} - \delta_{c1}) \\ &\quad + \frac{3}{2} \sum I_{c1} m_{h^-} \cos(\omega_{h^-} t + \omega_1 t + \gamma_{h^-} + \delta_{c1}) + \frac{3}{2} \sum m_1 I_{ch^+} \cos(\omega_{h^+} t + \delta_{ch^+} - \omega_1 t - \gamma_1) \\ &\quad + \frac{3}{2} \sum_{i,j \in h^+} m_i I_{cj} \cos(\omega_i t - \omega_j t + \gamma_i - \delta_{cj}) + \frac{3}{2} \sum_{i \in h^-, j \in h^+} m_i I_{cj} \cos(\omega_i t + \omega_j t + \gamma_i + \delta_{cj}) \\ &\quad + \frac{3}{2} \sum m_1 I_{ch^-} \cos(\omega_{h^-} t + \delta_{ch^-} + \omega_1 t + \gamma_1) + \frac{3}{2} \sum_{i \in h^+, j \in h^-} m_i I_{cj} \cos(\omega_i t + \gamma_i + \omega_j t + \delta_{cj}) \\ &\quad + \frac{3}{2} \sum_{i \in h^-, j \in h^-} m_i I_{cj} \cos(\omega_i t + \gamma_i - \omega_j t - \delta_{cj}) \end{aligned} \quad (2.17)$$

In (2.17), the harmonic components in the dc-side current that are introduced by the interaction between two different harmonics can be omitted due to the small magnitude. Note that the dc components in the dc-side current will pass to the other side of the dc-link capacitor while the harmonic components in the dc-side current can pass through the dc-link capacitor, leading to the voltage on the dc-link capacitor as

$$\begin{aligned}
V_{dc}(t) &= \frac{1}{C_{dc}} \int_0^t I_{dc}(t) dt + V_{dc}(0) \\
&= V_{dc0} + \frac{3}{2C_{dc}(\omega_{h+} - \omega_1)} \sum I_{c1} m_{h+} \cos(\omega_{h+}t - \omega_1t + \gamma_{h+} - \delta_{c1} - \frac{\pi}{2}) \\
&\quad + \frac{3}{2C_{dc}(\omega_{h-} + \omega_1)} \sum I_{c1} m_{h-} \cos(\omega_{h-}t + \omega_1t + \gamma_{h-} + \delta_{c1} - \frac{\pi}{2}) \\
&\quad + \frac{3}{2C_{dc}(\omega_{h+} - \omega_1)} \sum m_1 I_{ch+} \cos(\omega_{h+}t + \delta_{ch+} - \omega_1t - \gamma_1 - \frac{\pi}{2}) \\
&\quad + \frac{3}{2C_{dc}(\omega_{h-} + \omega_1)} \sum m_1 I_{ch-} \cos(\omega_{h-}t + \delta_{ch-} + \omega_1t + \gamma_1 - \frac{\pi}{2})
\end{aligned} \tag{2.18}$$

The above equation is obtained by assuming all harmonic components in the dc-side current pass through the dc-link capacitor. However, in practice, the other side of the dc-link may consist of a dc source or load, and the associated equivalent impedance is  $Z_{load}(h\pm 1)$  (the impedance feature will be further justified in Section 2.4). Under such a condition, all harmonic components in (2.18) need to be multiplied by a coefficient of  $Z_{load}(h\pm 1)/(Z_{load}(h\pm 1) + Z_{Cdc}(h\pm 1))$ . To simplify the illustration, this coefficient is not included in the following derivations, but it can be easily included when  $Z_{load}(h\pm 1)$  exists. The voltage in (2.18) is related to the ac-side voltage through the switching process, and the expression is given as

$$\begin{aligned}
V_{cah} &= \{m_a(t)V_{dc}(t)\}_h \\
&= \left\{ \sum m_{h+} \cos(\omega_{h+}t + \alpha_{h+}) + \sum m_{h-} \cos(\omega_{h-}t + \alpha_{h-}) \right\} V_{dc0} / \sqrt{2/3} / V_{nom} \Big|_1 \\
&+ \frac{3P_{nom}}{4V_{nom}^2 C_{dc} (\omega_{h+} - \omega_1)} \sum m_1 I_{c1} m_{h+} \cos(\omega_{h+}t + \alpha_{h+} + \alpha_1 - \delta_{c1} - \frac{\pi}{2}) \Big|_2 \\
&+ \frac{3P_{nom}}{4V_{nom}^2 C_{dc} (\omega_{h+} - \omega_1)} \sum m_1 I_{c1} m_{h+} \cos(\omega_{h+}t - 2\omega_1t + \alpha_{h+} - \alpha_1 - \delta_{c1} - \frac{\pi}{2}) \Big|_3 \\
&+ \frac{3P_{nom}}{4V_{nom}^2 C_{dc} (\omega_{h-} + \omega_1)} \sum m_1 I_{c1} m_{h-} \cos(\omega_{h-}t + 2\omega_1t + \alpha_{h-} + \alpha_1 + \delta_{c1} - \frac{\pi}{2}) \Big|_4 \\
&+ \frac{3P_{nom}}{4V_{nom}^2 C_{dc} (\omega_{h-} + \omega_1)} \sum m_1 I_{c1} m_{h-} \cos(\omega_{h-}t + \alpha_{h-} - \alpha_1 + \delta_{c1} - \frac{\pi}{2}) \Big|_5 \\
&+ \frac{3P_{nom}}{4V_{nom}^2 C_{dc} (\omega_{h+} - \omega_1)} \sum m_1^2 I_{ch+} \cos(\omega_{h+}t + \delta_{ch+} - \frac{\pi}{2}) \Big|_6 \\
&+ \frac{3P_{nom}}{4V_{nom}^2 C_{dc} (\omega_{h+} - \omega_1)} \sum m_1^2 I_{ch+} \cos(\omega_{h+}t - 2\omega_1t - 2\alpha_1 + \delta_{ch+} - \frac{\pi}{2}) \Big|_7 \\
&+ \frac{3P_{nom}}{4V_{nom}^2 C_{dc} (\omega_{h-} + \omega_1)} \sum m_1^2 I_{ch-} \cos(\omega_{h-}t + \delta_{ch-} + 2\omega_1t + 2\alpha_1 - \frac{\pi}{2}) \Big|_8 \\
&+ \frac{3P_{nom}}{4V_{nom}^2 C_{dc} (\omega_{h-} + \omega_1)} \sum m_1^2 I_{ch-} \cos(\omega_{h-}t + \delta_{ch-} - \frac{\pi}{2}) \Big|_9
\end{aligned} \tag{2.19}$$

where  $P_{nom}$  is the nominal power, and  $|_x$  is used to mark the number of terms ( $x=1\sim 9$ ), which can be used to identify the terms that impact the power loop. The voltage and current in (2.19) have been converted to per unit values to be consistent with the variables used in the above derivation of the control loop. The first term in (2.19) describes the relationship between the ac-side voltage of the VSC and the modulation signal when the impact of the dc-link capacitor is not included (i.e., an infinite capacitance). The rest of the terms in (2.19) indicate the impact of the dc-link capacitor. Equation (2.19) shows that a smaller dc-link capacitance will have a more noticeable impact on low-order harmonics. Equation (2.19) can be illustrated using Figure 2-8, where the red paths specify the impacts of the power loop. The dc-link capacitor has two main impacts. The first is that it makes the harmonic components in the ac-side voltage of the VSC deviate from those in the output signal of the inner current control ( $\sqrt{3}V_{dc0}m_h / \sqrt{2}V_{nom}$ , i.e., the first term of (2.19)). When the impact of the dc-link capacitor is not considered, the harmonic components in the modulation signal will be the same as those in the ac-side voltage

(black path in Figure 2-8). An additional linear relationship between the modulation signal and the ac-side voltage (the 2nd~5th terms of (2.19)) will be introduced with the power loop. The second impact of the power loop is that it introduces an additional capacitive impedance (the 6<sup>th</sup>~9<sup>th</sup> terms of (2.19)). This capacitive impedance appears because the capacitor will be connected to the ac system when the switches are on.

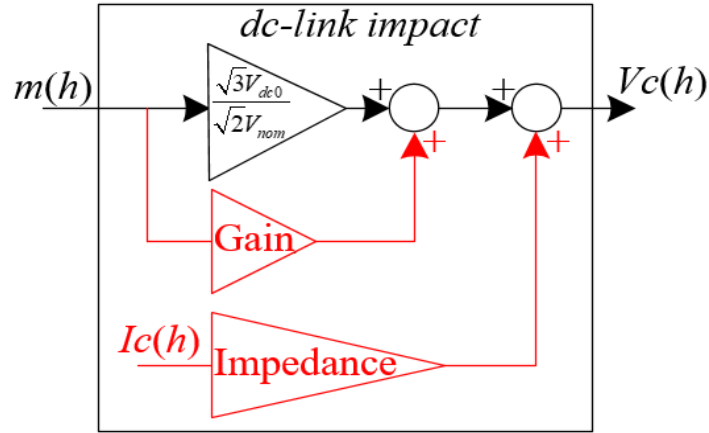


Figure 2-8 Illustration of the impact of the dc-link capacitor

### 2.3.3 Overall Harmonic Model of the VSC

The above analysis establishes the harmonic voltage on the ac side of the VSC as a function of the voltage and current at the PCC. The harmonic components in the voltage on the ac side of the converter can also be related to the harmonic voltage and current at the PCC through the front-end LCL filter, which is given as

$$V_{ch\pm} - \frac{Z_{L1} + Z_{Cf}}{Z_{Cf}} V_{gh\pm} = \frac{Z_{L1}Z_{L2} + Z_{L1}Z_{Cf} + Z_{L2}Z_{Cf}}{Z_C} I_{gh\pm} \quad (2.20)$$

where  $Z_{L1}$ ,  $Z_{L2}$ , and  $Z_{Cf}$  represent the harmonic impedance of  $L_1$ ,  $L_2$ , and  $C_f$ , respectively. Thus, combining (2.13), (2.14), (2.19), and (2.20) can lead to an equation that represents the relationship between the steady-state phase voltage and current at the PCC. This equation gives the harmonic model of phase A as follows:

$$\begin{bmatrix} \dot{V}_{ga3+} \\ \dot{V}_{ga5+} \\ \dot{V}_{ga7+} \\ \dots \\ \dot{V}_{gah+} \end{bmatrix} = \begin{bmatrix} Z_{3,3}^+ & Z_{3,5}^+ & Z_{3,7}^+ & \dots & 0 \\ 0 & Z_{5,5}^+ & Z_{5,7}^+ & \dots & 0 \\ 0 & 0 & Z_{7,7}^+ & \dots & 0 \\ \dots & \dots & \dots & \dots & \dots \\ 0 & 0 & 0 & \dots & Z_{h,h}^+ \end{bmatrix} \begin{bmatrix} \dot{I}_{ga3+} \\ \dot{I}_{ga5+} \\ \dot{I}_{ga7+} \\ \dots \\ \dot{I}_{gah+} \end{bmatrix} \quad (2.21)$$

$$\begin{bmatrix} \dot{V}_{ga3-} \\ \dot{V}_{ga5-} \\ \dot{V}_{ga7-} \\ \dots \\ \dot{V}_{gah-} \end{bmatrix} = \begin{bmatrix} Z_{3,3}^- & 0 & 0 & \dots & 0 \\ Z_{5,3}^- & Z_{5,5}^- & 0 & \dots & 0 \\ Z_{7,3}^- & Z_{7,5}^- & Z_{7,7}^- & \dots & 0 \\ \dots & \dots & \dots & \dots & \dots \\ 0 & 0 & 0 & \dots & Z_{h,h}^- \end{bmatrix} \begin{bmatrix} \dot{I}_{ga3-} \\ \dot{I}_{ga5-} \\ \dot{I}_{ga7-} \\ \dots \\ \dot{I}_{gah-} \end{bmatrix} \quad (2.22)$$

where

$$Z_{h,h}^{\pm} = -\frac{Z_{L1}(Z_{L2}+k_{2\pm})/Z_{Cf} + Z_{L1} + (Z_{L2}+k_{2\pm}) + k_{1\pm}H_2(s \mp j\omega_0) \mp j\omega_0(L_1+L_2)k_{1\pm}}{1.5I_{g1}H_2(s \mp j\omega_1)H_1(s \mp j\omega_1)k_{1\pm} + (Z_{L1} + Z_{Cf})/Z_{Cf}} \quad (2.23)$$

$$Z_{h,h+2}^+ = \frac{-1.5k_{3+}H_1(s-j\omega_1)H_2(s-j\omega_1)V_{ga1}e^{j(-2\theta_1)}}{1.5k_{3+}H_1(s-j\omega_1)H_2(s-j\omega_1)I_1 + (Z_{L1} + Z_{Cf})/Z_{Cf}} - \frac{-jV_{nom}^2 m_1^2}{2V_{dc0}P_{nom}^2 C_{dc}(\omega_{h+} - \omega_1)} \quad (2.24)$$

$$Z_{h,h-2}^- = \frac{-1.5k_{3-}H_1(s+j\omega_1)H_2(s+j\omega_1)V_{ga1}e^{j(2\theta_1)}}{1.5k_{3-}H_1(s+j\omega_1)H_2(s+j\omega_1)I_{a1} + (Z_{L1} + Z_{Cf})/Z_{Cf}} - \frac{-jV_{nom}^2 m_1^2}{2V_{dc0}P_{nom}^2 C_{dc}(\omega_{h-} + \omega_1)} \quad (2.25)$$

$$Z_{h,h+4}^+ = -\frac{3}{2}H_1(s-j\omega_1)H_2(s-j\omega_1)\frac{-j\sqrt{3}P_{nom}m_1I_{c1}}{2\sqrt{2}V_{dc0}V_{nom}C_{dc}(\omega_{h+} - \omega_1)}e^{j(-2\theta-\gamma_1-\delta_{c1})} \quad (2.26)$$

$$Z_{h,h-4}^- = -\frac{3}{2}H_1(s+j\omega_1)H_2(s+j\omega_1)\frac{-j\sqrt{3}P_{nom}m_1I_{c1}}{2\sqrt{2}V_{dc0}V_{nom}C_{dc}(\omega_{h-} + \omega_1)}e^{j(2\theta+\gamma_1+\delta_{c1})} \quad (2.27)$$

$$k_{1\pm} = 1 + \frac{\sqrt{3}P_{nom}}{2\sqrt{2}C_{dc}V_{dc0}V_{nom}(\omega_{h+} \mp \omega_1)} m_1 I_{c1} e^{j(\pm\gamma_1 - \delta_{c1} - \frac{\pi}{2})} \quad (2.28)$$

$$k_{2\pm} = \frac{-j3P_{nom}m_1^2}{4C_{dc}V_{nom}^2(\omega_{h+} \mp \omega_1)} \quad (2.29)$$

$$k_{3\pm} = 1 + \frac{\sqrt{3}P_{nom}}{2\sqrt{2}C_{dc}V_{dc0}V_{nom}(\omega_{h+} \mp \omega_1)} m_1 I_{c1} e^{j(\pm\gamma_1 - \delta_{c1} - \frac{\pi}{2})} \quad (2.30)$$

The above equations show that the VSC can be represented using a harmonically coupled frequency-dependent impedance matrix. Chapter 3 will prove that the degree of the coupling between different harmonics can be negligible so that the model can be further simplified as (2.31).

$$\begin{bmatrix} \dot{V}_{ga3\pm} \\ \dot{V}_{ga5\pm} \\ \dot{V}_{ga7\pm} \\ \dots \\ \dot{V}_{gah\pm} \end{bmatrix} = \begin{bmatrix} Z_{3,3}^\pm & 0 & 0 & \dots & 0 \\ 0 & Z_{5,5}^\pm & 0 & \dots & 0 \\ 0 & 0 & Z_{7,7}^\pm & \dots & 0 \\ \dots & \dots & \dots & \dots & \dots \\ 0 & 0 & 0 & \dots & Z_{h,h}^\pm \end{bmatrix} \begin{bmatrix} \dot{I}_{ga3\pm} \\ \dot{I}_{ga5\pm} \\ \dot{I}_{ga7\pm} \\ \dots \\ \dot{I}_{gah\pm} \end{bmatrix} \quad (2.31)$$

The following are findings from the model in (2.31):

- The VSC does not impact the power system by injecting harmonic current like conventional LCC equipment. Instead, the VSC only responds to the external harmonics by behaving as a frequency-dependent and fundamental frequency operating point-dependent impedance.
- The VSC's impedances at the positive-sequence and negative-sequence harmonics are different.
- The model is not affected by the distortion levels experienced by the VSC (i.e.,  $v_{gh}$ ), which means that it is a linear model and can be easily integrated into existing noniterative harmonic power flow tools.
- The computation of the proposed model requires the internal information of the VSC, which includes the filter parameters, control transfer functions,

fundamental frequency components. This also means the proposed model can be determined at an operating point before it is connected to an ac system.

Since the proposed impedance model is dependent on the fundamental frequency operating point, the fundamental frequency power flow analysis is first required to obtain the fundamental frequency voltage and current to compute the model parameters. Then the harmonic model of the VSC can be computed. Although the above model is derived based on a specific control scheme in Figure 2-6, it is possible to derive the model of the VSC with different configurations and control schemes using the same method. Developing an analytical generalized harmonic model of the VSC is challenging since the control strategy of the VSC could be diversified. In practice, it is crucial to find the harmonic nature of the VSC. For example, if the VSC can be proved to be an impedance under harmonic frequencies, the measurement-based method can be used to obtain the model regardless of the complexity of the control schemes.

## **2.4 Impact of the PWM on the Developed Model**

In previous derivations of the harmonic model of the VSC, the PWM is assumed to be ideal. This is only valid when two criteria are satisfied: 1) the modulated output signal of the PWM can reproduce the modulation waveform perfectly; 2) the PWM does not introduce additional harmonics that overlap with low-order harmonics in the modulation signal. In the following, these two aspects are analyzed.

### **2.4.1 Reproduction of the Modulation Signal**

Reproducing the modulation signal for the PWM is always justified if the switching frequency of the carrier signal is much higher than the frequency of the modulation signal. However, harmonic power flow study requires computing the harmonic distortions for harmonic power flow studies for up to the 29th harmonic. On the other hand, in many high-power VSC equipment, the switching frequency can be low (e.g., a switching frequency of 2 kHz is close to the 33<sup>rd</sup> harmonic).

Therefore, it is necessary to investigate how the switching frequency of the PWM affects the reproduction of the modulation signal.

To investigate how the PWM switching frequency impacts the harmonic components in the modulation signal, a bipolar double-edge PWM with a triangle carrier was analyzed numerically [23]. In this study, the modulation signal consisted of the fundamental frequency signal and a 10% harmonic. Figure 2.8 shows the results of the harmonics in the output signal of a PWM with different switching frequencies. The PWM is based on the widely used asymmetrical sampling technique [67]. Based on the results of Figure 2-9 and using a 5% difference as the threshold, we can conclude that if the switching frequency is 2 kHz, the proposed model is reasonably accurate for up to the 13<sup>th</sup> harmonic. If the switching frequency is 3 kHz, the proposed model is reasonably accurate for up to the 23<sup>rd</sup> harmonic. If the switching frequency is 4 kHz, the proposed model is reasonably accurate for up to the 29<sup>th</sup> harmonic.

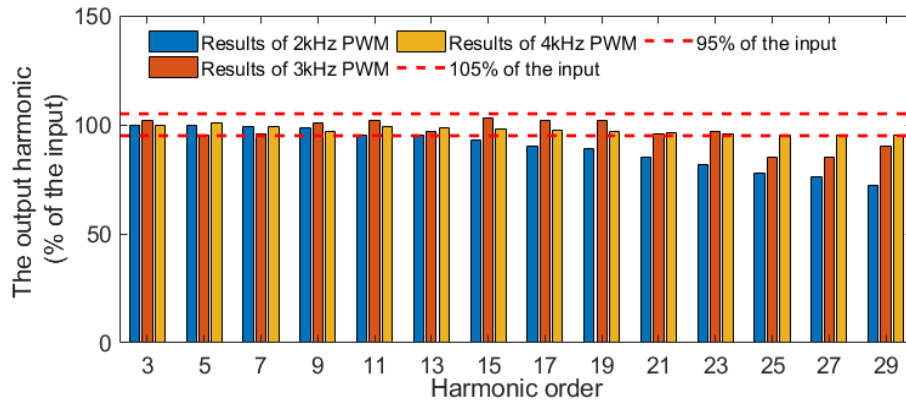


Figure 2-9 Results of the output harmonics for PWM with asymmetrical sampling technique

The above conclusions were obtained by assuming that the control loop (i.e., the modulation signal) always has a considerable impact on the impedance, that is, the modulation signal always contains considerable harmonics regardless of the harmonic frequencies. However, in practice, the high-frequency harmonics in the modulation signal can be very limited due to the control loop's limited bandwidth. Under such conditions, the PWM's reproduction limit does not affect impedances

at these harmonics. The impact of the control loop on the harmonic impedance of the VSC can be determined by comparing the calculated impedance using the proposed model and the calculated impedance without the impact of the control loop ( $m_h=0$ ). By applying a threshold of  $\pm 5\%$ , the range of harmonics for which the control loop has negligible impacts on the harmonic impedance can be obtained.

According to the above analyses, the applicable harmonics for the proposed model need to be determined by combining the impact of the switching frequency of the PWM and the impact of the control loop on the harmonic impedance of the VSC. As analyzed previously, for a specific switching frequency, the proposed model is only reasonably accurate for harmonics up to  $h_{limit\_PWM}$ . However, if the control loop makes a negligible contribution to the harmonic impedance for  $h_{limit\_PWM}$  and higher harmonics, the applicable harmonics for the proposed model can be extended. The process to determine applicable harmonics for the proposed model is summarized as:

- 1) Determine the highest harmonic for which a PWM has input/output error within  $\pm 5\%$  ( $h_{limit\_PWM}$ )
- 2) Plot the impedances of the VSC with and without the control loop ( $m_h=0$ ). Find the range of harmonics, for which the control has a contribution less than  $\pm 5\%$  ( $h_{limit\_control}$ )
- 3) Compare the  $h_{limit\_PWM}$  and  $h_{limit\_control}$ . If the  $h_{limit\_PWM} > h_{limit\_control}$ , the proposed model is reasonably accurate for all harmonics. If the  $h_{limit\_PWM} < h_{limit\_control}$ , the proposed model is valid for  $(0, h_{limit\_PWM})$  and  $(h_{limit\_control}, \infty)$  (except in the case of switching harmonics).

#### **2.4.2 Additional Harmonics Introduced by the PWM**

In addition to its impacts on the reproduction capability of the modulation signal, the PWM may also introduce additional low-order harmonics when the modulation signal contains harmonic components. When the modulation signal contains harmonic components, the harmonics associated with the PWM can also be given based on the double Fourier series method [23]. According to this method, when

there is a harmonic  $\omega_h$  in the modulation signal, the switching harmonics will have harmonics  $\omega_h$ ,  $\omega_c \pm 2\omega_1$ ,  $\omega_c - \omega_h \pm \omega_1$  (only the lowest switching harmonics are considered). With this understanding, and according to the mathematical derivations in Section 2.2, the harmonics in different voltages and currents can be illustrated using Figure 2-10. One can see from Figure 2-10 that, in addition to the original harmonics in the connected grid ( $\omega_h$ ), there are additional harmonics of  $\omega_c \pm 2\omega_1$ ,  $\omega_c \pm 2\omega_1 \pm \omega_1 \pm \omega_h$ ,  $\omega_c - \omega_h \pm \omega_1$ , and  $\omega_c - \omega_h \pm \omega_h$  appearing on the ac side of the VSC. Other harmonics may also exist but are much smaller. When the switching frequency is a multiple of three times the fundamental frequency ( $21\omega_1$ , for example), these harmonics might overlap with the other low-order harmonics. However, the bandwidth of the current control loop must be much lower than the switching frequency, and as a result,  $\omega_h \ll \omega_c$  [2], which means the above-mentioned harmonics are close to the switching frequency, and thus can be significantly attenuated by the front-end passive filter. Furthermore, if the switching frequency is not a multiple of the fundamental frequency, all the above harmonics are interharmonics that do not overlap with other low-order harmonics. Although only cases with one harmonic in the system are analyzed, the above theory can be adopted when multiple harmonics exist. In summary, the harmonics associated with the PWM are not a concern for low-order harmonic studies.

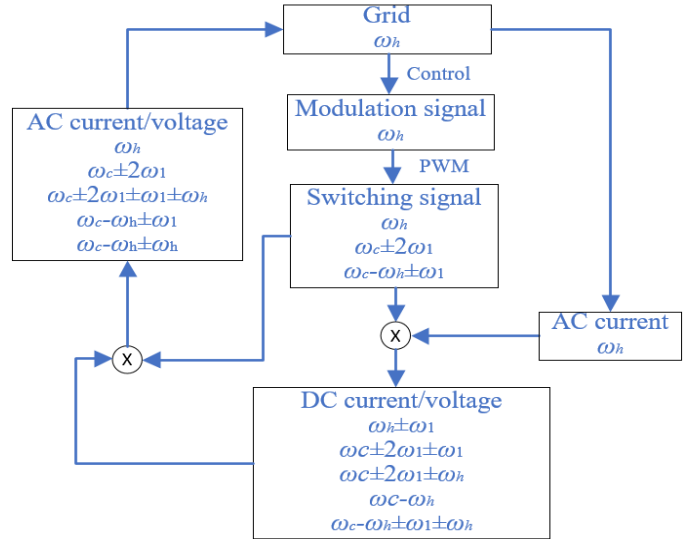


Figure 2-10 Harmonic information in VSC considering switching harmonics

## 2.5 Technical Discussions of the Proposed Harmonic model

This section examines technical discussions of the proposed harmonic model, including the applicable VSC equipment for the proposed model for VSC equipment and the characteristics of the converter impedance.

### 2.5.1 Applicable VSC Equipment for the Proposed Model

The above-proposed harmonic model of the three-phase VSC is established with the assumption that the dc system connected to the dc-link of the VSC can be represented as an equivalent impedance ( $Z_{load}$ ) at harmonic frequencies. Therefore, the proposed model can only be suitable for VSC equipment that satisfies this criterion. For equipment such as the Photovoltaic (PV) system and the VSC-based dc motor, the dc system can surely be modeled as an impedance [76], so the model can be applied for such equipment. On the other hand, for equipment such as Permanent Magnetic Synchronous Generator (PMSG) and VSC-based Variable Frequency Drive (VFD), another VSC is connected to the dc-link capacitor (i.e., back-to-back VSCs), as shown in Figure 2-11. It needs to be proved that the other VSC can be modeled as an impedance seen from the dc-link, i.e.,  $V_{dch}/I_{dch}$  is an impedance.

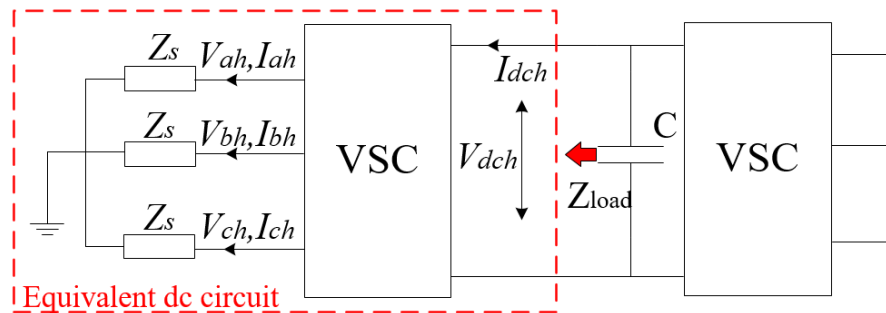


Figure 2-11 The equivalent circuit of a VSC seen from the dc-link capacitor

The basic strategy to demonstrate the impedance nature of the VSC seen from the dc-link capacitor is to assume a harmonic voltage on the dc-link capacitor ( $V_{dch}$ ). Then, based on the analytical representations of the control loop and power loop, the corresponding harmonic current ( $I_{dch}$ ) can be derived. By checking the

relationship between the  $I_{dch}$  and  $V_{dch}$ , the impedance feature can be verified.

Suppose there is a harmonic voltage on the dc-link that will induce a harmonic voltage on the ac side of the VSC. Note that the  $(h-1)$ -th harmonic on the dc side of the VSC corresponds to the  $h$ -th harmonic on the ac side of the VSC (here we only discuss positive-sequence harmonics, although negative-sequence harmonics can be addressed the same way), so the dc-link voltage and ac voltage of the VSC can be written as

$$V_{dc} = V_{dc0} + V_{dch-1} \cos(\omega_{h-1}t + \varphi_{h-1}) \quad (2.32)$$

$$V_a = V_{a1} \cos(\omega_1t + \theta_1) + V_{ah} \cos(\omega_h t + \theta_h) \quad (2.33)$$

The harmonic voltage on the ac side of the VSC will introduce a harmonic current on the ac side of the VSC, which can be expressed as

$$I_a = I_{a1} \cos(\omega_1t + \delta_1) + I_{ah} \cos(\omega_h t + \delta_h) \quad (2.34)$$

And the harmonic voltage and current on the ac side of the VSC have the following frequency-domain relationship

$$Z_s = \frac{\dot{V}_{ah}}{\dot{I}_{ah}} \quad (2.35)$$

where  $Z_s$  represents the harmonic impedance on the ac side of the other VSC (e.g., a generator in PMSG and the motor in a VFD). According to the analysis of the control loop, the modulation signal can also be written as

$$m_a = m_1 \cos(\omega_1t + \alpha_1) + m_h \cos(\omega_h t + \alpha_h) \quad (2.36)$$

It has been demonstrated that the harmonic components in the modulation signal are proportional to the harmonic components in the ac side current in the frequency domain, which can be expressed as

$$Z_{control} = \frac{\dot{m}_h}{\dot{I}_h} \quad (2.37)$$

According to the power loop analysis, the dc-side current can be written as

$$\begin{aligned} I_{dc} &= m_a I_a + m_b I_b + m_c I_c \\ &= I_{dc0} + \frac{3}{2} m_1 I_{ah} \cos(\omega_h t + \delta_h - \omega_1 t + \alpha_1) + \frac{3}{2} m_h I_{a1} \cos(\omega_h t + \alpha_h - \omega_1 t + \delta_1) \end{aligned} \quad (2.38)$$

So, the harmonic components in (2.38) represent the dc current's response ( $I_{dch}$ ) to the harmonic components in the dc-link voltage. Combining the above equations, the harmonic voltage and current on the dc side have the following relationship

$$\begin{aligned} Z_{load} &= \frac{V_{dc(h-1)}}{I_{dc(h-1)}} = \frac{V_{dc(h-1)} \cos(\omega_{h-1} t + \varphi_{h-1})}{\frac{3}{2} m_1 I_{ah} \cos(\omega_h t + \delta_h - \omega_1 t + \alpha_1) + \frac{3}{2} m_h I_{a1} \cos(\omega_h t + \alpha_h - \omega_1 t + \delta_1)} \\ &= \frac{V_{ah} \cos(\omega_h t + \theta_h) - V_{dc0} m_h \cos(\omega_h t + \alpha_h) / (\sqrt{2/3} V_{nom})}{\frac{3}{2} m_1 I_{ah} \cos(\omega_h t + \delta_h - \omega_1 t + \alpha_1) + \frac{3}{2} m_h I_{a1} \cos(\omega_h t + \alpha_h - \omega_1 t + \delta_1)} \end{aligned} \quad (2.39)$$

And the above equation can be expressed in the frequency domain as

$$\begin{aligned} Z_{load} &= \frac{\dot{V}_{dc(h-1)}}{\dot{I}_{dc(h-1)}} = \frac{\dot{V}_{ah} - V_{dc0} Z_{control} \dot{I}_{ah}}{\frac{3}{2} m_1 \dot{I}_{ah} e^{j\alpha_1} + \frac{3}{2} I_{a1} \dot{I}_{ah} Z_{control} e^{j\delta_1}} \\ &= \frac{Z_s - V_{dc0} Z_{control} / (\sqrt{2/3} V_{nom})}{\frac{3}{2} m_1 e^{j\alpha_1} + \frac{3}{2} I_{a1} Z_{control} e^{j\delta_1}} \end{aligned} \quad (2.40)$$

The above result shows that the VSC seen from the dc-link capacitor exhibits an impedance nature, so for the PMSG and VSC-VFD, the assumption that the dc system can always be regarded as an equivalent impedance is reasonable. Note that the assumption of an equivalent impedance for the VSC seen from the dc-link capacitor is only valid when the ac side of this VSC is not connected to the grid. When the other VSC is also connected to the grid, which means the ac side of the

other VSC contains harmonic sources, the impedance nature of the VSC seen from the dc-link capacitor is not valid. The equipment containing back-to-back VSCs exposed to grid harmonics will be studied in Chapter 5 (DFIG) and Chapter 6 (VSC-HVDC).

### 2.5.2 Characteristics of Converter Impedance

The above-developed harmonic impedance of the VSC is obtained at the PCC, which comprises the front-end passive filter and the converter. The main interest for the developed VSC model is the converter impedance since the impedance of the front-end passive filter can be easily established. In particular, the concern is whether the converter seen from its ac side is an impedance that is independent of the front-end passive filter. Answers to this question can determine whether the converter impedance can be independently obtained or whether the converter and front-end passive filter should take as a whole to determine the impedance. To test the above problem, we assume that the converter acts as an independent impedance, and the overall VSC can thus be represented using the equivalent circuit in Figure 2-12. According to this circuit, the following equation can be established as

$$Z_{VSC} = \frac{(Z_{conv} + Z_{L2})Z_{Cf}}{Z_{conv} + Z_{L2} + Z_{Cf}} + Z_{L1} \quad (2.40)$$

where  $Z_{VSC}$  is the overall impedance of the VSC given in (2.23), and  $Z_{conv}$  is the converter impedance. Figure 2-13 shows an exemplary result of the overall impedance of the VSC and corresponding converter impedance as described in (2.40). However, it is interesting to find that when the computed converter impedance is submitted back to (2.40) to calculate the overall impedance of the VSC, the new result of  $Z_{VSC}$  does not match well with the initial results, as shown in Figure 2-13. This means the equivalent circuit in Figure 2-12 is not correct, and the converter cannot be represented as an impedance that is independent of the front-end passive filter. This is because the feedback current of the control is from the PCC, and as a result, the harmonic voltage on the ac side of the converter is a function of the harmonic current at the PCC, as shown in Figure 2-14 (a).

Consequently, the converter is not an independent impedance. Therefore, the converter and filter must be considered as a unit for the harmonic model development of the VSC.

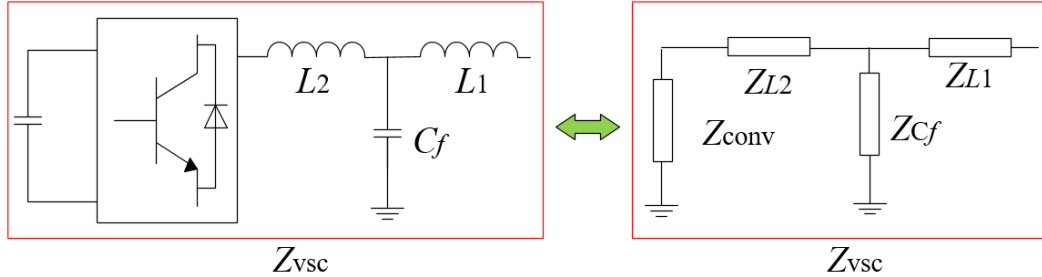


Figure 2-12 The equivalent circuit of VSC by assuming the converter is an independent impedance

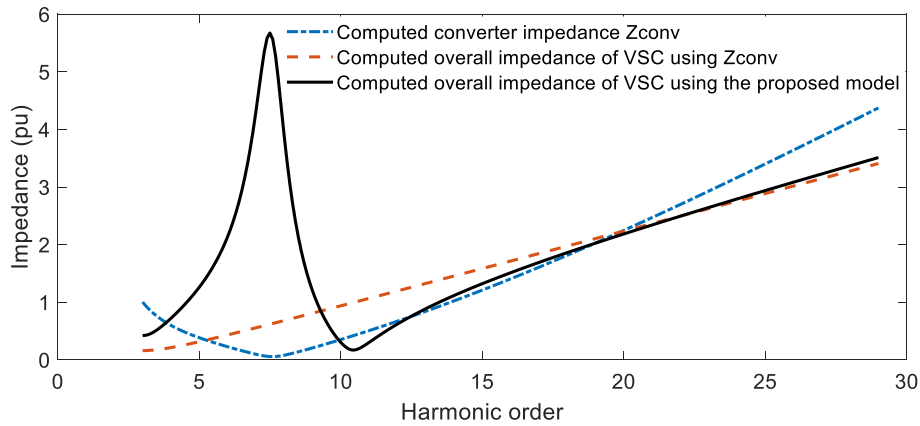
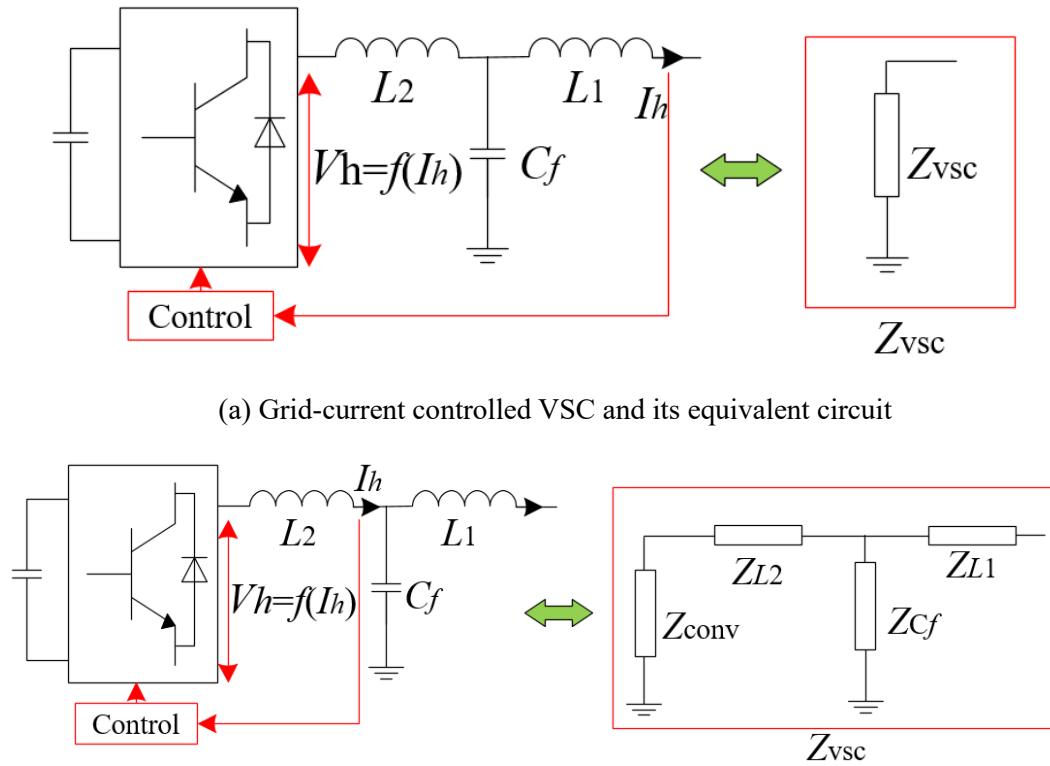


Figure 2-13 Calculated converter impedance and corresponding VSC impedance

However, it is noteworthy that different control schemes may lead to different characteristics of the converter impedance. For example, suppose the feedback current is from the ac side of the converter (or the front-end filter is only an inductor, which makes the current in the PCC the same as the current on the ac side of the converter). In that case, the harmonic voltage on the ac side of the converter will be a function of the harmonic current on the ac side of the converter, as shown in Figure 2-14 (b). Therefore, the converter can be a harmonic impedance independent of the front-end passive filter. As a result, the equivalent circuit in Figure 2-12 might be applicable. To summarize the above analysis, to ensure the harmonic model can always be correct for VSCs with different control schemes, the converter and the

filter should be considered as a unit for VSC's harmonic development.



(a) Grid-current controlled VSC and its equivalent circuit

(b) Converter-current controlled VSC and its equivalent circuit

Figure 2-14 Equivalent impedance of VSC with the different current control schemes

## 2.6 Summary

Based on the above analysis, the main findings and contributions of this chapter can be summarized as follows:

- The response mechanism of the VSC to power system harmonics was revealed. The impacts of both the control loop and power loop on the harmonic model of the VSC were mathematically analyzed.
- A harmonic model of VSC that can be used for harmonic analysis was developed. The result shows that the VSC can be represented by a coupled frequency-domain impedance matrix at low-order harmonics. This model is not affected by the distortion levels experienced by the VSC, so it is a linear

model. The equations to compute the new model were established.

- A comprehensive analysis of the impact of the PWM was presented in this chapter. The research defined the range of the harmonics to which that the proposed model can be applied. It also demonstrated that the interaction between the harmonics on the modulation signal and switching harmonics did not affect the proposed harmonic model.
- The applicable VSC equipment for the proposed model were discussed. The proposed model will be suitable for equipment containing only one VSC or equipment containing back-to-back VSCs but only one VSC connected to the grid. Typical examples of such VSC equipment include three-phase PV, VSC-VFD, and PMSG. The research work also showed that the harmonic model of VSC equipment would be developed by considering the converter and the front-end passive filter to function as a single unit.

# **Chapter 3**

## **Modeling Voltage Source Converters for Power System Harmonic Analysis: Model Verification and Application**

In this chapter, the proposed harmonic model of the voltage source converter (VSC) in Chapter 2 will be verified and analyzed via time-domain simulations and lab experiments. The correctness of the proposed model will be verified through time-domain simulations, and the frequency-dependent impedance nature of the VSC model be validated using lab experiments. Practical considerations, including the relative contribution of different operating segments of the VSC, the impact of the power loop, the impact of the control loop, the strength of coupling effect, as well as the measurement-based model determination, will be investigated to show the characteristics of the proposed model. According to the model characteristics, a practical procedure to construct the developed model will be proposed. Furthermore, the application of the proposed model for harmonic power flow studies will be demonstrated via time-domain simulations.

This chapter is organized as follows: Section 3.1 shows the verification of the proposed harmonic model of VSC via time-domain simulations and lab experiments. In Section 3.2, some practical considerations for the developed model are investigated. Section 3.3 presents a practical approach to constructing the developed model. The verification of the effectiveness of the proposed model for the harmonic power flow studies is presented in Section 3.4. Section 3.5 contains the chapter summary.

### 3.1 Verification of the Proposed Model Via Time-domain Simulations and Lab experiments

The proposed impedance model was verified using time-domain simulations, and the frequency-dependent impedance nature of the VSC model was validated using lab experiments. The simulations and experiments will be described in this section.

#### 3.1.1 Verification of the Proposed Model Via Time-domain Simulations

Figure 3.1 shows the system in which the proposed model was verified in Simulink/MATLAB. The control of the VSC is the same as the control scheme in Figure 2-6. The dc-link was a capacitor powered by a series connection of an ideal dc source and a resistor (to mimic a dc source). Table 3.1 shows the design parameters of the studied system, referring to the design method in [21].

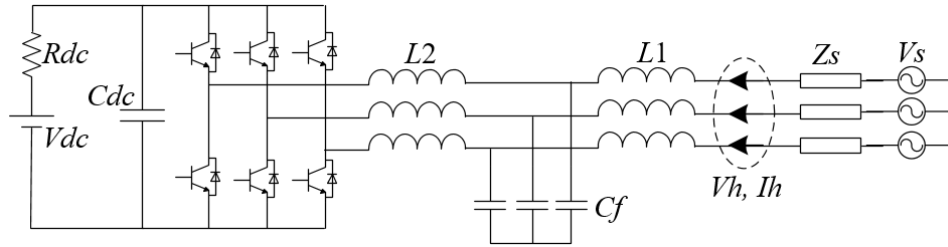


Figure 3-1 Studied system for verifying the proposed harmonic model

Table 3-1 Source of data

$f_{switch}$	3kHz	$L_2, R_2$	2.5mL, 0.01 $\Omega$
$L_1, R_1$	2.5mL, 0.01 $\Omega$	$C_f, R_c$	50 $\mu$ F, 1 $\Omega$
$H_1$	$k_p=0.033, k_i=2.46$	$H_2$	$k_p=0.3467, k_i=517$
$V_s$	380V	Rating	20kW
$V_{dc}$	760V	$R_{dc}$	100 $\Omega$

In power systems, odd harmonics constitute a significant concern. Thus, only these harmonics were investigated, and a set of positive-sequence and negative-sequence odd harmonics up to the 29<sup>th</sup> order were added in the ac source in Figure 3-1 to conduct the simulations. For the simulation, the voltage and current at the

PCC were measured, and a fast Fourier transform (FFT) was conducted to obtain the harmonic voltage and current ( $V_h$  and  $I_h$  in Figure 3-1), which were used to compute the harmonic impedance ( $V_h/I_h$ ). The simulated harmonic impedance of the VSC was compared with the calculated impedance using (2.23) in Figure 3-2. Figure 3-2 shows that the calculated harmonic impedance using the proposed model matched well with the simulated harmonic impedance. This verifies the correctness of the proposed model. Also, the positive-sequence impedance differed from the negative-sequence impedance. Thus, the positive-sequence and negative-sequence impedances had to be used separately for harmonic power flow studies. In the simulations, IHD for different harmonics in the ac source was increased up to 20%, and the same results were obtained, which means the model was linear.

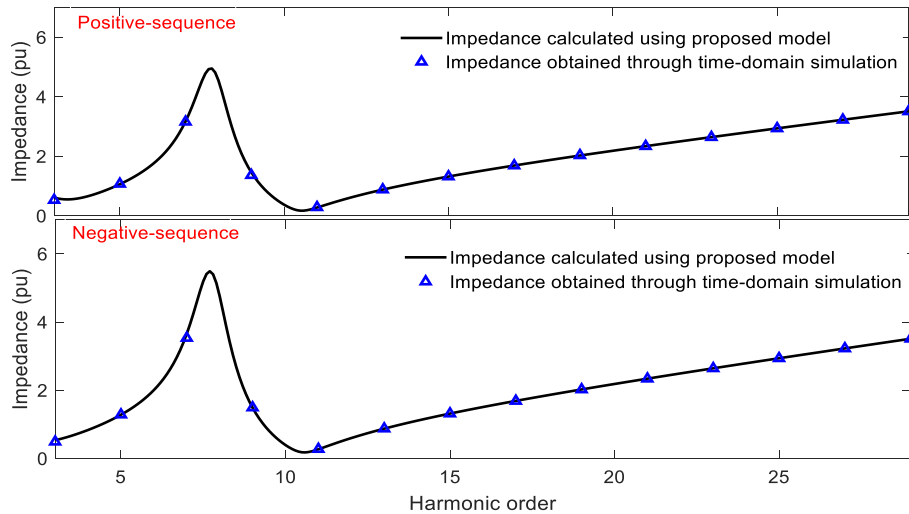


Figure 3-2 Comparison between the phase-A harmonic impedances calculated using the proposed model and impedances using time-domain simulations

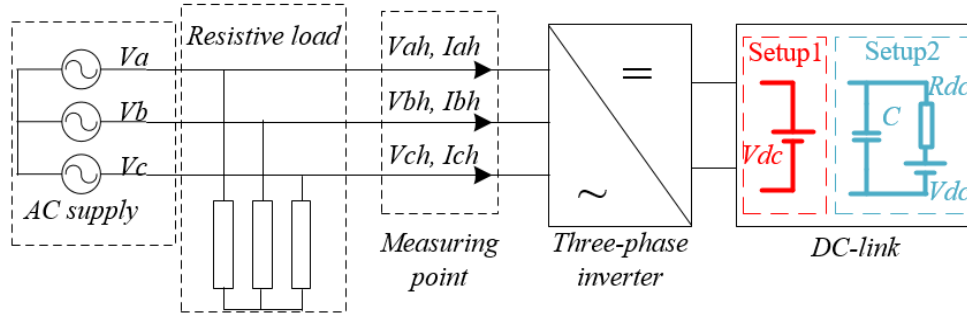
### 3.1.2 Verification of the Proposed Model Via Lab Experiments

The main finding of this work is that the VSC can be modeled as a frequency-dependent impedance at a specific harmonic. In this section, this impedance feature was verified by lab experiments in a 2kW VSC with the same control configurations as shown in Figure 2-6. The internal parameters were unknown and thus are represented by a black box seen from the grid side. The lab experiments were set

up following the schematical diagram in Figure 3-3 (a). There were two types of setups: 1) the dc-link was supplied by an ideal dc voltage source (300V), 2) the dc-link was a capacitor (80 $\mu$ F) powered by a series connection of an ideal dc voltage source (300V), and a resistor (30 $\Omega$ ). The first setup could be used to measure the harmonic impedance of the VSC with an infinite dc-link capacitor, while the second setup was to show the impact of the dc-link capacitor. The VSC inverter is operated at its nominal power, i.e., 2kW. The physical experimental setups are presented in Figure 3-3 (b).

In the lab experiments, multiple harmonics, including the 5<sup>th</sup>, 7<sup>th</sup>, and 11<sup>th</sup> harmonics of different IHDs (2%, 5%, 10%) were added to the voltage source of the ac supply. The FFT algorithm was applied to the voltage and current waveforms measured at the PCC of the VSC. The exemplary waveforms of the voltage and current when the ac source contained 5% of the 5<sup>th</sup>, 7<sup>th</sup>, and 11<sup>th</sup> harmonics for setup 1 and setup 2 are shown in Figure 3-4. The FFT results of the voltage and current were used to compute the harmonic impedances. Table 3-1 shows the experimental impedance results for all of the investigated cases. The results revealed the following key information:

- The impedance at one harmonic was almost constant regardless of the background harmonic distortion levels. This finding confirms that the VSC equipment can indeed be modeled as an impedance at each harmonic frequency for a specific operating point. The coupling effect was negligible since the results were not affected when multiple harmonics were added.
- The impedance for the VSC with a dc-link capacitance of 80 $\mu$ F was different from the impedance of the VSC with a constant dc source, verifying the impact of the dc-link capacitor. The differences were not significant for the 5<sup>th</sup> and 11<sup>th</sup> harmonic impedance, while the difference was more obvious for the 7<sup>th</sup> harmonic impedance.

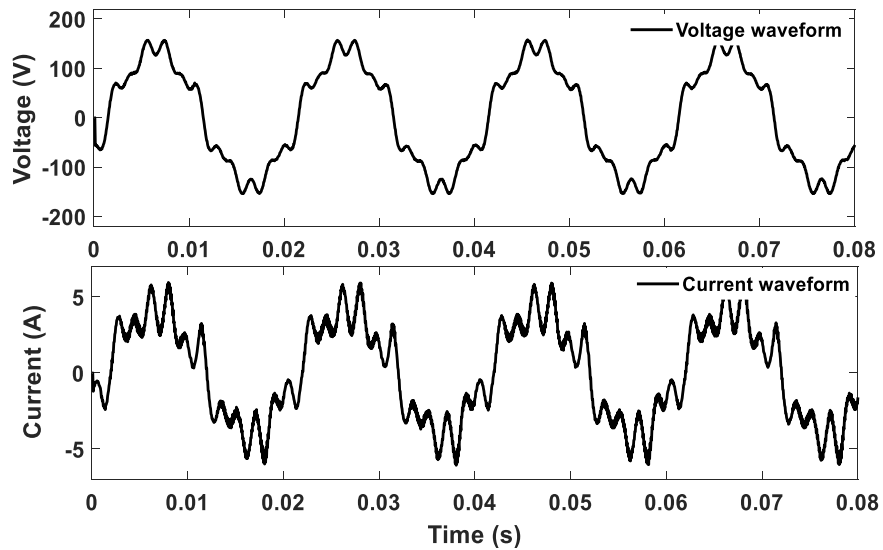


(a) Schematic diagram of the experimental setup

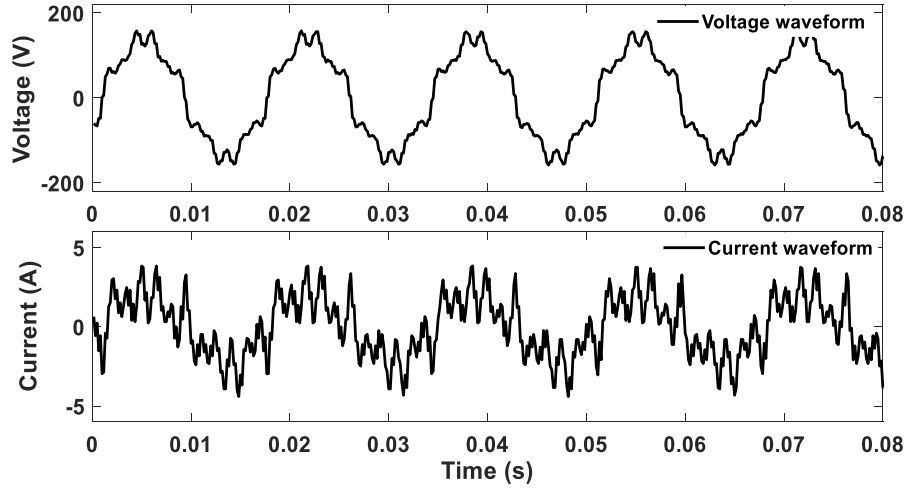


(b) Experimental setup for VSC impedance measurement

Figure 3-3 Experimental test of the harmonic impedance of a VSC



(a) experimental waveforms for setup1



(b) experimental waveforms for setup2

Figure 3-4 Recorded experimental waveforms of phase-A voltage and current at the PCC of VSC when 5% of the 5<sup>th</sup>, 7<sup>th</sup>, and 11<sup>th</sup> harmonics were added

Table 3-2 Measured phase-A impedance of a 2kW VSC under different background harmonics

		IHD	5 <sup>th</sup>	7 <sup>th</sup>	11 <sup>th</sup>
Setup1	Single harmonic	5%	27.77Ω	21.14Ω	14.41Ω
		10%	27.35Ω	21.51Ω	14.44Ω
	Multiple harmonic	5%	27.45Ω	21.05Ω	14.71Ω
		10%	27.73Ω	21.26Ω	14.85Ω
Setup2	Single harmonic	5%	28.10Ω	23.46Ω	14.64Ω
		10%	28.71Ω	23.10Ω	14.72Ω
	Multiple harmonic	5%	28.62Ω	23.51Ω	15.06Ω
		10%	28.11Ω	24.11Ω	15.10Ω

### 3.2 Practical Considerations and Simplifications

This section includes the analysis of the relative contribution of different VSC operating segments, the impact of the power loop, the impact of the control loop, the strength of the coupling, as well as the measurement-based approach are analyzed.

### 3.2.1 Relative Contribution of VSC Operating Segments

A VSC harmonic model consists of the contributions from three operating segments of the VSC equipment: (1) the front-end passive filter, (2) the control loop, and (3) the power loop. It is helpful to understand the relative impact of these segments to facilitate model construction. In Figure 3-5, the computed impedance using the proposed model of the system in Figure 3-1 (dc-link capacitance is  $20\mu\text{F}$ ) is compared with the computed impedance without the impact of the power loop (i.e., an infinite dc-link capacitance), the computed impedance without the impact of control ( $m_h=0$ ), and the filter impedance (i.e., both the control loop and power loop are omitted). The results show that the filter impedance contributes most to the VSC impedance, while the control loop and the power loop also have noticeable impacts. Therefore, it is suggested to include all operating segments of the VSC to obtain an accurate impedance. The impacts of the dc-link capacitor and control loop are only obvious for relatively low-order harmonics. The control only impacts the impedance for harmonics lower than the 13<sup>th</sup> while the power loop only impacts the harmonics lower than the 10<sup>th</sup>.

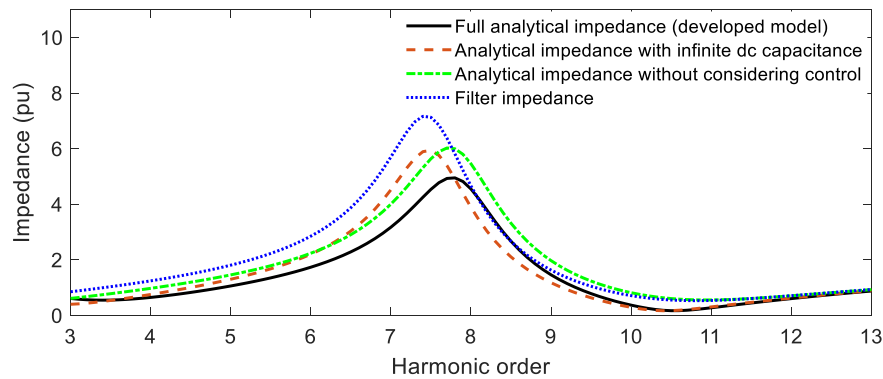


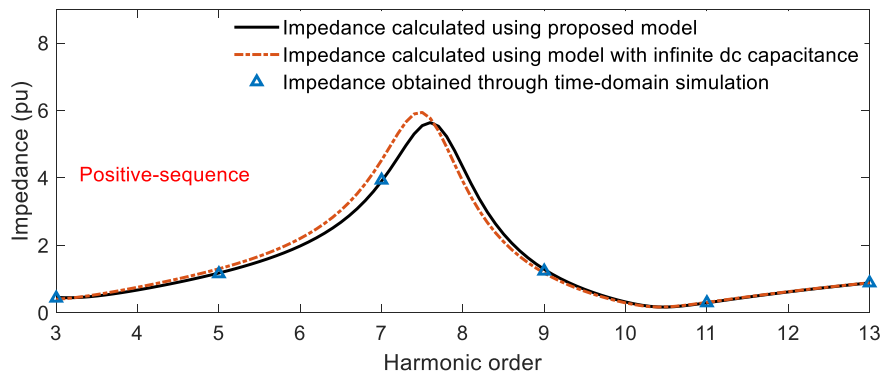
Figure 3-5 Impact of each operating segment on harmonic impedance

The switching frequency of the VSC was set at 3kHz. According to the analysis of the impact of the PWM, the PWM can only reasonably reproduce the harmonic components in the modulation signal for up to the 23<sup>rd</sup> harmonics. But as shown in Figure 3-5, the control loop did not have any impact on the impedance of the VSC for the 13<sup>th</sup> or higher harmonics. So as shown in Figure 3-2, the proposed model is

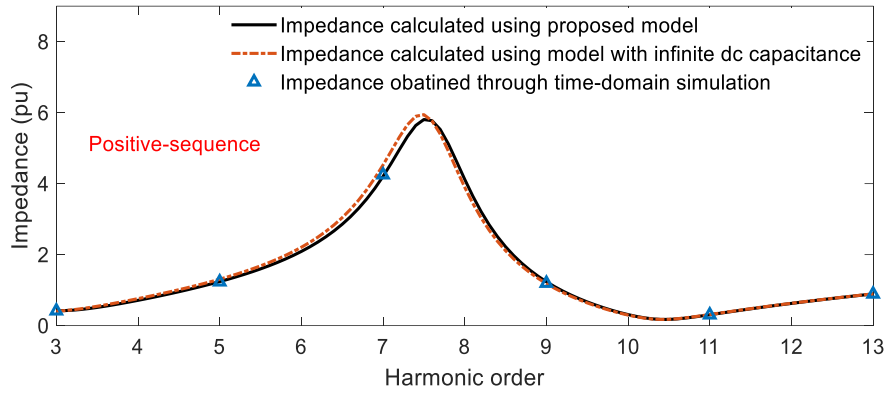
accurate for all harmonics.

### 3.2.2 The Impact of the Dc-link Capacitor

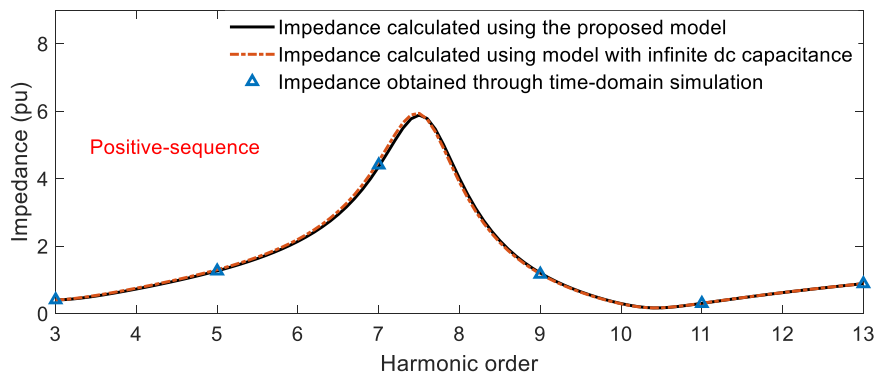
The simulation results are compared with two types calculated results to show the impact of the dc-link capacitor. The first calculated results are based on the proposed model for different dc-link capacitances (50 $\mu$ F, 100 $\mu$ F, 200 $\mu$ F). The second calculated results are based on the proposed model but the impact of the dc-link capacitor is not included (i.e., an infinite dc-link capacitance). The comparison results are shown in Figure 3-6. As Figure 3-6 shows, the results using the proposed model matched perfectly with the simulation results, while there were discrepancies with the calculated results for the infinite dc-link capacitor. This demonstrates that the power loop did affect the impedance of the VSC. Figure 3-6 also shows that the impact of the dc-link capacitor became less noticeable, which is consistent with the analytical model in (2.23). For comparisons, see Table 3-2, which shows the errors between the computed 7<sup>th</sup> harmonic impedance with an infinite dc-link capacitor and the simulation results. The error reached 12.86% for a dc-link capacitance of 50 $\mu$ F, and the difference declined to 3.2% when the dc-link capacitance was increased to 200 $\mu$ F.



(a) Harmonic impedance for a dc-link capacitance of 50 $\mu$ F



(b) Harmonic impedance for a dc-link capacitance of 100µF



(c) Harmonic impedance for a dc-link capacitance of 200µF

Figure 3-6 Comparison between the calculated harmonic impedances and simulated harmonic impedances for different dc-link capacitances

Table 3-3 Impact of the dc-link capacitance on the 7<sup>th</sup> harmonic impedance of the VSC under different dc-link capacitances

dc-link capacitance	Simulated impedance	Calculated impedance with $C_{dc}=\infty$	Error (%)
50µF	0.6276+0.9741i	0.6260 + 1.1482i	12.86%
100µF	0.6484+1.047i	0.6260 + 1.1482i	6.19%
200µF	0.663+1.08i	0.6260 + 1.1482i	3.2%

Although the above results show that the impact of the dc-link capacitor was not very significant, this research has quantified and clarified the degree of impact of the power loop on the VSC harmonic responses. The findings will enable users to

confidently model VSC with or without the inclusion of the power loop.

To determine whether the impact of the dc-link capacitor can be omitted in a VSC, a sensitivity study can be conducted before the harmonic impedance is given. As mentioned previously, the dc-link capacitor mainly impacted two aspects: the first was the variation of the control part effect represented by  $k_1$  in (2.28), the second was an additional impedance (series connected with  $L_2$ ) represented by  $k_2$  in (2.29). With this understanding, the impact of the dc-link on this part can be examined by comparing  $k_1$  to 1, and  $k_2/Z_{L_2}$  to 0. The analytical results of  $k_1$  and  $k_2/Z_{L_2}$  in the simulated VSC system with different dc-link capacitances are depicted in Figure 3-7, where  $k_1$  is closer to 1 and  $k_2/Z_{L_2}$  is closer to 0 with a capacitance of 100 $\mu$ F compared with a capacitance of 20 $\mu$ F, which is consistent with the results in Figure 3-6. Accordingly, a pre-calculation of  $k_1$  and  $k_2/Z_{L_2}$  can be conducted first to check the impact of the dc-link capacitance before computing the harmonic impedance. Using a 5% difference as a threshold, if  $k_1$  is smaller than 1.05 and  $k_2/Z_{L_2}$  is smaller than 0.05, then the impact of the dc-link capacitor can be omitted. And the criteria are given as follow

$$|k_1 - 1| \leq 5\% \quad \left| \frac{k_2}{Z_{L_2}} \right| \leq 5\% \quad (3.1)$$

If (3.1) is satisfied, the power loop does not need to be included.

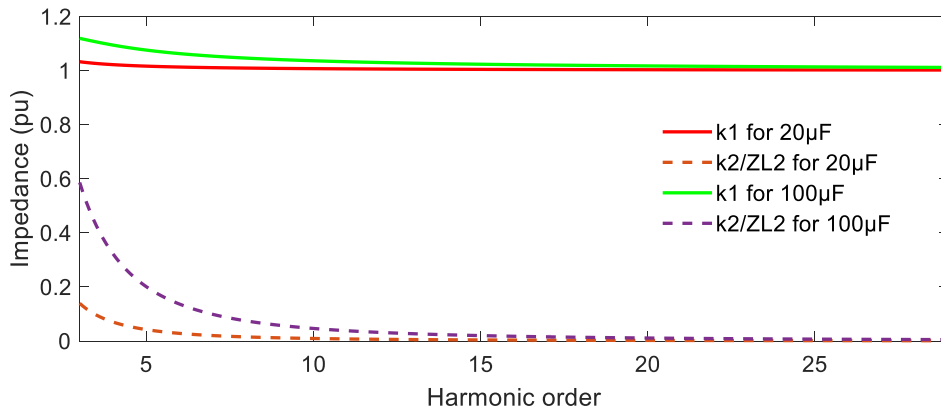


Figure 3-7 Numerical assessment of the impact of the dc-link capacitor

In practice, it is concerned whether the criteria in (3.1) are needed for a commercial VSC since the dc-link capacitor is designed within a specific range. The rating of the dc-link capacitor for a practical VSC can be given by the following equation [21]

$$C_{dc} \geq \frac{T_d \Delta P_{LMAX}}{2V_{dc0} \Delta V_{dc0}} \quad (3.2)$$

where,  $T_d$  is the delay caused by the voltage and current control,  $\Delta P_{LMAX}$  is the maximum known variation of the power on dc bus,  $V_{dc0}$  is the desired dc-link voltage, and  $\Delta V_{dc0}$  is the tolerable dc-link voltage variation. In addition, the rating of the dc-link capacitor is also designed to guarantee desired load ride-through capability. For the studied three-phase VSC (refer to parameters in Table 3-1), a dc-link capacitor of 50 $\mu$ F is enough to meet (3.2). If the dc-link capacitor is selected as 50 $\mu$ F, according to the results in Figure 3-6, the power loop must be included. But a larger dc-link capacitor may be adopted to increase the ride-through capability of the VSC. If the dc-link capacitor is selected to be larger than 200 $\mu$ F, the power loop can be omitted. Therefore, the power loop may impact the harmonic impedance of a practical VSC, and the criteria in (3.1) need to be checked.

### 3.2.3 The Impact of the Control Loop

The above analysis shows that the control loop has a considerable impact on the VSC harmonic impedance. The control loop consists of the outer and inner control loops. A further investigation was conducted to show the individual impact of the outer and inner control loops. Figure 3.8 shows a comparison between the impedance with the outer control loop and the impedance without the outer control loop. The impact of the outer control loop is not obvious for most harmonics, so the impact of the outer loop is not comparable with that of the inner loop. Yet, there are large errors for harmonics near the peak point of the impedance curve. For example, the impedance error reached 10% at the 11<sup>th</sup> harmonic. The reason was that the filter contributed to the impedance. For the peak value of the impedance, the filter experienced series resonance between  $L_1$  and  $C_f$ . As a result, the filter's contribution

to the impedance was reduced, and the cascaded outer control loop and inner control loop became more dominant in the overall impedance. Therefore, the outer control loop cannot be ignored near the peak value of the impedance. Also, the resonance impedance was affected by the damping of the filter, and the smaller damping led to the filter having less significance. Figure 3-8 shows a comparison between the different damping in the capacitor. The impedance error for the 11<sup>th</sup> harmonic increased to 27% when the resistance was reduced from 1Ω to 0.5Ω. In summary, although the outer control loop is not as significant as the inner control loop, it affects the impedance to some degree for some harmonics and needs to be taken into account for better accuracy.

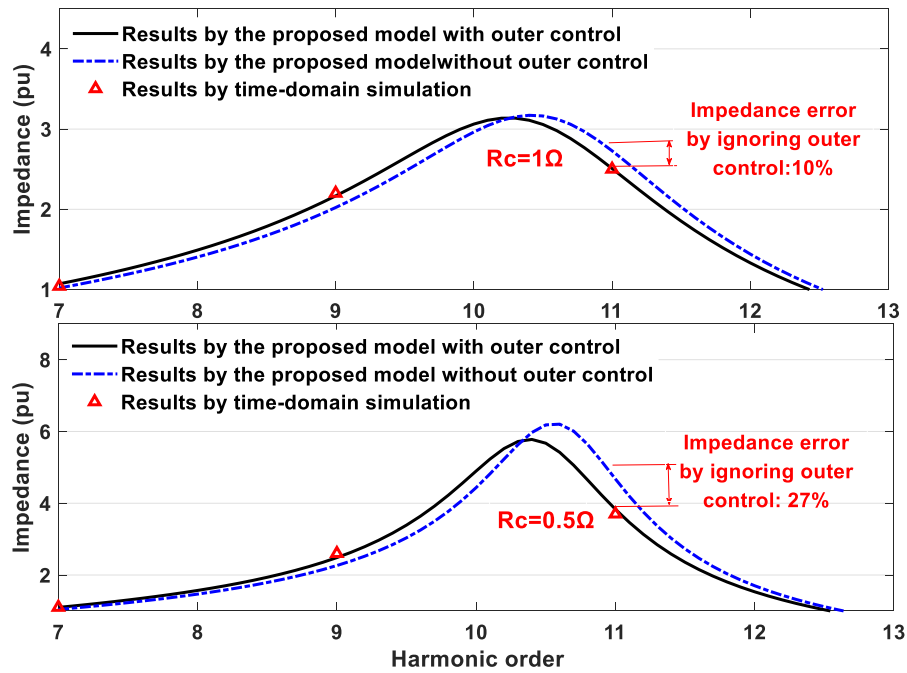


Figure 3-8 Impact of the outer control loop

### 3.2.4 Strength of the Coupling Effect

The proposed impedance matrix showed that there were coupling effects between different harmonics, which originated from the outer control loop and the power loop. There are two types of coupling effects: the coupling between  $h$ -th and  $(h+2)$ -th harmonics and the coupling between  $h$ -th and  $(h+4)$ -th harmonics. In both time-domain simulations and lab experiments, multiple harmonics were added at

the same time, but results remain almost the same. This meant the interaction between different harmonics was very limited. To verify the analytical nondiagonal impedance of the positive-sequence impedance matrix in (2.21) was compared with the diagonal impedance with a dc-link capacitance of  $50\mu\text{F}$ . The results are shown in Figure 3-9, where the coupling impedance is almost negligible compared to the diagonal impedance. The reason for this phenomenon is that both the outer control loop and dc-link make fewer contributions compared with the filter and inner current control that determine the diagonal impedance. Thus, the coupling effect can be omitted in most cases, resulting in a simplified diagonal impedance matrix.

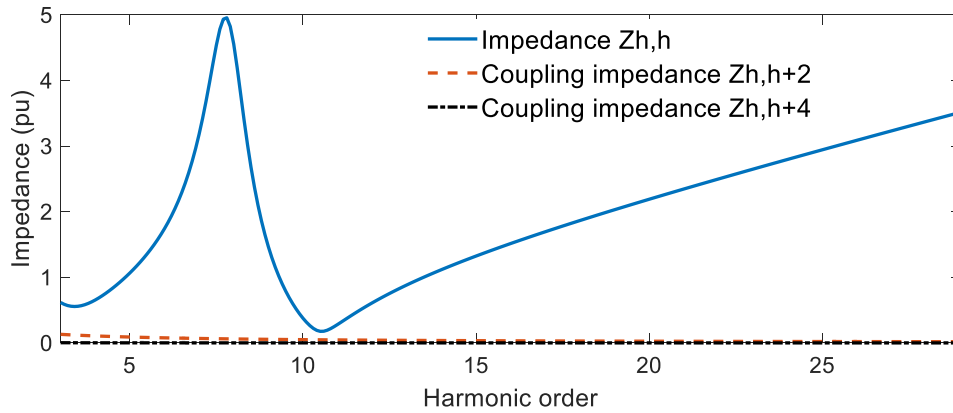


Figure 3-9 Comparison between the diagonal components and nondiagonal impedance in the impedance matrix

The results of time-domain simulations further support the above analysis. Figure 3-10 shows the coupling effect when a negative 5<sup>th</sup> harmonic or positive 7<sup>th</sup> harmonic is added in the ac system in Figure 3-10. The negative 5<sup>th</sup> harmonic indeed introduces a 7<sup>th</sup> harmonic, while the positive sequence 7<sup>th</sup> harmonic introduces a 5<sup>th</sup> harmonic, which matches the theoretical analysis in Section II. However, the coupled voltage is almost negligible compared to the injected harmonics. Therefore, the coupling effect can be omitted in this case.

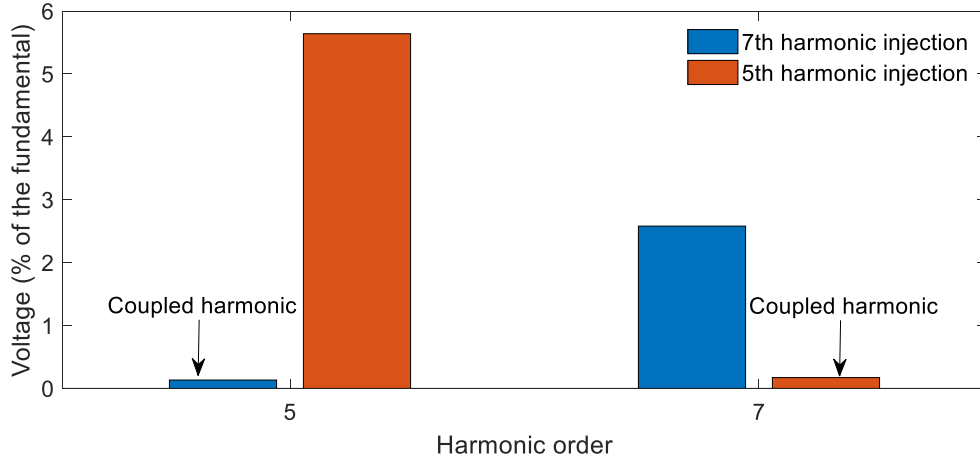


Figure 3-10 Coupling effect in simulations

### 3.2.5 Determination of Model Parameters Using Measurements

Computing the analytical harmonic model requires internal details of VSC equipment. In practice, the manufacturers might be reluctant to provide the control parameters or even the detailed control configurations. In such a situation, a measurement-based method can be used to determine the model parameters. The measurement-based method takes into account the finding that the VSC equipment behaves essentially as impedances at the traditional low-order harmonic frequencies at the operating points of interest. Thus, the impedance can be determined by simply using  $V_h/I_h$  at the connection point (PCC) of the VSC equipment at the operating points of interest. The measurement method can be the lab experiments as described in Section 3.1.2 or the field data after VSC equipment is connected to a power system, taking advantage of the natural harmonic voltage and current at the PCC of VSC equipment. Note that the field-data-based procedure may require long-term monitoring of the harmonics since it needs abundant harmonics observed at the PCC, and the fundamental frequency operating points of the VSC equipment can change in a day.

### 3.3 An Overall Procedure to Construct the Harmonic Model

Based on the impact and data availability of the three operating segments of VSC

equipment, the ideal procedure for constructing the harmonic model is:

- First, the harmonic model of the VSC must include the front-end passive filter since the front-end passive filter has the most contributions to the harmonic model of the VSC. In this model, the VSC impedance can be obtained by assuming that the converter is a short circuit and the VSC is behaving as the front-end filter. This approach, which is easiest to take, may lead to a large error for some harmonics (e.g., the error can reach 32.5% for 7<sup>th</sup> harmonic impedance for the studied system with a 100 $\mu$ F dc-link capacitor).
- Second, the inner current control loop of the VSC is included to improve the accuracy of the harmonic model. This requires knowing the  $H_2(s)$  transfer function in addition to the filter parameters. Including the inner current control will make the VSC impedance model acceptable for many cases. For example, the error of the 7<sup>th</sup> harmonic impedance of the studied system is only 7%.
- Third, the outer control loop and the power loop can be included for further refinement of the model. This step requires knowing more internal parameters of the VSC equipment.
- If no data is available at all, a measurement-based approach explained in section 3.2.5 can be used to determine the VSC impedance model at operating points of interest.

### **3.4 Application of the Proposed Model for Harmonic Power Flow Studies**

The main application of the proposed harmonic model of the VSC, i.e., integrating the proposed model into harmonic power flow studies, is investigated in this section.

A 13-bus IEEE test system [68] was used to show the usefulness of the proposed model for harmonic power flow studies in power systems containing VSC equipment, as shown in Figure 3-11. In this system, there are two VSC-based loads at bus 5 and bus 11 and one LCC-based load at bus 7. The harmonic distortion was

computed using both time-domain simulations and analytical harmonic power flow. For the time domain simulations, the system in Figure 3-11 was modeled in Simulink/MATLAB. The VSC-based loads were modeled on the configuration of the VSC in Figure 2-6. The parameters of the VSC loads are shown in Table 3-4. The LCC-based load is a 6-pulse rectifier.

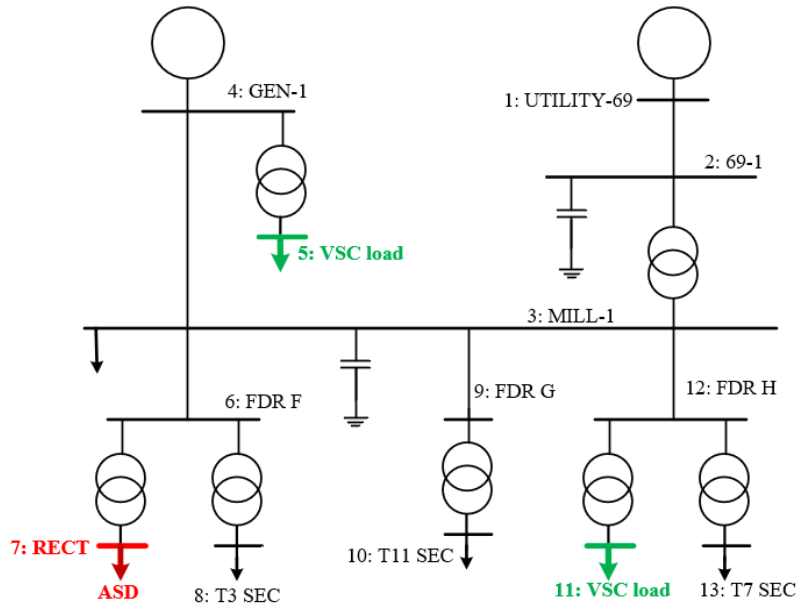


Figure 3-11 An industrial system for harmonic power flow studies

Table 3-4 Parameters of VSC loads

$f_{switch}$	2kHz	$L_2, R_2$	5mL, 0.02 $\Omega$
$L_1, R_1$	5mL, 0.02 $\Omega$	$C, R_c$	100 $\mu$ F, 1 $\Omega$
$H_1$	$k_p=0.033, k_i=2.46$	$H_2$	$k_p=0.693, k_i=1034$
$V_s$	380V	Rating	800kW

Taking advantage of the developed VSC model, a non-iterative harmonic power flow is proposed with the following steps:

1) Conduct the fundamental frequency power flow in the power system by treating LCC equipment and VSC equipment as constant power loads (PQ nodes). The harmonic impedance of the VSC loads can be obtained using equations (2.23). Accordingly, the matrix model of the VSC can be established as equations (2.31).

2) The LCC rectifier is modeled as a harmonic current source ( $I_7(H)$ ). The nodal harmonic current injection is expressed as  $I_{bus}(H)=[0,0,0,0,0,0,I_7(H),0,0,0,0,0]$ ;

3) The rest of the system is linear and can be modeled as a harmonically decoupled admittance matrix as follows:

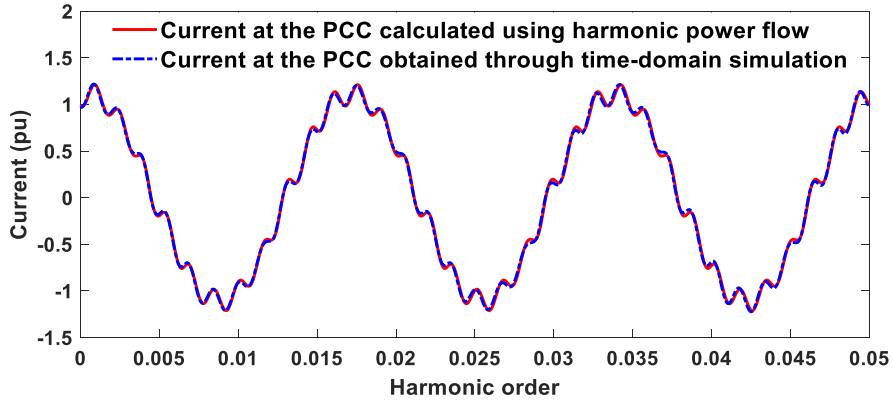
$$\begin{bmatrix} [I]_3 \\ [I]_5 \\ \dots \\ [I]_H \end{bmatrix} = \begin{bmatrix} [Y]_3 & 0 & \dots & 0 \\ 0 & [Y]_5 & \dots & 0 \\ \dots & \dots & \dots & \dots \\ 0 & 0 & \dots & [Y]_H \end{bmatrix} \begin{bmatrix} [V]_3 \\ [V]_5 \\ \dots \\ [V]_H \end{bmatrix} \quad (3.1)$$

(4) Finally, the above equations are integrated to compute the harmonic voltage as

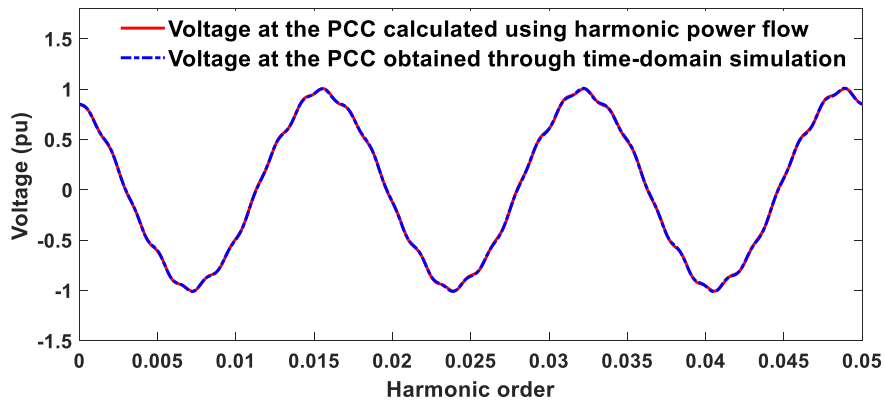
$$V_{bus}(H) = Y_H^{-1} I_{bus}(H) \quad (3.2)$$

where  $V_{bus}$  is the nodal harmonic voltage,  $H$  is the harmonic order interested.

To verify the usefulness of the developed model, the simulated phase-A harmonic voltage and current at the PCC (bus 2) were compared with the calculated phase-A harmonic voltage and current at the PCC using harmonic power flow with the proposed harmonic model. The results of the waveforms of the voltage and current are presented since they provide not only the magnitudes of the harmonics but also the angle information of these harmonics. The results are shown in Figure 3-12, where the calculated voltage and current at the PCC match perfectly with the simulated voltage and current at the PCC. The voltage and current at bus 5, where a VSC load is connected, are also presented in Figure 3-13, and the calculated results also match the simulated results. The above results show that the model can be used to accurately assess the harmonic distortion in VSC-involved power systems.

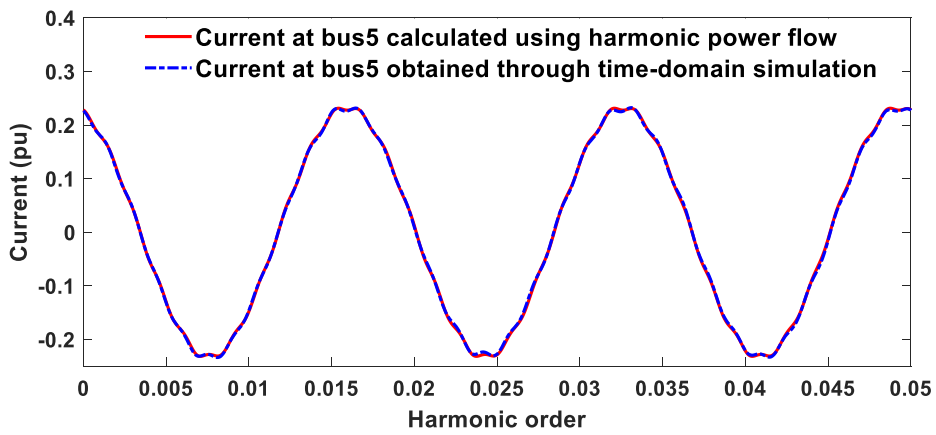


(a) Current waveform

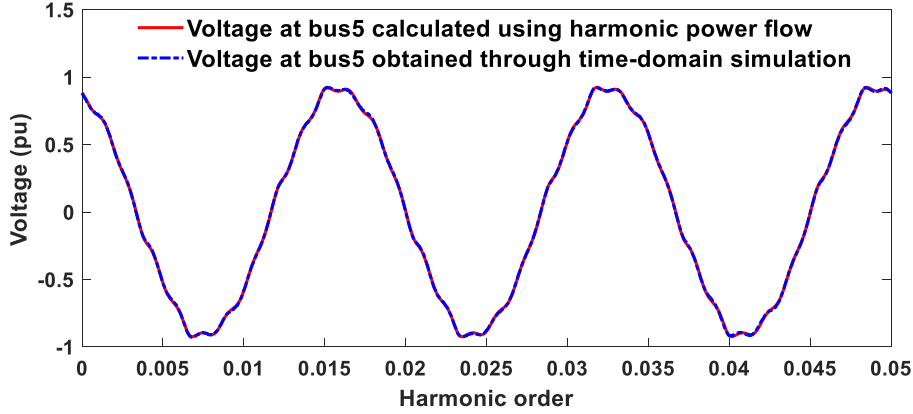


(b) Voltage waveform

Figure 3-12 Calculated and simulated phase-A voltage and current at the PCC



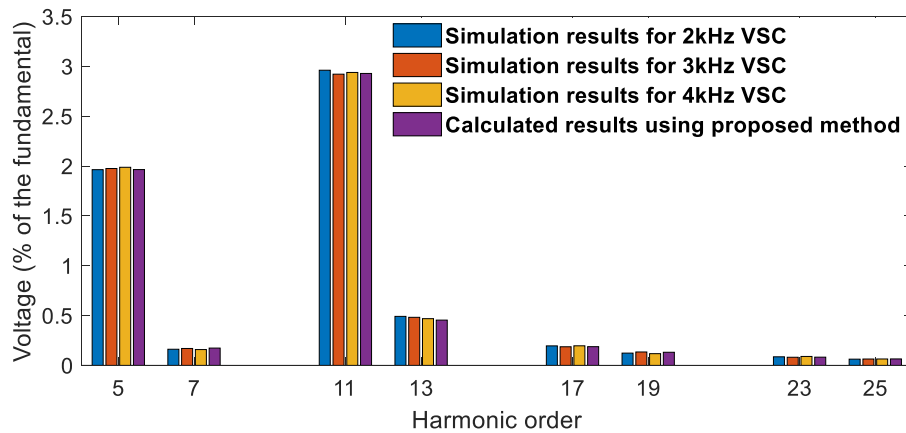
(a) Current waveform



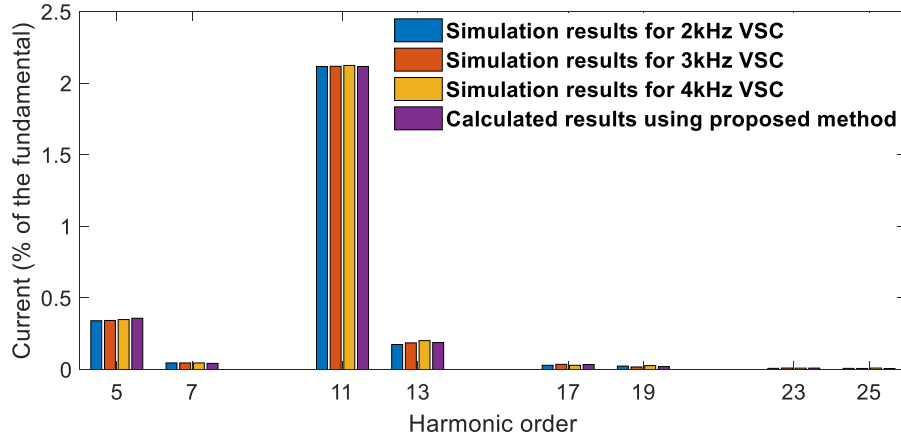
(b) Voltage waveform

Figure 3-13 Calculated and simulated phase-A voltage and current at bus 5

In the studied system in Figure 3-11, the switching frequency of the VSC was as 2 kHz. For comparison, the switching frequency of the VSC is changed to 3 kHz and 4 kHz while other parameters are unchanged. Figure 3-14 compares the spectrums of the voltage and current at bus 5 obtained using time-domain simulations with the spectrums calculated using the proposed model. The simulated spectrums of phase-A voltage and current match the results calculated using the proposed method. The reason is that, according to the designed parameters, the control makes a very limited contribution to the harmonic impedance for harmonics higher than the 10<sup>th</sup>. Therefore, according to the analyses in Section 2.4, the harmonic model of the VSC is not affected by switching frequencies.



(a) Voltage spectrum



(b) Current spectrum

Figure 3-14 Comparison between the voltage and current spectrum obtained through simulations and the spectrum calculated using the proposed method.

To show the importance of including the impedance model of the VSC, an additional case was conducted. In this case, the harmonic power flow was run without the VSC load at the bus 5 VSC at harmonic frequencies (i.e.,  $Z_{VSC}(h)=\infty$ ). The spectrum of the phase-A current at the PCC was compared with the original harmonic power flow results in Figure 3-15. If the impedance model of the VSC at bus 5 was ignored, there was a 28% error for the 11<sup>th</sup> harmonic current. This case illustrates that the impedance model of the VSC must be included in harmonic power flow studies.

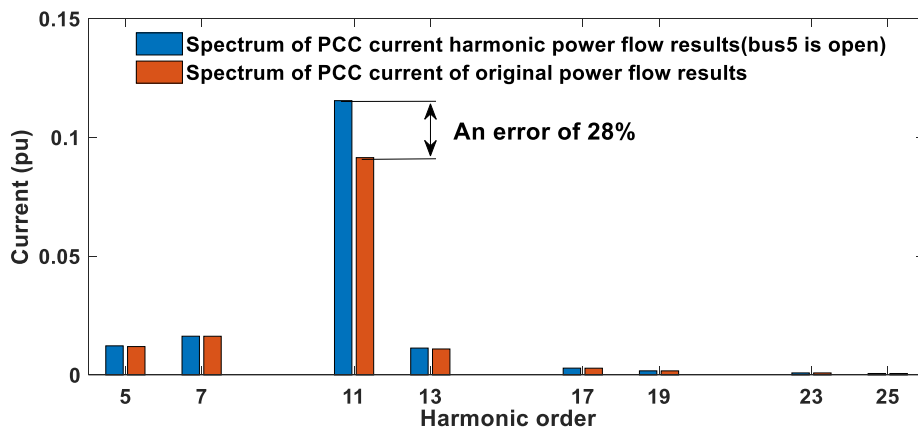


Figure 3-15 Errors of the spectrum of phase-A current at the PCC when assuming the bus 5 load is open

### 3.5 Summary

In this chapter, the proposed harmonic model of the VSC was verified. The chapter's main contributions are:

- The correctness of the proposed harmonic model was verified by time-domain simulations. The impacts of different operating segments on the harmonic model of the VSC were analyzed. The results showed that the control had a significant impact while the dc-link capacitor did not impact the harmonic impedances when the dc-link capacitor was sufficiently large. The chapter also included a proposal for a criterion to help determine whether the power loop needs to be considered.
- Lab experiments verified the main finding that a frequency-dependent impedance could represent the VSC at a specific operating point. Experiments also demonstrated that the dc-link capacitor did not significantly impact the model.
- A practical procedure to construct the developed impedance was presented according to the characteristics of the proposed model.
- The effectiveness of the proposed model for harmonic power flow systems in a complex power system was verified. The results show that the new model can be easily integrated into the harmonic power flow tools.

## Chapter 4

# Extension of the Harmonic Model for Single-phase Voltage Source Converters

Single-phase voltage source converters (VSCs) are widely employed for interfacing solar energy and battery energy storage (BES) in distribution power systems [69][70]. It is essential to understand how the single-phase photovoltaic (PV) affects the harmonics in the single-phase distribution system [71], and a harmonic model is needed for this purpose. Similar to the three-phase VSC, the harmonic model of the single-phase VSC can be established based on its harmonic response mechanism that is determined by the control loop and the power loop. However, the resulting harmonic characteristics of the single-phase VSC are different from those of the three-phase VSC. In particular, the single-phase VSC will inject the 3<sup>rd</sup> harmonic into the connected ac system [72]. As a result, the developed model for the three-phase VSC in Chapter 2 cannot be directly applied to the single-phase VSC. To this end, in this chapter, the harmonic characteristics of the single-phase PV system are analyzed, then an analytical harmonic model of the single-phase PV system is developed through mathematical derivations.

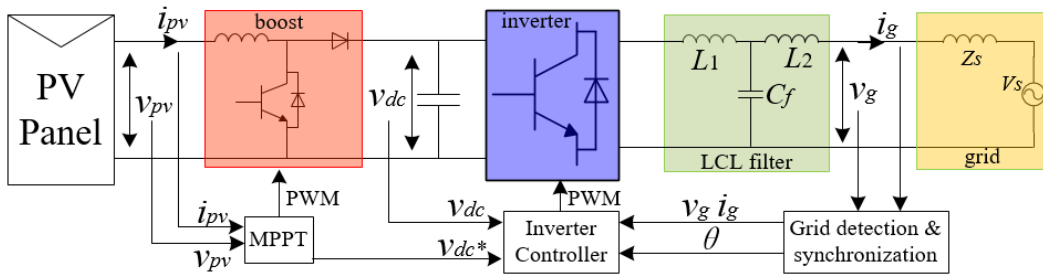
This chapter is organized as follows: Section 4.1 illustrates the harmonic response of a single-phase PV system and reviews existing relevant publications. Section 4.2 looks at the mathematical derivations of the harmonic model for the single-phase PV system. Section 4.3 details the time-domain simulations used to verify the proposed harmonic model. Section 4.4 is a discussion of the 3<sup>rd</sup> harmonic produced by the single-phase VSC in practical residential systems. Section 4.5 contains the chapter summary.

## 4.1 Harmonic Characteristics of a Single-phase PV system

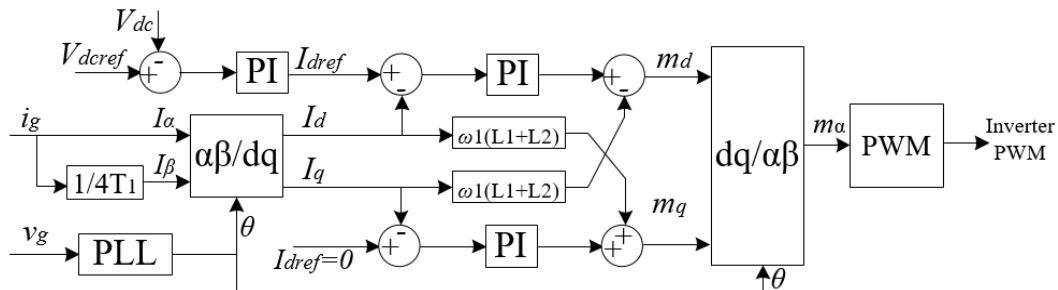
This section presents the characteristics of the harmonic response of single-phase PV systems and the current work on harmonic studies of the single-phase VSC.

### 4.1.1 Harmonic Response of a Single-phase PV System

A typical single-phase PV system shown in Figure 4-1 (a) is used to illustrate the harmonic modeling of the single-phase VSC. In this system, the PV panel is connected to the dc-link capacitor through a boost converter, and then the dc power is transferred to the ac grid through a single-phase inverter. The control scheme of the single-phase inverter is shown in Figure 4-1 (b). The inverter maintains the dc-link voltage and the reactive power that it injected into the grid (usually set as 0). The reactive power and dc-link voltage can be realized by controlling the current at the PCC of the inverter ( $i_g$  in Figure 4-1).



(a) structure of the PV system



(b) the control diagram of the inverter

Figure 4-1 Typical single-phase PV system and the control diagram

The harmonic response of a single-phase VSC is similar to that of a three-phase VSC, as shown in Figure 4-2. The harmonic model of the single-phase VSC can be established by the combined analytical representations of the impacts of the control loop and the power loop. However, the dc side current also contains a 2<sup>nd</sup> harmonic component ( $I_{dc2}$ ) that originates from the interaction between the fundamental frequency components in the modulation signal ( $m_1$ ) and the fundamental frequency components in the ac side current ( $I_{c1}$ ). Further, this 2<sup>nd</sup> harmonic current leads to a 2<sup>nd</sup> harmonic voltage on the dc-link capacitor, which along with the fundamental frequency component in the modulation signal ( $m_1$ ), gives a 3<sup>rd</sup> harmonic voltage on the ac side of the VSC through the switching process. Note that this 3<sup>rd</sup> harmonic voltage exists regardless of the external 3<sup>rd</sup> harmonic distortion, so the single-phase VSC also impacts the system as a voltage source at the 3<sup>rd</sup> harmonic. As to other harmonics, the single-phase does not act as a source, and the combined control loop and power loop will still lead to an impedance model.

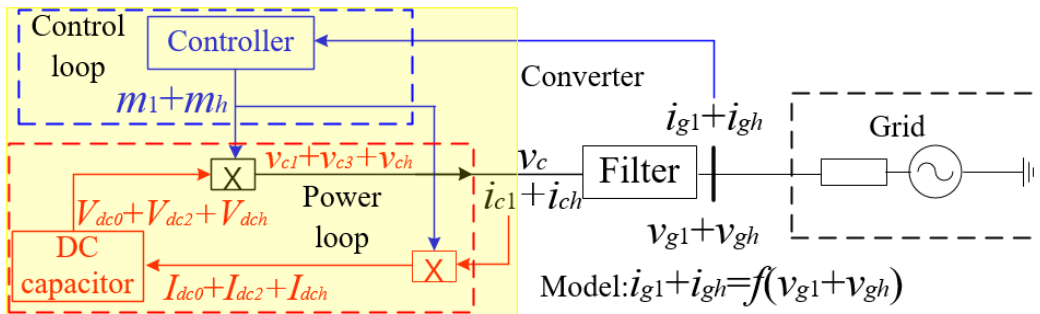


Figure 4-2 Harmonic response of a single-phase VSC

#### 4.1.2 Review of Existing Publications

Existing studies about the harmonic modeling problem of the single-phase VSC are similar to that of the three-phase VSC; they mainly focus on the harmonic resonance problems of the single-phase PV system using the impedance model. The impedance model is established through the analytical representation of the control loop [73][74] or by using only the LCL filter of the single-phase PV and ignoring the control impacts [75]. But these studies do not include the impact of the power loop, so the 3<sup>rd</sup> harmonic is overlooked. Some other publications study the 2<sup>nd</sup>

harmonic on the dc side of the single-phase VSC. But most of these studies focus on the mitigation of the 2<sup>nd</sup> harmonics on the dc-link [76]-[78]. Only [72] presents the computation of the 3<sup>rd</sup> harmonic using the closed-form solutions, but the computation method is indirect and relatively complex. Therefore, a sound model that fully represents the harmonic characteristics of the single-phase VSC is still needed.

## 4.2 Harmonic Modeling of Single-phase VSC

The harmonic model of the single-phase VSC can be established similar to that used for the three-phase VSC. The control loop can be analyzed to establish the analytical representation of the modulation signal. The resulting modulation signal can be used to establish the analytical expression of the power loop. Combining analytical expressions of the control loop and power loop can get the harmonic model of the single-phase VSC.

### 4.2.1 abc/dq Conversion in Single-phase VSC

The steady-state voltage and current at the PCC that contain harmonics can be expressed as

$$\begin{aligned} v_g &= V_{g1} \cos(\omega_1 t + \theta_{g1}) + \sum V_{gh} \cos(\omega_h t + \theta_{gh}) \\ i_g &= I_{g1} \cos(\omega_1 t + \delta_{g1}) + \sum I_{gh} \cos(\omega_h t + \delta_{gh}) \end{aligned} \quad (4.1)$$

where  $V$  and  $I$  stand for voltage and current,  $\omega$  is the angular frequency,  $h$  is the harmonic order, “1” represents the fundamental frequency, and  $\theta$  and  $\delta$  are the angles of voltage and current, respectively. Since the control is implemented in the  $dq$  frame, the above voltage and current have to be converted into  $dq$ -frame quantities. However, no transformation can be used for direct  $abc/dq$  conversion for single-phase voltage and current. So, the ac voltage and current are first converted into the  $\alpha\beta$  frame by taking the original voltage and current as the  $\alpha$ -axis voltage/current and creating the  $\beta$ -axis voltage/current by adding a 1/4 fundamental-frequency period delay in the original voltage and current (i.e., a 90°

delay for the fundamental frequency voltage and current). Accordingly, the  $\alpha\beta$ -frame voltage and current can be expressed as

$$\begin{aligned}
v_{g\alpha} &= V_{g1} \cos(\omega_1 t + \theta_{g1}) + \sum V_{gh} \cos(\omega_h t + \theta_{gh}) \\
v_{g\beta} &= V_{g1} \cos(\omega_1 t + \theta_{g1} - \frac{\pi}{2}) + \sum V_{gh} \cos(\omega_h t + \theta_{gh} - \frac{h\pi}{2}) \\
i_{g\alpha} &= I_{g1} \cos(\omega_1 t + \delta_{g1}) + \sum I_{gh} \cos(\omega_h t + \delta_{gh}) \\
i_{g\beta} &= I_{g1} \cos(\omega_1 t + \delta_{g1} - \frac{\pi}{2}) + \sum I_{gh} \cos(\omega_h t + \delta_{gh} - \frac{h\pi}{2})
\end{aligned} \tag{4.2}$$

The  $\alpha\beta$ -frame voltage and current are converted to the  $dq$  frame using (4.3)

$$\begin{bmatrix} f_d \\ f_q \end{bmatrix} = \begin{bmatrix} \cos(\omega_1 t + \theta_{g1}) & \sin(\omega_1 t + \theta_{g1}) \\ -\sin(\omega_1 t + \theta_{g1}) & \cos(\omega_1 t + \theta_{g1}) \end{bmatrix} \begin{bmatrix} f_\alpha \\ f_\beta \end{bmatrix} \tag{4.3}$$

where  $f$  stands for voltage or current. Accordingly, the voltage and current in the  $dq$  frame can be obtained as

$$\begin{aligned}
v_{gd} &= V_{g1} \cos(\omega_1 t + \theta_{g1}) \cos(\omega_1 t + \theta_{g1}) + \sum V_{gh} \cos(\omega_h t + \theta_{gh}) \cos(\omega_1 t + \theta_{g1}) \\
&+ V_{g1} \sin(\omega_1 t + \theta_{g1}) \sin(\omega_1 t + \theta_{g1}) + \sum V_{gh} \cos(\omega_h t + \theta_{gh} - \frac{h\pi}{2}) \sin(\omega_1 t + \theta_{g1}) \\
&= V_{g1} + \sum \frac{1}{2} V_{gh} \cos(\omega_h t + \theta_{gh} + \omega_1 t + \theta_{g1}) \left[ 1 + \cos(\frac{h\pi + \pi}{2}) \right] \\
&+ \sum \frac{1}{2} V_{gh} \cos(\omega_h t + \theta_{gh} - \omega_1 t - \theta_{g1}) \left[ 1 - \cos(\frac{h\pi + \pi}{2}) \right]
\end{aligned} \tag{4.4}$$

$$\begin{aligned}
v_{gq} &= -V_{g1} \cos(\omega_1 t + \theta_{g1}) \sin(\omega_1 t + \theta_{g1}) - \sum V_{gh} \cos(\omega_h t + \theta_{gh}) \sin(\omega_1 t + \theta_{g1}) \\
&+ V_{g1} \sin(\omega_1 t + \theta_{g1}) \cos(\omega_1 t + \theta_{g1}) + \sum V_{gh} \cos(\omega_h t + \theta_{gh} - \frac{h\pi}{2}) \cos(\omega_1 t + \theta_{g1}) \\
&= -\frac{1}{2} \sum V_{gh} \sin(\omega_h t + \theta_{gh} + \omega_1 t + \theta_{g1}) \left[ 1 + \cos(\frac{h\pi + \pi}{2}) \right] \\
&+ \frac{1}{2} \sum V_{gh} \sin(\omega_h t + \theta_{gh} - \omega_1 t - \theta_{g1}) \left[ 1 - \cos(\frac{h\pi + \pi}{2}) \right]
\end{aligned} \tag{4.5}$$

$$\begin{aligned}
i_{gd} &= I_{g1} \cos(\omega_1 t + \delta_{g1}) \cos(\omega_1 t + \theta_{g1}) + \sum I_{gh} \cos(\omega_h t + \delta_{gh}) \cos(\omega_1 t + \theta_{g1}) \\
&+ I_{g1} \sin(\omega_1 t + \delta_{g1}) \sin(\omega_1 t + \theta_{g1}) + \sum V_{gh} \cos(\omega_h t + \delta_{gh} - \frac{h\pi}{2}) \sin(\omega_1 t + \theta_{g1}) \\
&= I_{g1} \cos(\delta_{g1} - \theta_{g1}) + \frac{1}{2} \sum I_{gh} \cos(\omega_h t + \delta_{gh} + \omega_1 t + \theta_{g1}) \left[ 1 + \cos\left(\frac{h\pi + \pi}{2}\right) \right] \\
&+ \frac{1}{2} \sum I_{gh} \cos(\omega_h t + \delta_{gh} - \omega_1 t - \theta_{g1}) \left[ 1 - \cos\left(\frac{h\pi + \pi}{2}\right) \right]
\end{aligned} \tag{4.6}$$

$$\begin{aligned}
i_{gq} &= -I_{g1} \cos(\omega_1 t + \delta_{g1}) \sin(\omega_1 t + \theta_{g1}) - \sum I_{gh} \cos(\omega_h t + \delta_{gh}) \sin(\omega_1 t + \theta_{g1}) \\
&+ I_{g1} \sin(\omega_1 t + \delta_{g1}) \cos(\omega_1 t + \theta_{g1}) + \sum I_{gh} \cos(\omega_h t + \delta_{gh} - \frac{h\pi}{2}) \cos(\omega_1 t + \theta_{g1}) \\
&= I_{g1} \sin(\delta_{g1} - \theta_{g1}) - \frac{1}{2} \sum I_{gh} \sin(\omega_h t + \delta_{gh} + \omega_1 t + \theta_{g1}) \left[ 1 + \cos\left(\frac{h\pi + \pi}{2}\right) \right] \\
&+ \frac{1}{2} \sum I_{gh} \sin(\omega_h t + \delta_{gh} - \omega_1 t - \theta_{g1}) \left[ 1 - \cos\left(\frac{h\pi + \pi}{2}\right) \right]
\end{aligned} \tag{4.7}$$

The above  $dq$ -frame voltage and current show that, in the single-phase VSC, the harmonic  $\omega_h$  on the ac side of the VSC could be either  $\omega_h - \omega_1$  or  $\omega_h + \omega_1$  in the  $dq$  frame depending on the  $h$  value. For example, a 5<sup>th</sup> harmonic on the ac side of the VSC leads to a 4<sup>th</sup> harmonic in the  $dq$  frame, while a 7<sup>th</sup> harmonic leads to an 8<sup>th</sup> harmonic in the  $dq$  frame.

#### 4.2.2 Modulation Signal of PWM Switching

With the above obtained  $dq$ -frame voltage and current, the modulation signal can be computed. The dc-link voltage control is established through the outer control loop. The impact of this type of outer control loop is very limited (the reason will be explained in Section 4.3). Consequently, it is reasonable to assume that the outer control loop does not produce any low-order harmonics in the reference current of the inner current control loop (i.e.,  $I_{gdref}$  and  $I_{gqref}$  are harmonic free). Therefore, only the inner control loop is considered. Accordingly, the output of the inner control can be written as

$$\begin{aligned}
v_{dh} &= -\frac{1}{2}H(s+j\omega_1)I_{gh} \cos(\omega_h t + \delta_{gh} + \omega_1 t + \theta_{g1}) \left[ 1 + \cos\left(\frac{h\pi + \pi}{2}\right) \right] \\
&\quad -\frac{1}{2}H(s-j\omega_1)I_{gh} \cos(\omega_h t + \delta_{gh} - \omega_1 t - \theta_{g1}) \left[ 1 - \cos\left(\frac{h\pi + \pi}{2}\right) \right] \\
v_{qh} &= \frac{1}{2}H(s+j\omega_1)I_{gh} \sin(\omega_h t + \delta_{gh} + \omega_1 t + \theta_{g1}) \left[ 1 + \cos\left(\frac{h\pi + \pi}{2}\right) \right] \\
&\quad -\frac{1}{2}H(s-j\omega_1)I_{gh} \sin(\omega_h t + \delta_{gh} - \omega_1 t - \theta_{g1}) \left[ 1 - \cos\left(\frac{h\pi + \pi}{2}\right) \right]
\end{aligned} \tag{4.8}$$

The above  $dq$ -frame signal is converted back to the  $\alpha\beta$  frame, and the harmonic components of the  $\alpha$ -axis signal can be written as

$$\begin{aligned}
v_{\alpha h} &= - \left\{ \begin{aligned} &\frac{1}{2}H(s+j\omega_1)I_{gh} \cos(\omega_h t + \delta_{gh} + \omega_1 t + \theta_{g1}) \left[ 1 + \cos\left(\frac{h\pi + \pi}{2}\right) \right] \\ &+ \frac{1}{2}H(s-j\omega_1)I_{gh} \cos(\omega_h t + \delta_{gh} - \omega_1 t - \theta_{g1}) \left[ 1 - \cos\left(\frac{h\pi + \pi}{2}\right) \right] \end{aligned} \right\} \cos(\omega_1 t + \theta_{g1}) \\
&\quad - \left\{ \begin{aligned} &-\frac{1}{2}H(s+j\omega_1)I_{gh} \sin(\omega_h t + \delta_{gh} + \omega_1 t + \theta_{g1}) \left[ 1 + \cos\left(\frac{h\pi + \pi}{2}\right) \right] \\ &+ \frac{1}{2}H(s-j\omega_1)I_{gh} \sin(\omega_h t + \delta_{gh} - \omega_1 t - \theta_{g1}) \left[ 1 - \cos\left(\frac{h\pi + \pi}{2}\right) \right] \end{aligned} \right\} \sin(\omega_1 t + \theta_{g1}) \\
&= -\frac{1}{2}I_{gh}H(s+j\omega_1) \cos(\omega_h t + \delta_{gh}) \left[ 1 + \cos\left(\frac{h\pi + \pi}{2}\right) \right] \\
&\quad -\frac{1}{2}I_{gh}H(s-j\omega_1) \cos(\omega_h t + \delta_{gh}) \left[ 1 - \cos\left(\frac{h\pi + \pi}{2}\right) \right]
\end{aligned} \tag{4.9}$$

And the harmonic components in the modulation signal can be given as

$$m_h = (\sqrt{2}V_{nom} / V_{dc0})v_{\alpha h} \tag{4.10}$$

where  $V_{nom}$  is the nominal voltage. (4.9) and (4.10) show that the harmonic components in the modulation signal exhibit a linear relationship with the harmonic components in the steady-state current at the PCC.

### 4.2.3 Modeling of the Impact of the Power Loop

Based on the above analysis, with the presence of the harmonic components in

the steady-state current at the PCC, the modulation signal can include that harmonic as well. The steady-state current on the ac side of the VSC can also include that harmonic. Therefore, the modulation signal and the current on the ac side of the converter can be expressed as

$$m = m_1 \cos(\omega_1 t + \alpha_1) + \sum m_h \cos(\omega_h t + \alpha_h) \quad (4.11)$$

$$I_c = I_{c1} \cos(\omega_1 t + \delta_{c1}) + \sum I_{ch} \cos(\omega_h t + \delta_{ch}) \quad (4.12)$$

where c stands for the converter and  $\alpha$  is the angle of the modulation signal. The current on the dc side of the converter can be expressed as

$$\begin{aligned} I_{dc} &= \left\{ m_1 \cos(\omega_1 t + \alpha_1) + \sum m_h \cos(\omega_h t + \alpha_h) \right\} \cdot \left\{ I_{c1} \cos(\omega_1 t + \delta_{c1}) + \sum I_{ch} \cos(\omega_h t + \delta_{ch}) \right\} \\ &= I_{dc0} + \frac{1}{2} m_1 I_{c1} \cos(2\omega_1 t + \alpha_1 + \delta_{c1}) + \frac{1}{2} \sum I_{ch} m_1 \cos(\omega_h t + \delta_{ch} + \omega_1 t + \alpha_1) \\ &\quad + \frac{1}{2} \sum I_{ch} m_1 \cos(\omega_h t + \delta_{ch} - \omega_1 t - \alpha_1) + \frac{1}{2} \sum m_h I_{c1} \cos(\omega_h t + \alpha_h + \omega_1 t + \delta_{c1}) \\ &\quad + \frac{1}{2} \sum m_h I_{c1} \cos(\omega_h t + \alpha_h - \omega_1 t - \delta_{c1}) + \sum_{m,n \in h} m_m I_{cn} \cos(\omega_m t + \alpha_m) \cos(\omega_n t + \delta_{cn}) \end{aligned} \quad (4.13)$$

In the above current, the components that are introduced by the interaction between different harmonics can be omitted due to the small magnitudes. When passing through the dc-link capacitor, the harmonic components in the above current result in the dc-link voltage as

$$\begin{aligned} V_{dc} &= V_{dc0} + \frac{m_1 I_{c1}}{4C_{dc} \omega_1} \cos(2\omega_1 t + \alpha_1 + \delta_{c1} - \frac{\pi}{2}) + \sum \frac{I_{ch} m_1}{2C_{dc} (\omega_h + \omega_1)} \cos(\omega_h t + \delta_{ch} + \omega_1 t + \alpha_1 - \frac{\pi}{2}) \\ &\quad + \sum \frac{I_{ch} m_1}{2C_{dc} (\omega_h - \omega_1)} \cos(\omega_h t + \delta_{ch} - \omega_1 t - \alpha_1 - \frac{\pi}{2}) + \sum \frac{m_h I_{c1}}{2C_{dc} (\omega_h + \omega_1)} \cos(\omega_h t + \alpha_h + \omega_1 t + \delta_{c1} - \frac{\pi}{2}) \\ &\quad + \frac{m_h I_{c1}}{2C_{dc} (\omega_h - \omega_1)} \cos(\omega_h t + \alpha_h - \omega_1 t - \delta_{c1} - \frac{\pi}{2}) \end{aligned} \quad (4.14)$$

The above equation is obtained by assuming all harmonic components in the dc-side current pass through the dc-link capacitor. Notably, the dc-side PV panel can

also be regarded as an equivalent impedance and can be addressed as described in the three-phase VSC. The above dc-link voltage is related to the voltage on the ac side of the VSC through the switching process, and the expression is

$$\begin{aligned}
V_{ac} = mV_{dc} = & V_{dc0}m_1 \cos(\omega_1 t + \alpha_1) + \frac{m_1^2 I_{c1}}{8C_{dc}\omega_1} \cos(\omega_1 t + \delta_{c1} - \frac{\pi}{2}) \\
& + \frac{m_1^2 I_{c1}}{8C_{dc}\omega_1} \cos(3\omega_1 t + 2\alpha_1 + \delta_{c1} - \frac{\pi}{2}) + \frac{I_{ch}m_1^2}{4C_{dc}(\omega_h + \omega_1)} \cos(\omega_h t + \delta_{ch} + 2\omega_1 t + 2\alpha_1 - \frac{\pi}{2}) \\
& + \frac{I_{ch}m_1^2}{4C_{dc}(\omega_h + \omega_1)} \cos(\omega_h t + \delta_{ch} - \frac{\pi}{2}) + \frac{I_{ch}m_1^2}{4C_{dc}(\omega_h - \omega_1)} \cos(\omega_h t + \delta_{ch} - \frac{\pi}{2}) \\
& + \frac{I_{ch}m_1^2}{4C_{dc}(\omega_h - \omega_1)} \cos(\omega_h t + \delta_{ch} - 2\omega_1 t - 2\alpha_1 - \frac{\pi}{2}) + \frac{m_1 m_h I_{c1}}{4C_{dc}(\omega_h + \omega_1)} \cos(\omega_h t + \alpha_h + \delta_{c1} - \alpha_1 - \frac{\pi}{2}) \\
& + \frac{m_1 m_h I_{c1}}{4C_{dc}(\omega_h + \omega_1)} \cos(\omega_h t + \alpha_h + 2\omega_1 t + \alpha_1 + \delta_{c1} - \frac{\pi}{2}) + \frac{m_1 m_h I_{c1}}{4C_{dc}(\omega_h - \omega_1)} \cos(\omega_h t + \alpha_h + \alpha_1 - \delta_{c1} - \frac{\pi}{2}) \\
& + \frac{m_1 m_h I_{c1}}{4C_{dc}(\omega_h - \omega_1)} \cos(\omega_h t + \alpha_h - 2\omega_1 t - \delta_{c1} - \alpha_1 - \frac{\pi}{2}) + V_{dc0}m_h \cos(\omega_h t + \alpha_h)
\end{aligned} \tag{4.15}$$

Substituting the modulation signal in (4.10) into (4.15) and extracting the harmonic components from the ac voltage, the harmonic components in the voltage on the ac side of the converter can be expressed as

$$\begin{aligned}
V_{ach} = & \left\{ \frac{V_{dc0}}{\sqrt{2}V_{nom}} \right\} H(s \pm j\omega_1) I_{gh} \cos(\omega_h t + \delta_{gh}) + \\
& \left\{ \frac{-jm_1 P_{nom} I_{c1} e^{j(\delta_{c1} - \alpha_1)}}{4V_{nom}^2 C_{dc}(\omega_h + \omega_1)} + \frac{-jm_1 P_{nom} I_{c1} e^{j(-\delta_{c1} + \alpha_1)}}{4V_{nom}^2 C_{dc}(\omega_h - \omega_1)} \right\} H(s \pm j\omega_1) I_{gh} \cos(\omega_h t + \delta_{gh}) \\
& + \left\{ \frac{-jm_1^2 P_{nom}}{4V_{nom}^2 C_{dc}(\omega_h + \omega_1)} + \frac{-jm_1^2 P_{nom}}{4V_{nom}^2 C_{dc}(\omega_h - \omega_1)} \right\} I_{ch} \cos(\omega_h t + \delta_{ch}) \\
& + \frac{I_{ch} P_{nom} m_1^2}{4C_{dc} V_{nom}^2 (\omega_h + \omega_1)} \cos(\omega_h t + \delta_{ch} + 2\omega_1 t + 2\alpha_1 - \frac{\pi}{2}) \\
& + \frac{I_{ch} P_{nom} m_1^2}{4C_{dc} V_{nom}^2 (\omega_h - \omega_1)} \cos(\omega_h t + \delta_{ch} - 2\omega_1 t - 2\alpha_1 - \frac{\pi}{2}) \\
& + \frac{m_1 P_{nom} I_{c1}}{4C_{dc} V_{nom}^2 (\omega_h + \omega_1)} m_h \cos(\omega_h t + \alpha_h + 2\omega_1 t + \alpha_1 + \delta_{c1} - \frac{\pi}{2}) \\
& + \frac{m_1 P_{nom} I_{c1}}{4C_{dc} V_{nom}^2 (\omega_h - \omega_1)} m_h \cos(\omega_h t + \alpha_h - 2\omega_1 t - \delta_{c1} - \alpha_1 - \frac{\pi}{2}) \\
& + \frac{m_1^2 P_{nom} I_{c1}}{8C_{dc} V_{nom}^2} \cos(3\omega_1 t + 2\gamma_1 + \delta_{c1} - \frac{\pi}{2})
\end{aligned} \tag{4.16}$$

#### 4.2.4 Overall Harmonic Model of the Single-phase VSC

The obtained harmonic voltage in (4.16) can be related to the harmonic voltage and current at the PCC through the front-end LCL filter. The expression can be written as

$$V_{ch} = \frac{Z_{L1} + Z_{Cf}}{Z_{Cf}} V_{gh} - (Z_{L1} Z_{L2} + Z_{L1} Z_{Cf} + Z_{L2} Z_{Cf}) I_{gh} \tag{4.17}$$

Combining (4.16) and (4.17), we can have the following model:

$$\begin{bmatrix} V_{g3} \\ V_{g5} \\ V_{g7} \\ \dots \\ V_{gh} \end{bmatrix} = \begin{bmatrix} V_{gs3} \\ 0 \\ 0 \\ \dots \\ 0 \end{bmatrix} + \begin{bmatrix} Z_{3,3} & Z_{3,5} & 0 & \dots & 0 \\ Z_{3,5} & Z_{5,5} & Z_{5,7} & \dots & 0 \\ 0 & Z_{7,5} & Z_{7,7} & \dots & 0 \\ \dots & \dots & \dots & \dots & \dots \\ 0 & 0 & 0 & \dots & Z_{h,h} \end{bmatrix} \begin{bmatrix} I_{g3} \\ I_{g5} \\ I_{g7} \\ \dots \\ I_{gh} \end{bmatrix} \tag{4.18}$$

And the impedances in (4.18) can be written as

$$Z_{h,h} = \frac{Z_{L1}(Z_{L2} + k_2) + Z_{L1}Z_{C_f} + (Z_{L2} + k_2)Z_{C_f} + k_1H(s \pm j\omega_1)Z_{C_f}}{Z_{L2} + Z_{C_f}} \quad (4.19)$$

$$k_1 = 1 + \frac{-jm_1I_{t1}e^{j(\delta_{t1}-\gamma_1)}}{4V_{dc0}C_{dc}(\omega_h + \omega_1)} + \frac{-jm_1I_{t1}e^{j(-\delta_{t1}+\gamma_1)}}{4V_{dc0}C_{dc}(\omega_h + \omega_1)} \quad (4.20)$$

$$k_2 = \frac{-jm_1^2P_{nom}}{4V_{nom}^2C_{dc}(\omega_h + \omega_1)} + \frac{-jm_1^2P_{nom}}{4V_{nom}^2C_{dc}(\omega_h - \omega_1)} \quad (4.21)$$

$$Z_{h-2,h} = \frac{m_1^2 e^{j(-2\gamma_1 - \frac{\pi}{2})} Z_{C_f}^2 Z_s}{4C_{dc}(\omega_h - \omega_1)(Z_{L1} + Z_{h,h})(Z_{L1}Z_{C_f} + Z_sZ_{C_f} + Z_{L2}Z_{C_f} + Z_{L1}Z_{L2} + Z_{L2}Z_s)} + \frac{m_1I_{t1}e^{j(-\delta_{t1}-\gamma_1-\frac{\pi}{2})} H(s \pm j\omega_1)Z_{CC_f}Z_s}{4C_{dc}(\omega_h - \omega_1)(Z_{L1}Z_{C_f} + Z_sZ_{C_f} + Z_{L2}Z_{C_f} + Z_{L1}Z_{L2} + Z_{L2}Z_s)} \quad (4.22)$$

$$Z_{h+2,h} = \frac{m_1^2 e^{j(2\gamma_1 - \frac{\pi}{2})} Z_{C_f}^2 Z_s}{4C_{dc}(\omega_h + \omega_1)(Z_{L1} + Z_{h,h})(Z_{L1}Z_{C_f} + Z_sZ_{C_f} + Z_{L2}Z_{C_f} + Z_{L1}Z_{L2} + Z_{L2}Z_s)} + \frac{m_1I_{t1}e^{j(\delta_{t1}+\gamma_1-\frac{\pi}{2})} H(s \pm j\omega_1)Z_{C_f}Z_s}{4C_{dc}(\omega_h + \omega_1)(Z_{L1}Z_{C_f} + Z_sZ_{C_f} + Z_{L2}Z_{C_f} + Z_{L1}Z_{L2} + Z_{L2}Z_s)} \quad (4.23)$$

$$V_{gs3} = \frac{Z_{C_f}m_1^2I_{c1}e^{j(2\gamma_1+\delta_{t1}-\frac{\pi}{2})}}{8C_{dc}(Z_{C_f} + Z_{L2})} \quad (4.24)$$

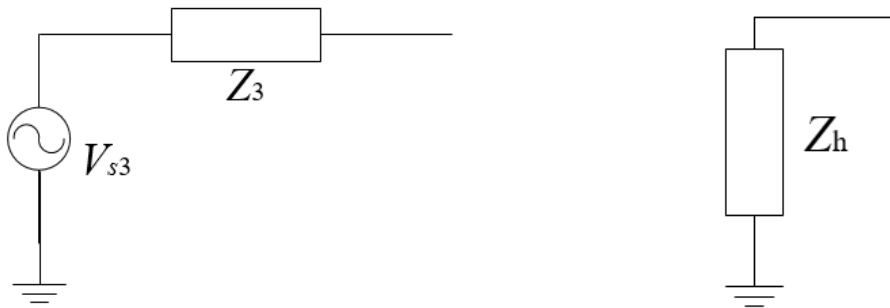
The equation (4.24) validates the analysis in Section 4.1.1, which says that the single-phase VSC will produce a 3<sup>rd</sup> harmonic voltage on the ac side of the VSC. The 3<sup>rd</sup> harmonic voltage source will lead to a 3<sup>rd</sup> harmonic current at the PCC, which will also introduce a 5<sup>th</sup> (and 7<sup>th</sup>, 9<sup>th</sup>, and so on) harmonic voltage source because of the coupling mechanism. But the 5<sup>th</sup> harmonic voltage introduced by the coupling mechanism was quite small (0.69% of the 3<sup>rd</sup> voltage source in the studied system in Section 4.3), and other coupling-introduced harmonics were even smaller.

Therefore, the coupling-induced harmonic voltage sources can be omitted, and the final model can be written as

$$\begin{bmatrix} V_{g3} \\ V_{g5} \\ V_{g7} \\ \dots \\ V_{gh} \end{bmatrix} = \begin{bmatrix} V_{gs3} \\ 0 \\ 0 \\ \dots \\ 0 \end{bmatrix} + \begin{bmatrix} Z_{3,3} & 0 & 0 & \dots & 0 \\ 0 & Z_{5,5} & 0 & \dots & 0 \\ 0 & 0 & Z_{7,7} & \dots & 0 \\ \dots & \dots & \dots & \dots & \dots \\ 0 & 0 & 0 & \dots & Z_{h,h} \end{bmatrix} \begin{bmatrix} I_{g3} \\ I_{g5} \\ I_{g7} \\ \dots \\ I_{gh} \end{bmatrix} \quad (4.25)$$

The following critical findings can be extrapolated from the above equations:

- There is a 3<sup>rd</sup> harmonic voltage source on the ac side of the converter, which is determined by the fundamental frequency voltage and current. Thus, the single-phase VSC acts as a harmonic source to the system. The 3<sup>rd</sup> harmonic voltage on the ac side of the VSC can also be affected by the external 3<sup>rd</sup> harmonic from the grid side. Overall, the single-phase VSC can be represented as a Thevenin circuit, as shown in Figure 4-3 (a).
- For harmonics higher than the 3<sup>rd</sup> (e.g., 5<sup>th</sup>~29<sup>th</sup>), the harmonic components on the ac side voltage are a response to the external harmonics. Like the three-phase VSC, the coupling effect between different harmonics is negligible so that the single-phase VSC acts as an impedance for 5<sup>th</sup>~29<sup>th</sup> harmonics, as shown in Figure 4-3 (b).



(a) Thevenin circuit at 3<sup>rd</sup> harmonic      (b) Impedance model at 5<sup>th</sup>~29<sup>th</sup> harmonic

Figure 4-3 Harmonic model of single-phase VSC

### 4.3 Verification of the Proposed Model Via Time-domain Simulations

The proposed harmonic model of the single-phase PV was tested by time-domain simulations using the system in Figure 2-6. The system parameters are presented in Table 4-1. The system is modeled in MATLAB/Simulink. The impedances for 5<sup>th</sup>~29<sup>th</sup> harmonics were verified first, and then the Thevenin circuit for the 3<sup>rd</sup> harmonic was validated.

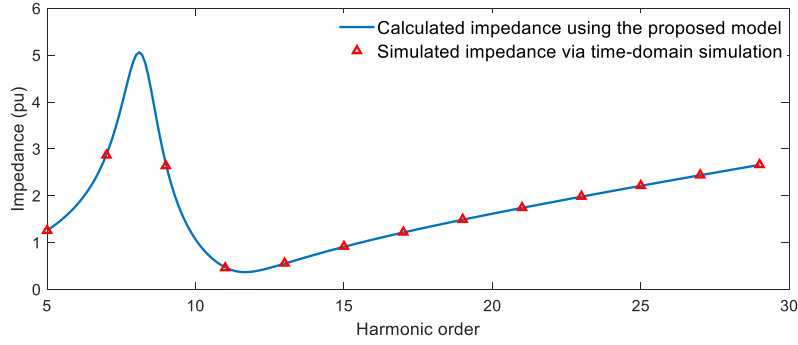
Table 4-1 Parameters of the studied single-phase PV system

$V_s$	120V	$Z_{L1}$	0.008+0.823i ( $\Omega$ )
$Z_s$	0.008+0.823i ( $\Omega$ )	$Z_{L2}$	0.008+0.823i ( $\Omega$ )
$Z_{Cf}$	2.19+109i ( $\Omega$ )	$C_{dc}$	3000 $\mu$ F
Power	3500W	Switching	3780Hz

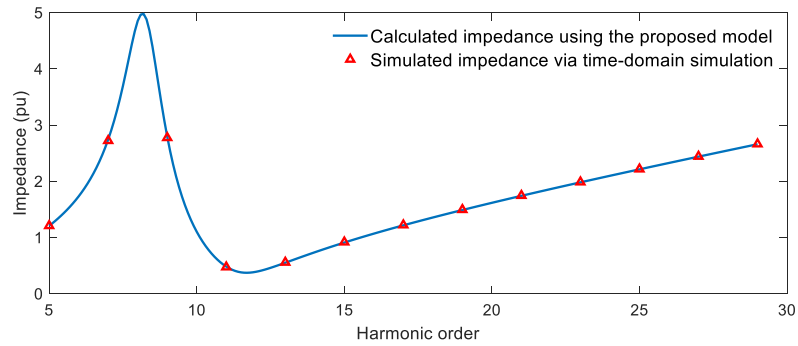
#### 4.3.1 Verification of Harmonic Impedances at 5<sup>th</sup>~29<sup>th</sup> Harmonics

##### A. Verification of the Correctness of the Harmonic Impedance

The impedances of the single-phase PV at the 5<sup>th</sup>~29<sup>th</sup> harmonics were verified via time-domain simulations in the studied single-phase PV system. For the simulations, various odd harmonics of different distortions were added to the voltage source of the system ( $V_s$ ). The simulated impedances were obtained through the harmonic voltage and current ( $v_{gh}/i_{gh}$ ). The calculated impedance using the proposed model was compared with the simulated impedance via time-domain simulations for a dc-link of 3000 $\mu$ F. The results are shown in Figure 4-4. The calculated impedances match perfectly with the simulated impedances, which verifies the correctness of the proposed model. In the simulations, the IHD of one harmonic voltage was up to 20% but the results were the same, indicating that the proposed impedance model is linear.



(a) a dc-link capacitor of 3000µF



(a) a dc-link capacitor of 300µF

Figure 4-4 Comparison between the calculated impedances and simulated impedances

### B. Impact of the DC-link Capacitor

To show the impact of the dc-link capacitor, the calculated impedances for the dc-link capacitor of 3000µF and 300µF, as well as the harmonic impedance for an infinite dc-link capacitor, are compared in Figure 4-5. The dc-link does not have a significant impact on the harmonic impedance even when the dc-link capacitor is reduced to 300µF. Therefore, in most cases, the impacts of the dc-link capacitor are almost negligible.

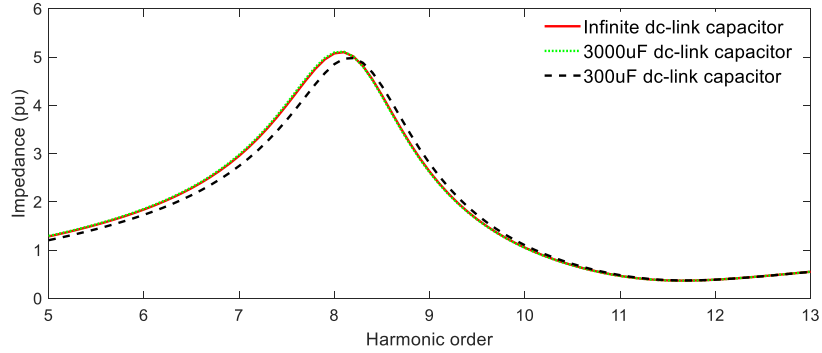
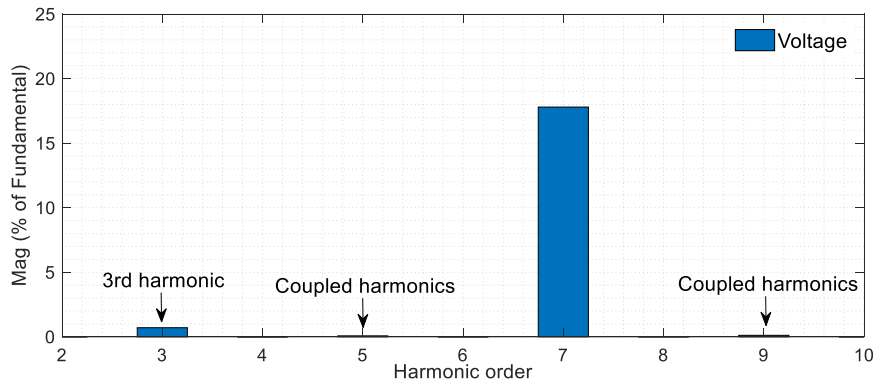


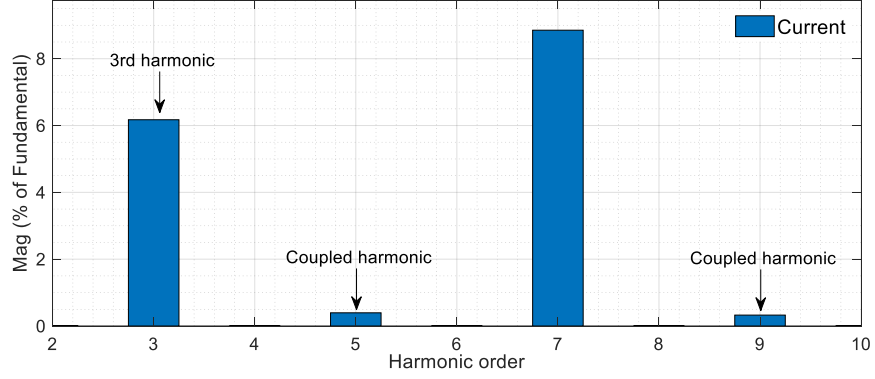
Figure 4-5 Comparison between the calculated impedances for different dc-link capacitors

### C. Strength of the Coupling Effect

The final model has also shown that the dc-link capacitor leads to harmonic coupling effects between different harmonics, but the coupling can be demonstrated to be negligible. Fig. 4-5 shows the simulated voltage and current at the PCC when 20% of the 7<sup>th</sup> harmonic voltage is added to the ac source. The 7<sup>th</sup> harmonic introduces the 5<sup>th</sup> and 9<sup>th</sup> harmonics, which is consistent with the theoretical analysis in Section 4.2. But the coupling-introduced voltage and current are very small, so the coupling can be omitted in practice.



(a) coupled voltage



(b) coupled current

Figure 4-6 Harmonic coupling effect in the VSC

### 4.3.2 Verification of the Thevenin Circuit for the 3<sup>rd</sup> harmonic

The verification of the Thevenin circuit of single-phase PV at the 3<sup>rd</sup> harmonic can be conducted using two sets of simulations, which are shown in Figure 4-7. For Setup1, there is no harmonic source in the ac system, and the relationship between the measured 3<sup>rd</sup> harmonic current at the PCC ( $I_{pcc1}$ ) and the 3<sup>rd</sup> harmonic voltage source of the Thevenin circuit can be written as (4.26). For Setup2, a 3<sup>rd</sup> harmonic voltage source is added to the system source ( $V_s$ ), and the relationship between the measured 3<sup>rd</sup> harmonic current at the PCC ( $I_{pcc2}$ ) and the 3<sup>rd</sup> harmonic voltage source of the Thevenin circuit can be written as (4.27). Therefore, we have two equations and two unknowns ( $V_{gs3}$ , and  $Z_{3,3}$ ). Solving these two equations can give the harmonic voltage source ( $V_{gs3}$ ) and the impedance of the Thevenin circuit ( $Z_{3,3}$ ).

$$I_{pcc1} = \frac{V_{gs3}}{Z_{3,3} + Z_s} \quad (4.26)$$

$$I_{pcc2} = \frac{V_{gs3} - V_s}{Z_{3,3} + Z_s} \quad (4.27)$$

The results were compared with the calculated results using the proposed model in Table II for the VSC with a capacitor of 300uF. The theoretical Thevenin circuit parameters match well with the Thevenin circuit parameters obtained by the time-

domain simulations. Therefore, the Thevenin circuit for the 3<sup>rd</sup> harmonic is correct.

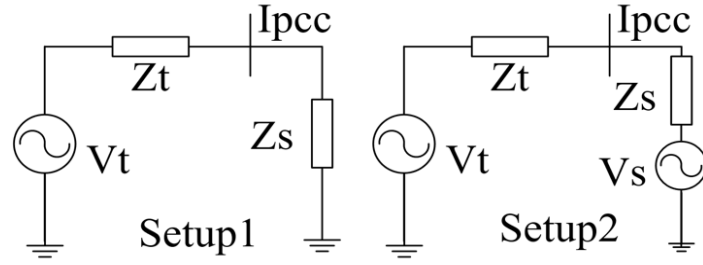
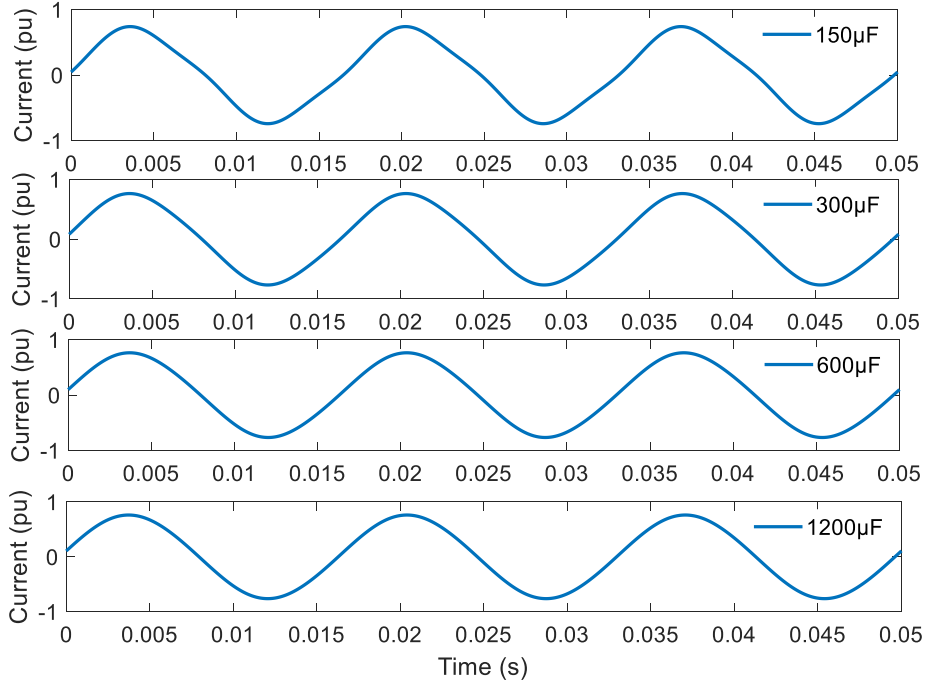


Figure 4-7 Setups for computing the Thevenin circuit

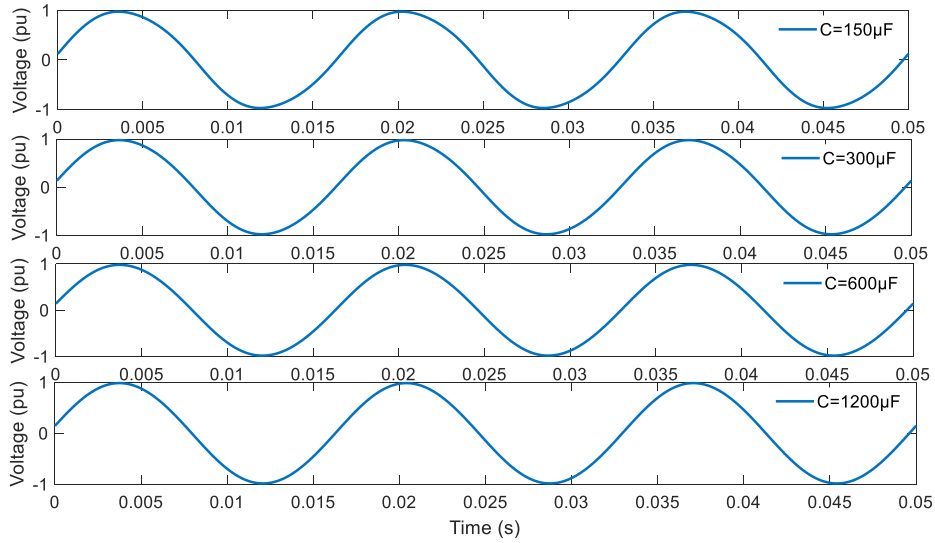
Table 4-2 3<sup>rd</sup> harmonic voltage at the PCC obtained using time-domain simulations and the proposed model

	Simulated results	Calculated results
$V_{gs3}$ (pu)	0.0003 - 0.0212i	0.0027 - 0.0210i
$Z_{3,3}$ (pu)	0.1759 + 0.6150i	0.1789 + 0.6444i

The above analyses show that the single-phase VSC produces the 3<sup>rd</sup> harmonic voltage and current, and the Thevenin model can be used to predict the 3<sup>rd</sup> harmonic distortion caused by the single-phase VSC. It is noteworthy that the source of the 3<sup>rd</sup> harmonic is influenced by the dc-link capacitance. A smaller dc-link capacitance will lead to a larger 3<sup>rd</sup> harmonic voltage source. Figure 4-8 shows the current and voltage waveforms at the PCC with different dc-link capacitances. The IHDs of the 3<sup>rd</sup> harmonic current and voltage are shown in Table 4-3. The 3<sup>rd</sup> harmonic distortion is inversely proportional to the dc-link capacitance, which is consistent with (4.24). Section 4.5 will look at the degree of the impact of the 3<sup>rd</sup> harmonic distortion caused by the single-phase VSC within practical system parameters.



(a) Current waveforms



(b) Voltage waveforms

Figure 4-8 Voltage and current waveforms at the PCC involving different dc-link capacitors

Table 4-3 IHDs of the 3<sup>rd</sup> harmonic voltage and current involving different dc-link capacitors

Capacitor	150μF	300μF	600μF	1200μF
Voltage IHD (%)	3.36%	1.7%	0.86%	0.43%
Current IHD (%)	7.65%	3.8%	1.86%	0.92%

### 4.3.3 Impact of the Outer Control Loop

The impact of the outer control loop of the single-phase VSC was not included in the proposed model, but the calculated harmonic model is still accurate, which means the outer control loop has a negligible impact. As noted from the control diagram of the single-phase VSC in Figure 2-6, the outer control loop regulates the dc-link voltage on the d axis and the reactive power injected to the grid by the VSC on the q axis. Since the reactive power is generally set as 0, the reference current on the q axis is also zero ( $I_{qref}=0$ ). Therefore, only the dc-link voltage control loop affects the harmonic response of the VSC by affecting the reference current of the inner current control loop ( $I_{dref}$ ). According to (4.14), the harmonic components in the dc-link voltage can be expressed as a function of the ac side harmonic current, as shown below:

$$\begin{aligned}
 V_{dc(h-1)} &= \frac{I_{ch}m_1}{2V_{dc0}C_{dc}(\omega_h - \omega_1)} \cos(\omega_h t + \delta_{ch} - \omega_1 t - \alpha_1 - \frac{\pi}{2}) \\
 &+ \frac{m_h I_{c1}}{2V_{dc0}C_{dc}(\omega_h - \omega_1)} \cos(\omega_h t + \alpha_h - \omega_1 t - \delta_{c1} - \frac{\pi}{2}) \\
 &= Z_{ch1}I_{ch} + Z_{gh2}I_{gh}
 \end{aligned} \tag{4.28}$$

$$\begin{aligned}
 V_{dc(h+1)} &= \frac{I_{ch}m_1}{2V_{dc0}C_{dc}(\omega_h + \omega_1)} \cos(\omega_h t + \delta_{ch} + \omega_1 t + \alpha_1 - \frac{\pi}{2}) \\
 &+ \frac{m_h I_{c1}}{2V_{dc0}C_{dc}(\omega_h + \omega_1)} \cos(\omega_h t + \alpha_h + \omega_1 t + \delta_{c1} - \frac{\pi}{2}) \\
 &= Z_{ch2}I_{ch} + Z_{gh2}I_{gh}
 \end{aligned} \tag{4.29}$$

The corresponding reference current (on d axis) for the inner current control loop can be written as

$$I_{dref(h-1)} = -H_1(s)Z_{th}I_{ih} - H_1(s)Z_{gh}I_{gh} \quad (4.30)$$

$$I_{dref(h+1)} = -H_1(s)Z_{th}I_{ih} - H_1(s)Z_{gh}I_{gh} \quad (4.31)$$

It is noted that the impedance  $Z_{ch}$  in (4.30) and  $Z_{ch}$  in (4.31) determine the relationship between the harmonic components in the dc-link voltage and the harmonic components in the ac side current. For the studied system (the dc-link capacitor is set as  $300\mu\text{F}$ ), the results of  $Z_{ch1}$  and  $Z_{gh1}$  ( $Z_{ch2}$  and  $Z_{gh2}$  are even smaller) under different harmonics are illustrated in Figure 4-9.  $Z_{ch1}$  and  $Z_{gh1}$  are very small, which means the harmonic current on the ac side of the VSC leads to only very limited harmonic components in the dc-link voltage. This is because the power loop of the VSC induces the harmonic components in the dc-link voltage, and, as demonstrated previously, the impact of the power loop is not significant. Consequently, the harmonic components in the reference current are negligible.

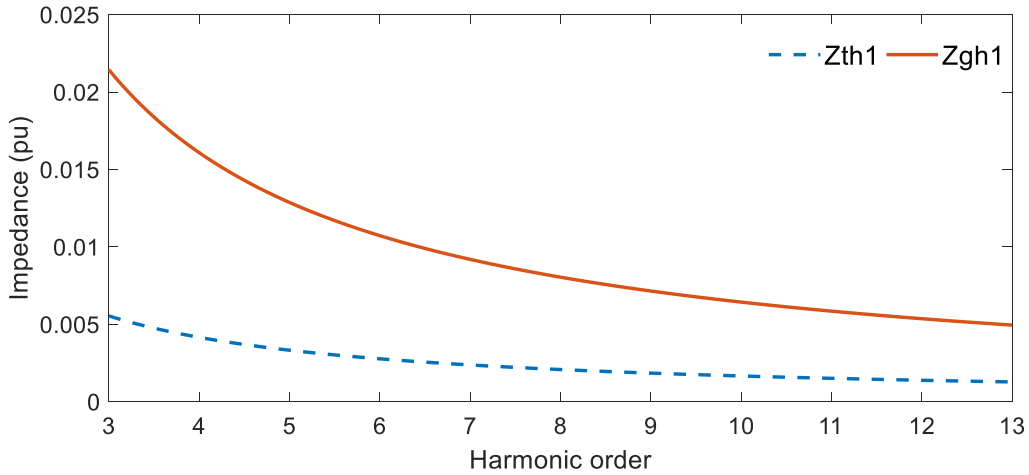


Figure 4-9 Impedance that connects the harmonic voltage on the dc-link and the harmonic current on the ac side of the VSC with the harmonic current at the PCC

To further illustrate the problem, the impact of the outer control loop that regulates the dc-link voltage is compared with the effect of the outer control loop that regulates active (or reactive) power. The harmonic components in the active power can be written as

$$\begin{aligned}
P_{(h-1)} &= \frac{3}{4} V_{g1} I_{gh} \cos(\omega_h t + \delta_{gh} - \omega_1 t - \theta_1 - \frac{\pi}{2}) \\
&+ \frac{3}{4} I_{g1} V_{gh} \cos(\omega_h t + \theta_{gh} - \omega_1 t - \delta_1 - \frac{\pi}{2})
\end{aligned} \tag{4.32}$$

$$\begin{aligned}
P_{(h+1)} &= \frac{3}{4} V_{g1} I_{gh} \cos(\omega_h t + \delta_{gh} + \omega_1 t + \theta_1 - \frac{\pi}{2}) \\
&+ \frac{3}{4} I_{g1} V_{gh} \cos(\omega_h t + \theta_{gh} + \omega_1 t + \delta_1 - \frac{\pi}{2})
\end{aligned} \tag{4.33}$$

The corresponding reference current for the inner current control loop can be written as

$$I_{dref(h-1)} = -H_1(s)P_{(h-1)} \tag{4.34}$$

$$I_{dref(h+1)} = -H_1(s)P_{(h+1)} \tag{4.35}$$

As shown in (4.30) and (4.31), the harmonic components in the reference current are determined by both the harmonic voltage and current at the PCC. Here we compared the harmonic components in the active power that are induced by the ac side harmonic current with the harmonic components in the dc-link voltage that are induced by the ac side harmonic current. In practice, the fundamental frequency voltage at the PCC is regulated to be 1 pu ( $V_{g1}=1$ ), so the harmonic component in the reference current is  $I_{drefh}=-3/4V_{g1}H_1(s)=-0.75H_1(s)I_h$ . Therefore, according to the results in Figure 4-9, for the same ac side harmonic current, the harmonic components in the reference current that are induced by the dc-link voltage control are much less than those caused by the active power control. Chapter 3 showed that the active power outer control loop is not significant for most harmonics, so the dc-link voltage control has an even more negligible impact. In summary, for harmonic modeling, the dc-link voltage control can be omitted with confidence.

#### 4.4 Investigation of 3<sup>rd</sup> Harmonics Produced by VSC in Practical Systems

The concern about the Thevenin circuit developed at the 3<sup>rd</sup> harmonic is how the harmonic source affected the distribution system. The degree of the 3<sup>rd</sup> harmonic distortion caused by the single-phase VSC in practical distribution systems was investigated to determine whether the 3<sup>rd</sup> harmonic source needed to be considered. According to the established equations, the equivalent impedance and the 3<sup>rd</sup> harmonic voltage source of the Thevenin circuit can be computed using (4.19) and (4.24) with a set of parameters. For practical, single-phase PV systems, the range of parameters are listed in Table 4-4. Table 4-5 shows the resulting range of the 3<sup>rd</sup> harmonic voltage source and the equivalent impedance of the Thevenin circuit.

Table 4-4 Parameters of practical single-phase PV systems

$V_{nom}$	120V or 240V	$P_{nom}$	1kW ~ 3kW
$L_2$	2mL ~ 5mL	$L_1$	2mL ~ 5mL
$C_f$	5 $\mu$ F~20 $\mu$ F	$R_{Cf}$	1 $\Omega$ ~ 2 $\Omega$
$m_1$	0.6~1.0	$I_{e1}$	8.33A~50A
$K_p$	0.15	$K_i$	6.6
$V_{dc0}$	120V ~ 400V	$C_{dc}$	1000 $\mu$ F~3000 $\mu$ F

Table 4-5 Range of the voltage source and impedance of the Thevenin circuit

$V_{gs3}$	0.84% ~ 2.64%	$Z_{3,3}$	0.3418 pu ~ 0.6437 pu
-----------	---------------	-----------	-----------------------

Based on the results in Table 4-5, the equivalent circuit in Figure 4-10 can be used to estimate the 3<sup>rd</sup> harmonic voltage and current in the system. Notably, the equivalent impedance of the connected distribution system is also needed to evaluate the 3<sup>rd</sup> harmonic distortion. Table 4-6 shows a survey of the equivalent impedance of the practical, single-phase distribution systems. According to the data in Table 4-5, Table 4-6, and Figure 4-10, the practical 3<sup>rd</sup> harmonic voltage and current can be written as shown in Table 4-7. Although the 3<sup>rd</sup> harmonic voltage source of the Thevenin circuit is not very small, the 3<sup>rd</sup> harmonic voltage and current at the PCC are limited because the equivalent impedance of the Thevenin

circuit is very large. Therefore, practically speaking, the 3<sup>rd</sup> harmonic produced by the single-phase VSC is not a significant concern for the system.

Table 4-6 Single-phase impedance data collected from various sources

Region	Country	R+jX (1 $\phi$ $\Omega$ )	Z(1 $\phi$ $\Omega$ )	Comments
Europe	IEC-TR-60275	0.400+j0.250	0.4717	L-N,230V, recommended value
	Europe (95%)	0.400+j0.270	0.5420	L-N, 230V (IEC-725 survey results)
Asia	Korean (95%)	0.670+j0.370	0.7654	220V 2-wire for 1 $\phi$
	Japan	0.231+j0.089	0.2461	L-N, 100V
		0.257+j0.117	0.2824	L-L, 200V
North America	United states (95%)	0.102+j0.059	0.1178	L-L, 240V
	Hydro Quebec (high-end)	0.190+j0.062	0.1999	L-N, 120V, calculated value
		0.200+j0.080	0.2122	L-L, 120V, calculated value
Collected data (Urban and suburban)	Field measurement (95%)	0.090+j0.055	0.1055	L-N, 120V
	Site calculation		0.0900	L-N, 120V
	Survey (typical)		0.0660	L-N, 120V
	Based on $\Delta V$ limit (high-end)		0.1~0.2	L-N, 120V

Table 4-7 3<sup>rd</sup> harmonic voltage and current at the PCC in practical, single-phase distribution systems

System parameters	3 <sup>rd</sup> harmonic voltage at PCC	3 <sup>rd</sup> harmonic current at PCC
$V_{gs3}$	0.84% ~ 2.64%	
$Z_{3,3}$	0.95 pu ~ 2.52 pu	0.08% ~ 0.1%
$Z_{s3}$	0.01pu ~ 0.1pu	0% ~ 2.51%

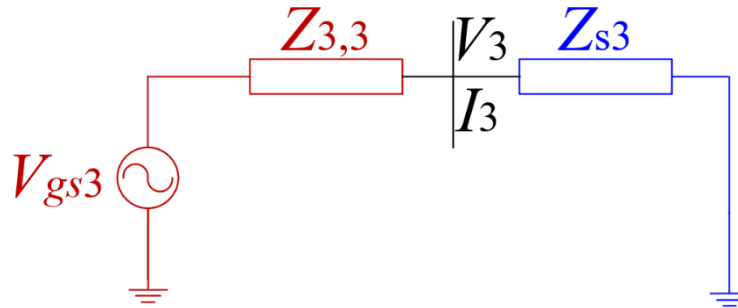


Figure 4-10 Equivalent circuit to compute the 3<sup>rd</sup> harmonic distortion

The 3<sup>rd</sup> harmonic distortion caused by the single-phase VSC was further compared with the 3<sup>rd</sup> harmonic distortions caused by other appliances, such as desktops, laptops, TVs, and washers. These harmonic-producing appliances are harmonic current sources. Therefore, the 3<sup>rd</sup> harmonic current induced by the single-phase PV was compared with the 3<sup>rd</sup> harmonic currents induced by the appliances mentioned above, as shown in Table 4-8. The 3<sup>rd</sup> harmonic produced by the single-phase VSC was much lower than that for the other appliances. Therefore, the 3<sup>rd</sup> harmonic produced by the single-phase VSC can be omitted.

Table 4-8 Comparisons between the 3<sup>rd</sup> harmonic currents produced by single-phase and other appliances

Appliance	Single-phase VSC	Desktop	Laptop	TV	Washer
3 <sup>rd</sup> current IHD	0~2.51%	85.49%	80.4%	3.33%	66.57%

## 4.5 Summary

Based on the above analysis, the main findings and contributions of this chapter can be summarized as follows:

- The response mechanism of the single-phase VSC to power system harmonics was explained, and a harmonic model of the single-phase VSC was established. The results showed that the single-phase VSC can be represented using a Thevenin circuit for the 3<sup>rd</sup> harmonic and an impedance model for other

harmonics. The equations that can compute the developed model were also established.

- Time-domain simulations verified the correctness of the proposed harmonic model for the single-phase VSC. In addition, the impacts of the dc-link capacitor and outer control loop were analyzed.
- The 3<sup>rd</sup> harmonic voltage and current produced by the single-phase VSC in practical systems was investigated. The 3<sup>rd</sup> harmonic voltage source did not impact the connected distribution significantly due to the large equivalent impedance of the Thevenin circuit.

## Chapter 5

# Modeling Doubly-fed Induction Generators for Power System Harmonic Analysis

The doubly-fed induction generator (DFIG) is predominantly used in power systems because it operates at a constant frequency under variable wind speeds, provides independent regulation for active and reactive power, loses power very infrequently, and has low converter costs [79]. A DFIG generally consists of three sections: an induction generator (IG), a rotor side converter (RSC), and a grid side converter (GSC). The harmonic features of the DFIG are determined by these three parts. The harmonic model of an IG has already been maturely developed [80], and the validity of its equivalence in DFIG has also been investigated in [81]. Consequently, the key to developing the harmonic model of DFIG is the harmonic models of the RSC and the GSC as well as their integration with the harmonic model of the IG. Note that the RSC and GSC are back-to-back connected (i.e., they share the dc-link), so the harmonics entering the RSC can propagate into the GSC and vice versa, which leads to mutual harmonic coupling between the RSC and GSC. As a result, the harmonic model of a three-phase VSC developed in Chapter 2 cannot be directly applied to the RSC and GSC. In this chapter, a new harmonic model of the combined RSC and GSC unit will be presented first. Based on the model, a full harmonic model of the DFIG will be presented.

This chapter is organized as follows. Section 5.1 provides a brief review of the harmonic modeling of the DFIG for harmonic analysis. Section 5.2 describes the operating characteristics of the DFIG. Section 5.3 shows the derivations of the harmonic model of the DFIG. Section 5.4 and Section 5.5 present the verifications of the proposed model via time-domain simulations and lab experiments, respectively. The application of the proposed model for power system harmonic

power flow studies is validated in Section 5.6. Section 5.7 contains the chapter summary.

## 5.1 Review of Harmonic Modeling of the DFIG

DFIG models for the purpose of harmonic studies have been investigated and published. For example, some harmonic current source models were proposed for harmonic analysis in DFIG-based wind power systems [82]-[84]. In these papers, the RSC and GSC[82], or the whole DFIG [83][84] were modeled as harmonic current sources that are determined using measurement results. This model was also proposed by IEC 61400-21: 2008 in which the wind turbines were suggested to be represented using harmonic current source models established by measurements [64]. But such a harmonic current source model has been reported to be inaccurate [65]. In a most recent IEC report [65], a Norton equivalent model was suggested to replace the harmonic current source model for better accuracy. Nevertheless, this report did not present the technical justifications for this recommendation, and, as a result, the recommended measurement-based Norton model is not always guaranteed to be accurate.

There are also some analytical harmonic models of DFIG proposed for harmonic studies. Typical examples are the extended harmonic domain model [85][86], the impedance-based model [87]-[91], or the more accurate impedance matrix, which includes the frequency coupling effect [92][94]. Among them, the impedance or the impedance matrix model is favored for harmonic analysis since it can be easily integrated into the existing harmonic power flow tools. In the impedance model of [87]-[91], the RSC and GSC are decoupled from the dc-link capacitor by assuming a constant dc-link voltage, and the RSC and GSC are both modeled as impedances. However, no rigorous analytical justifications have been provided for such an assumption. In practice, the dc-link capacitor may also experience harmonic ripples because of the ac/dc harmonic interaction, especially when the dc-link capacitance is not sufficiently large. Because harmonic ripples in the dc-link voltage that come from the RSC can propagate into the GSC and vice versa, there exists a harmonic

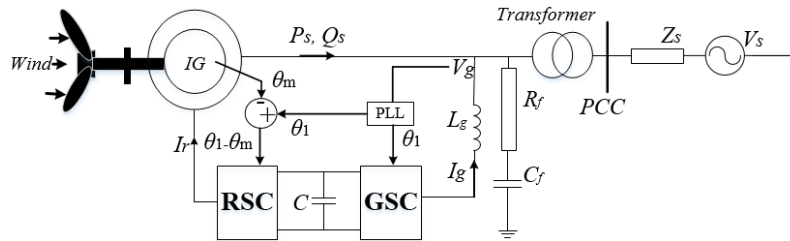
coupling between the RSC and GSC. As a result, the obtained impedance model based on a constant dc-link voltage could be inaccurate. In [95], the impact of the dc-link capacitor is investigated but does not show the mechanism of harmonic penetration between RSC and GSC.

## 5.2 Operating Characteristics of DFIG

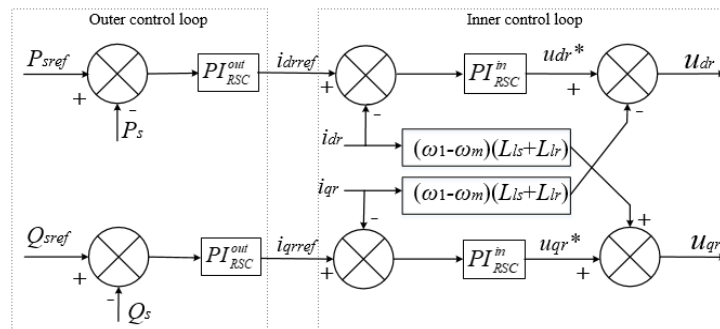
Figure 5-1 (a) shows the typical structure of a DFIG, which contains an IG, a GSC, and an RSC [82]. An inductor ( $L_g$ ) is connected to the GSC to attenuate the switching harmonics. An RC branch on the entrance of the DFIG is used for power factor correction and could also attenuate the switching harmonics. The power generated by the wind turbine flows into the grid mainly through the stator winding. However, when the rotor speed is greater than the synchronous speed, the rotor also delivers power to the grid through the RSC and GSC link. If the rotor speed is lower than the synchronous speed, the grid will transfer power to the rotor through the GSC and RSC link. In this way, the GSC and RSC unit transfers power in both directions [96].

The RSC supplies an adjustable frequency ac voltage ( $\omega_1-\omega_m$ ,  $\omega_1$  is the grid frequency and  $\omega_m$  is the rotor speed) to the rotor of the IG through the RSC controls. Figure 5-1 (b) shows the control scheme. The active power and reactive power from the stator circuit ( $P_s$ ,  $Q_s$  in Figure 5-1 (a)) to the grid are maintained to specific values established through the outer control loop. The constant power control is achieved by controlling the rotor side current ( $I_r$  in Figure 5-1(a)) [97] through varying the rotor voltage imposed by the RSC and its modulation signal, as shown in the inner control loop. The GSC is connected to the grid, so the ac voltage is synchronized with the grid voltage, and its control is shown in Figure 5-1 (c). The GSC maintains the dc-link voltage and the reactive power of the GSC (usually set as 0,  $i_{gqref}=0$ ), which is realized by controlling the current on the ac side of the GSC ( $I_g$  in Figure 5-1(a)). A phase-lock loop (PLL) is used to synchronize with the grid voltage ( $\theta_1$ ) for the GSC control. The angle result can also be used to track the frequency of the RSC's ac voltage ( $\theta_1-\theta_m$ ).

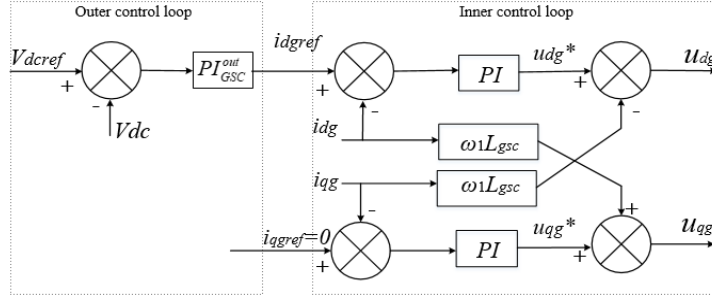
Figure 5-2 shows the RSC and GSC's responses to external low-order harmonics. When there is a harmonic in the grid ( $\omega_h$ ), both the RSC and GSC are exposed to that harmonic ( $\omega_h$  for GSC and  $\omega_h \pm \omega_m$  for RSC). Since the control loop takes the converter ac-side current ( $i_r$  and  $i_g$ , where subscript r and g stand for RSC and GSC) as the input, the harmonics are present in the control loop and thus affect the modulation signal ( $m$ ) and the resulting switching function. The harmonics on the ac side of the RSC and GSC can also propagate into the dc-link through power electronic switching, leading to harmonic ripples in the dc-link voltage. This dc-link voltage, in turn, can affect the harmonic voltage on the ac side of the RSC and GSC. Note that the ripples in the dc-link voltage are jointly determined by the RSC and GSC, there will be a harmonic coupling between the RSC and GSC. To ensure a harmonic model, the RSC and GSC unit needs to be developed by analyzing both the control loop and the ac/dc harmonic interaction.



(a) Typical DFIG system



(b) Control block of the RSC



(c) Control block of the GSC

Figure 5-1 Typical DFIG system and the control diagrams of the RSC and GSC

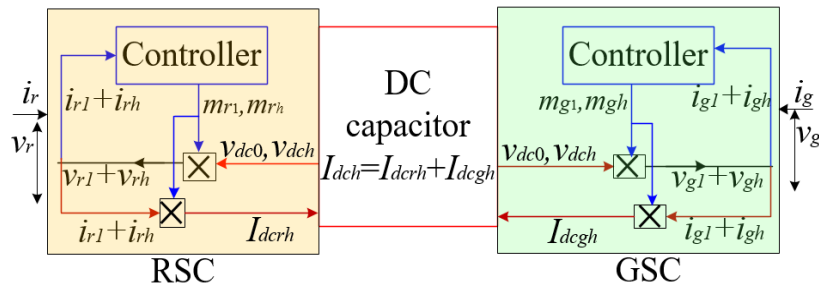


Figure 5-2 RSC and GSC response mechanism to the external harmonics

### 5.3 Harmonic Model of the DFIG

The main challenge to developing a harmonic model for the DFIG is to find a method to model the combined RSC and GSC unit, a two-terminal “equipment”, as shown in Figure 5-3. A model of this unit represents the harmonic voltage and current relationships between the two terminals, “r” and “g,” i.e.,

$$(v_{rh}, i_{rh}) = f(v_{gh}, i_{gh}) \quad (5.1)$$

Once the above model is made available, it can be connected to the linear model of the induction generator, which is shown in Figure 5-4 (the detailed derivation of this equivalent circuit will be presented in Section 5.3.1). Then a harmonic model for the entire DFIG equipment can be developed.

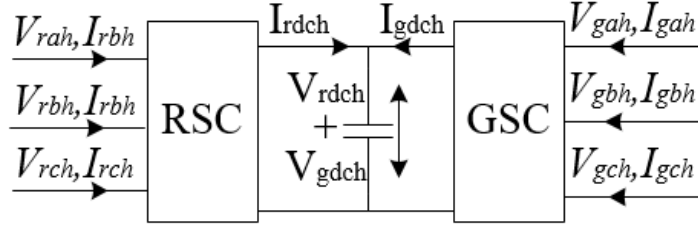


Figure 5-3 Combined RSC and GSC unit to be modeled.

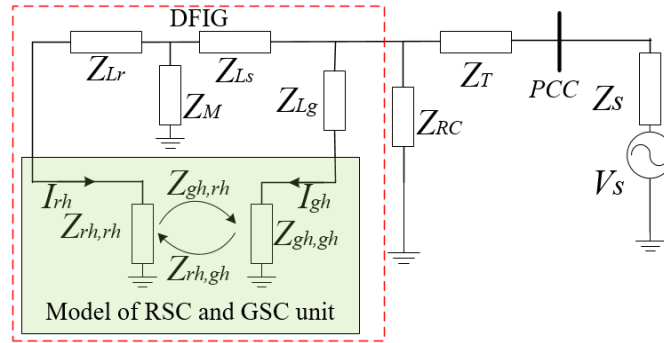


Figure 5-4 Equivalent harmonic model of the DFIG system

### 5.3.1 Harmonic Coupling Model of RSC and GSC

The harmonic model of the combined RSC and GSC unit can be developed using the flow in Figure 5-5. The detailed procedure to get the harmonic model is summarized as follow:

- Assume that the steady-state currents entering the ac sides of the RSC ( $v_{rh}$ ,  $i_{rh}$ ) and GSC ( $v_{gh}$ ,  $i_{gh}$ ) contain harmonics.
- Through the control loop, the modulation signal for RSC and GSC can be expressed analytically ( $m_{rh}$ ,  $m_{gh}$ ).
- The steady-state current ( $i_r$ ,  $i_g$ ), through the PWM switching via the modulation signal  $m$ , results in the dc-side current. The dc-link voltage can be determined by integrating the dc currents from both the RSC and GSC, thus establishing a relationship between the dc-link voltage and the input currents of the RSC and GSC.
- On the other hand, the dc-link voltage is related to the ac voltages of the RSC and GSC through the PWM switching. Thus, another equation can be



$$[I]_{dq} = T[I]_{abc} \quad (5.3)$$

where

$$T = \begin{bmatrix} \cos(\omega_{g1}t + \theta_{g1}) & \cos(\omega_{g1}t + \theta_{g1} - 120^\circ) & \cos(\omega_{g1}t + \theta_{g1} + 120^\circ) \\ -\sin(\omega_{g1}t + \theta_{g1}) & -\sin(\omega_{g1}t + \theta_{g1} - 120^\circ) & -\sin(\omega_{g1}t + \theta_{g1} + 120^\circ) \end{bmatrix} \quad (5.4)$$

and  $\theta_{g1}$  is the synchronized angle for the  $abc/dq$  conversion. The transformation in (5.4) is obtained with the phase-lock loop (PLL). Substituting (5.2) to (5.3) leads to

$$i_{gd} = I_{g1} \cos(\delta_{g1} - \theta_{g1}) + \sum I_{gh+} \cos(\omega_{gh+}t + \delta_{gh+} - \omega_{g1}t - \theta_{g1}) + \sum I_{gh-} \cos(\omega_{gh-}t + \delta_{gh-} + \omega_{g1}t + \theta_{g1}) \quad (5.5)$$

$$i_{gq} = I_{g1} \sin(\delta_{g1} - \theta_{g1}) + \sum I_{gh+} \sin(\omega_{gh+}t + \delta_{gh+} - \omega_{g1}t - \theta_{g1}) - \sum I_{gh-} \sin(\omega_{gh-}t + \delta_{gh-} + \omega_{g1}t + \theta_{g1}) \quad (5.6)$$

Since we focused on the steady-state, low-order harmonics, the outer control loop and PLL of the GSC were omitted because of their low bandwidths (e.g., lower than 120Hz). Therefore, only the inner control loop was considered here. As a result, the above current passing through the inner current control gives the output signal as

$$\begin{aligned} u_{gd} &= H_d(s)(H_{g2}(s)[I_{gdref} - i_{gd}] - \omega_{g1}L_g i_{gq}) \\ u_{gq} &= H_d(s)(H_{g2}(s)[I_{gqref} - i_{gq}] + \omega_{g1}L_g i_{gd}) \end{aligned} \quad (5.7)$$

where  $H_d(s)$  represents the 1.5-sample delay introduced by the digital implementation of the control and PWM modulation and  $H_{g2}$  is the inner PI regulator of GSC. The expression in (5.7) gives the harmonic components in the above voltage signal as

$$\begin{aligned} u_{gd\_harmonic} &= -H_d(s)H_{g2}(s)i_{gd\_harmonic} - \omega_{g1}L_{gsc}i_{gq\_harmonic} \\ u_{gq\_harmonic} &= -H_d(s)H_{g2}(s)i_{gq\_harmonic} + \omega_{g1}L_{gsc}i_{gd\_harmonic} \end{aligned} \quad (5.8)$$

Converting the  $dq$  voltage in (5.8) back to the  $abc$  frame (for PWM) gives

$$\begin{aligned}
u_{ga\_harmonic} = & H_d(s - j\omega_{g1}) \left\{ -H_{g2}(s - j\omega_{g1})i_{ph+} - j\omega_{g1}L_{gsc}i_{gh+} \right\} \\
& + H_d(s + j\omega_{g1}) \left\{ -H_{g2}(s + j\omega_{g1})i_{gh-} + j\omega_{g1}L_{gsc}i_{gh+} \right\}
\end{aligned} \quad (5.9)$$

and phase-B and phase-C modulation signals have a 120-degree shift from (5.9). The result in (5.9) is scaled to the modulation signal as

$$m_{gah} = (\sqrt{2/3}V_{nom} / V_{dc0})u_{ga\_harmonic} \quad (5.10)$$

where  $V_{nom}$  is the nominal line voltage and  $V_{dc0}$  is the desired dc voltage. As shown in (5.10), in addition to the fundamental frequency component, there are harmonic components in the modulation signal. To illustrate the ac/dc harmonic interaction, the phase-A modulation signal can be written as

$$\begin{aligned}
m_{ga\_harmonic} = & m_{g1} \cos(\omega_{g1}t + \phi_{g1}) \\
& + \sum m_{gh+} \cos(\omega_{gh+}t + \phi_{gh+}) + \sum m_{gh-} \cos(\omega_{gh-}t + \phi_{gh-})
\end{aligned} \quad (5.11)$$

where  $\phi$  is the angle of the modulation signal. The ac-side harmonics would propagate into the dc side of the converter and induce harmonic ripples on the dc side.

## B. Current and Voltage on the DC side

According to the above current and modulation signal (the switching harmonics are omitted since we focused on the low-order harmonics), the current on the dc side of the GSC can be written as (5.12).

$$\begin{aligned}
i_{gdc} = & i_{ga}m_{ga} + i_{gb}m_{gb} + i_{gc}m_{gc} = \frac{3}{2}m_{g1}I_{g1} \cos(\phi_{g1} - \delta_{g1}) \\
& + \frac{3}{2}I_{g1} \left\{ \sum m_{gh+} \cos(\omega_{gh+}t - \omega_{g1}t + \phi_{gh+} - \delta_{g1}) + \sum m_{gh-} \cos(\omega_{gh-}t + \omega_{g1}t + \phi_{gh-} + \delta_{g1}) \right\} \\
& + \frac{3}{2} \sum m_{g1}I_{gh+} \cos(\omega_{gh+}t + \delta_{gh+} - \omega_{g1}t - \phi_{g1}) + \frac{3}{2} \sum_{i,j \in h+} m_{gi}I_{gj} \cos(\omega_{gi}t - \omega_{gj}t + \phi_{gi} - \delta_{gj}) \\
& + \frac{3}{2} \sum_{i \in h-, j \in h+} m_{gi}I_{gj} \cos(\omega_{gi}t + \omega_{gj}t + \phi_{gi} + \delta_{gj}) + \frac{3}{2} \sum m_{g1}I_{gh-} \cos(\omega_{gh-}t + \delta_{gh-} + \omega_{g1}t + \phi_{g1}) \\
& + \frac{3}{2} \sum_{i \in h+, j \in h-} m_{gi}I_{gj} \cos(\omega_{gi}t + \phi_{gi} + \omega_{gj}t + \delta_{gj}) + \frac{3}{2} \sum_{i \in h-, j \in h-} m_{gi}I_{gj} \cos(\omega_{gi}t + \phi_{gi} - \omega_{gj}t - \delta_{gj})
\end{aligned} \quad (5.12)$$

In (5.12), the terms introduced by the interaction between two harmonics can be omitted due to their small magnitudes. Similarly, the harmonic current on the dc side introduced by the RSC can be written as

$$\begin{aligned}
i_{rdc} &= i_{ra}m_{ra} + i_{rb}m_{rb} + i_{rc}m_{rc} = \frac{3}{2}m_{r1}I_{r1} \cos(\phi_{r1} - \delta_{r1}) \\
&+ \frac{3}{2}I_{r1} \left\{ \sum m_{rh+} \cos(\omega_{rh+}t - \omega_{r1}t + \phi_{rh+} - \delta_{r1}) + \sum m_{rh-} \cos(\omega_{rh-}t + \omega_{r1}t + \phi_{rh-} + \delta_{r1}) \right\} \\
&+ \frac{3}{2} \sum m_{r1}I_{rh+} \cos(\omega_{rh+}t + \delta_{rh+} - \omega_{r1}t - \phi_{r1}) + \frac{3}{2} \sum_{i,j \in h+} m_{ri}I_{rj} \cos(\omega_{ri}t - \omega_{rj}t + \phi_{ri} - \delta_{rj}) \\
&+ \frac{3}{2} \sum_{i \in h-, j \in h+} m_{ri}I_{rj} \cos(\omega_{ri}t + \omega_{rj}t + \phi_{ri} + \delta_{rj}) + \frac{3}{2} \sum m_{r1}I_{rh-} \cos(\omega_{rh-}t + \delta_{rh-} + \omega_{r1}t + \phi_{r1}) \\
&+ \frac{3}{2} \sum_{i \in h+, j \in h-} m_{ri}I_{rj} \cos(\omega_{ri}t + \phi_{ri} + \omega_{rj}t + \delta_{rj}) + \frac{3}{2} \sum_{i \in h-, j \in h-} m_{ri}I_{rj} \cos(\omega_{ri}t + \phi_{ri} - \omega_{rj}t - \delta_{rj})
\end{aligned} \tag{5.13}$$

In (5.12) and (5.13), the harmonic components in the current will both pass through the dc-link capacitor, leading to the harmonic components in the dc-link voltage, as shown in Figure 5-3. As a response to the external harmonic  $\omega_{gh}$ , the harmonic on the ac side of the RSC is  $\omega_{rh\pm} = \omega_{gh\pm} \mp \omega_m$ . Consequently, the harmonics penetrating the dc side from the RSC become  $\omega_{rh\pm} \mp \omega_{r1}$ , which is equal to  $\omega_{gh\pm} \mp \omega_{g1}$ . As a result, the harmonics on the dc-link from both the RSC and GSC overlap with each other. Accordingly, the harmonic components in the dc-link voltage can be computed using (5.14), and the ac side voltage of the GSC can be computed using (5.15).

$$V_{dc}(t) = V_{dc0} + \frac{1}{C_{dc}} \int i_{rdch} dt + \frac{1}{C_{dc}} \int i_{gdch} dt \tag{5.14}$$

$$V_{gah} = \left\{ m_{ga}(t) \left( V_{dc0} + \frac{1}{C_{dc}} \int i_{rdch} dt + \frac{1}{C_{dc}} \int i_{gdch} dt \right) \right\}_h \tag{5.15}$$

### C. Harmonic Model for the Combined RSC and GSC Unit

Substituting (5.12) and (5.13) for (5.15) can lead to the harmonic model of the

combined RSC and GSC unit. Overall, the relationship between the harmonic voltage and current of the RSC and GSC can be expressed as (5.16). The equivalent circuit is shown in Figure 5-4.

$$\begin{bmatrix} V_{GSCh} \\ V_{RSC h} \end{bmatrix} = \begin{bmatrix} Z_{gh,gh} & Z_{gh,rh} \\ Z_{rh,gh} & Z_{rh,rh} \end{bmatrix} \begin{bmatrix} I_{GSC h} \\ I_{RSC h} \end{bmatrix} \quad (5.16)$$

The impedance matrix can be written as (5.17)

$$\begin{bmatrix} \dot{V}_{ga3\pm} \\ \dot{V}_{ga5\pm} \\ \dot{V}_{ga7\pm} \\ \dots \\ \dot{V}_{gah\pm} \end{bmatrix} = \begin{bmatrix} Z_{g3,g3}^{\pm} & Z_{g3,g5}^{\pm} & 0 & \dots & 0 \\ Z_{g3,g5}^{\pm} & Z_{g5,g5}^{\pm} & Z_{g5,g7}^{\pm} & \dots & 0 \\ 0 & Z_{g5,g7}^{\pm} & Z_{g7,g7}^{\pm} & \dots & 0 \\ \dots & \dots & \dots & \dots & \dots \\ 0 & 0 & 0 & \dots & Z_{gh,gh}^{\pm} \end{bmatrix} \begin{bmatrix} \dot{I}_{ga3\pm} \\ \dot{I}_{ga5\pm} \\ \dot{I}_{ga7\pm} \\ \dots \\ \dot{I}_{gah\pm} \end{bmatrix} \quad (5.17)$$

$$+ \begin{bmatrix} Z_{g3,r3}^{\pm} & Z_{g3,r5}^{\pm} & 0 & \dots & 0 \\ Z_{g3,g5}^{\pm} & Z_{g5,r5}^{\pm} & Z_{g5,r7}^{\pm} & \dots & 0 \\ 0 & Z_{g5,g7}^{\pm} & Z_{g7,r7}^{\pm} & \dots & 0 \\ \dots & \dots & \dots & \dots & \dots \\ 0 & 0 & 0 & \dots & Z_{gh,rh}^{\pm} \end{bmatrix} \begin{bmatrix} \dot{I}_{ra3\pm} \\ \dot{I}_{ra5\pm} \\ \dot{I}_{ra7\pm} \\ \dots \\ \dot{I}_{rah\pm} \end{bmatrix}$$

where

$$Z_{gh,gh}^{\pm} = \frac{-j3P_{nom} m_{g1}^2}{4V_{nom}^2 C_{dc} (\omega_{gh\pm} \mp \omega_{g1})} + \left\{ \frac{H_d(s \mp j\omega_{g1}) H_{g2}(s \mp j\omega_{g1})}{\mp jL_{gsc} \omega_{g1}} \right\} \left\{ 1 + \frac{\sqrt{3}P_{nom} m_{g1} I_{g1} e^{j(\delta_{g1} \mp \phi_{g1} - \frac{\pi}{2})}}{2\sqrt{2}V_{nom} V_{dc0} C_{dc} (\omega_{gh\pm} \mp \omega_{g1})} \right\} \quad (5.18)$$

$$Z_{gh,gh\pm 2}^{\pm} = \frac{3P_{nom} m_{g1}^2 e^{j(\mp 2\phi_{g1} - \frac{\pi}{2})}}{4V_{nom}^2 C_{dc} (\omega_{gh\pm} \mp \omega_{g1})} + \frac{\sqrt{3}P_{nom} m_{g1} I_{g1} e^{j(\mp \phi_{g1} - \delta_{g1} - \frac{\pi}{2})}}{2\sqrt{2}V_{nom} V_{dc0} C_{dc} (\omega_{gh\pm} \mp \omega_{g1})} \left\{ \frac{H_d(s \mp j\omega_{g1}) H_{g2}(s \mp j\omega_{g1})}{\mp jL_g \omega_{g1}} \right\} \quad (5.19)$$

$$Z_{gh,rh}^{\pm} = \frac{3P_{nom} m_{r1} m_{g1} e^{j(\pm\phi_{g1} - \phi_{r1} - \frac{\pi}{2})}}{4C_{dc} V_{nom}^2 (\omega_{gh\pm} \mp \omega_{g1})} + \left\{ \frac{H_d(s \mp j\omega_{r1}) H_{r2}(s \mp j\omega_{r1})}{\mp j(L_{lr} + L_{ls})\omega_{r1}} \right\} \left\{ \frac{\sqrt{3}P_{nom} m_{g1} I_{r1} e^{j(\delta_{g1} \mp \phi_{g1} - \frac{\pi}{2})}}{2\sqrt{2}V_{nom} V_{dc0} C_{dc} (\omega_{gh\pm} \mp \omega_{g1})} \right\} \quad (5.20)$$

$$Z_{gh,rh\pm 2}^{\pm} = \frac{3P_{nom} m_{g1}^2 e^{j(\mp\phi_{g1} \mp \phi_{r1} - \frac{\pi}{2})}}{4V_{nom}^2 C_{dc} (\omega_{gh\pm} \mp \omega_{g1})} + \frac{\sqrt{3}P_{nom} m_{g1} I_{r1} e^{j(\mp\phi_{g1} + \delta_{r1} - \frac{\pi}{2})}}{2\sqrt{2}V_{nom} V_{dc0} C_{dc} (\omega_{gh\pm} \mp \omega_{g1})} \left\{ \frac{H_d(s \mp j\omega_{g1}) H_{g2}(s \mp j\omega_{g1})}{\mp j(L_{lr} + L_{ls})\omega_{g1}} \right\} \quad (5.21)$$

A similar impedance matrix for the RSC can be established in the same manner as (5.17), and the impedances can be written as

$$Z_{rh,rh}^{\pm} = \frac{-j3P_{nom} m_{r1}^2}{4V_{nom}^2 C_{dc} (\omega_{gh\pm} \mp \omega_{g1})} + \left\{ \frac{H_d(s \mp j\omega_{r1}) H_{r2}(s \mp j\omega_{r1})}{\mp j(L_{ls} + L_{lr})\omega_{g1}} \right\} \left\{ 1 + \frac{\sqrt{3}P_{nom} m_{r1} I_{r1} e^{\delta_{r1} \mp \phi_{r1} - \frac{\pi}{2}}}{2\sqrt{2}V_{nom} V_{dc0} C_{dc} (\omega_{gh\pm} \mp \omega_{g1})} \right\} \quad (5.22)$$

$$Z_{rh,rh\pm 2}^{\pm} = \frac{3P_{nom} m_{r1}^2 e^{j(\mp 2\phi_{r1} - \frac{\pi}{2})}}{4V_{nom}^2 C_{dc} (\omega_{gh\pm} \mp \omega_{g1})} + \frac{\sqrt{3}P_{nom} m_{r1} I_{r1} e^{j(\mp\phi_{r1} - \delta_{r1} - \frac{\pi}{2})}}{2\sqrt{2}V_{nom} V_{dc0} C_{dc} (\omega_{gh\pm} \mp \omega_{g1})} \left\{ \frac{H_d(s \mp j\omega_{r1}) H_{r2}(s \mp j\omega_{r1})}{\mp j(L_{ls} + L_{lr})\omega_{r1}} \right\} \quad (5.23)$$

$$Z_{rh,gh}^{\pm} = \frac{3P_{nom} m_{g1} m_{r1} e^{j(\phi_{r1} \mp \phi_{g1} - \frac{\pi}{2})}}{4C_{dc} V_{nom}^2 (\omega_{gh\pm} \mp \omega_{g1})} + \left\{ \frac{H_d(s \mp j\omega_{g1}) H_{g2}(s \mp j\omega_{g1})}{\mp jL_{gsc}\omega_{g1}} \right\} \left\{ \frac{\sqrt{3}P_{nom} m_{r1} I_{g1} e^{j(\delta_{r1} \mp \phi_{r1} - \frac{\pi}{2})}}{2\sqrt{2}V_{nom} V_{dc0} C_{dc} (\omega_{gh\pm} \mp \omega_{g1})} \right\} \quad (5.24)$$

$$Z_{rh,gh\pm 2}^{\pm} = \frac{3P_{nom} m_{g1} m_{r1} e^{j(\mp\phi_{r1} \mp \phi_{g1} - \frac{\pi}{2})}}{4V_{nom}^2 C_{dc} (\omega_{gh\pm} \mp \omega_{g1})} + \frac{\sqrt{3}P_{nom} m_{r1} I_{g1} e^{j(\mp\phi_{r1} + \delta_{g1} - \frac{\pi}{2})}}{2\sqrt{2}V_{nom} V_{dc0} C_{dc} (\omega_{gh\pm} \mp \omega_{g1})} \left\{ \frac{H_d(s \mp j\omega_{r1}) H_{r2}(s \mp j\omega_{r1})}{\mp jL_{gsc}\omega_{r1}} \right\} \quad (5.25)$$

The model developed above shows that a coupled impedance matrix can represent the combined RSC and GSC unit. The coupling effect includes the coupling between the RSC and GSC and the coupling between different harmonics. The dc-link capacitor introduces both. The above-developed harmonic model of the

combined RSC and GSC unit is a generalized harmonic model for any back-to-back VSCs. This harmonic model can also be applied for other equipment containing back-to-back VSCs.

### 5.3.2 Equivalent Harmonic Model of the DFIG

The developed equations in (5.16) define the relationship between the harmonic voltage and current on the ac side of the GSC and RSC. The above model can be integrated with the impedance model of the induction generator to form the harmonic model of the DFIG. The coupling between different harmonics is very limited (will show in Section 5.4.4), so here we focus on the harmonic impedance correlating the voltage and current of the same harmonic. According to the developed harmonic model in (5.16), the DFIG can be modeled as Figure 5-4, and the model of the RSC and GSC unit in Figure 5-4 can be further equivalently represented as a harmonic impedance using the conducting circuit analysis as shown in Figure 5-6, which can result in the following equations

$$\begin{aligned}
 V_h &= I_{1h} Z_{Ls} + (I_{1h} - I_{rh}) Z_M = I_{gh} (Z_{Lgsc} + Z_{gh,gh}) + I_{rh} Z_{gh,rh} \\
 (I_{1h} - I_{rh}) Z_M &= I_{rh} (Z_{Lr} + Z_{rh,rh}) + I_{gh} Z_{rh,gh} \\
 I_h &= I_{1h} + I_{gh}
 \end{aligned} \tag{5.26}$$

Solving (5.26) gives the equivalent impedance of the DFIG. The expression of the impedance is shown in (5.27).

$$\begin{aligned}
 Z_h &= \frac{V_h}{I_h} = \\
 &= \frac{[Z_M (Z_M + Z_{gh,rh}) - (Z_M + Z_{Lr} + Z_{rh,rh} / slip)(Z_{Ls} + Z_M)](Z_{Lgsc} + Z_{gh,gh})}{(Z_M + Z_{rh,gh} / slip)(Z_M + Z_{gh,rh}) - (Z_M + Z_{Lr} + Z_{rh,rh} / slip)(Z_{Lgsc} + Z_{gh,gh} + Z_{Ls} + Z_M)} \\
 &+ \frac{[Z_{rh,gh} (Z_M + Z_{Ls}) / slip - Z_M (Z_{Lgsc} + Z_{gh,gh})] Z_{gh,rh}}{(Z_M + Z_{rh,gh} / slip)(Z_M + Z_{gh,rh}) - (Z_M + Z_{Lr} + Z_{rh,rh} / slip)(Z_{Lgsc} + Z_{gh,gh} + Z_{Ls} + Z_M)}
 \end{aligned} \tag{5.27}$$

In (5.27), the rotor-side quantities are converted to the stator side.  $Z_{Lg}$  is the impedance of the inductor connected to the GSC.  $Z_{Lr} = jhX_{lr}' + R_r' / slip$  and  $R_r'$  and

$X_{lr}'$  are the rotor resistance and inductance that refer to the stator side, respectively.  $Z_{Ls}=R_s+jhX_{Ls}$  and  $R_s$  and  $X_{Ls}$  are the resistance and reactance of the stator side, respectively.  $Z_M=jhX_M$ ,  $X_M$  is the magnetizing reactance. The slip is defined as

$$slip = \frac{\omega_{h\pm} \mp \omega_m}{\omega_{h\pm}} \quad (5.28)$$

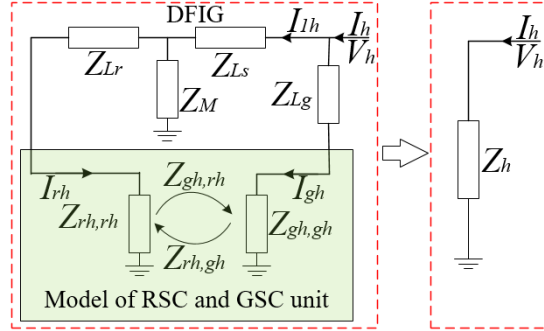


Figure 5-6 Equivalent impedance of the whole DFIG

Generally, the harmonic model of the DFIG includes the front-end RC filter as well, so ultimately the harmonic impedance of the DFIG can be written as

$$Z_{DFIG} = \frac{Z_h Z_{RC}}{Z_h + Z_{RC}} \quad (5.29)$$

The final model in (5.29) reveals that the DFIG can be simply represented using an impedance, and the impedance can be calculated using (5.27) and (5.29).

## 5.4 Verification of the Proposed Model Via Time-domain Simulations

In this section, the proposed model is validated via time-domain simulations. The impact of the dc-link capacitor, the significance of the GSC and RSC impedance, and the coupling impedance between different harmonics in GSC are also analyzed.

### 5.4.1 Validation of the Proposed Model

The proposed impedance model was tested via time-domain simulations in the system of Figure 5-1 in MATLAB/Simulink. The parameters of the studied system are shown in Table 5-1. In power systems, odd harmonics are a significant concern. Thus, only these kinds of harmonics were investigated, and a set of positive-sequence and negative-sequence odd harmonics up to the 29<sup>th</sup> order were added in the ac source to conduct the simulations. The voltage and current at the point of common coupling (PCC) were measured, and a fast Fourier transform (FFT) was conducted to obtain the harmonic voltage and current ( $V_h$  and  $I_h$  at the PCC), which were used to compute the impedance ( $V_h/I_h$ ). The impedances based on simulations were compared to the calculated impedance in (5.29), which is shown in Figure 5-7. It is clear from Figure 5-7 that both the positive-sequence and negative-sequence harmonic impedances calculated using the proposed model have good agreement with the impedances obtained through time-domain simulations, which verifies the correctness of the proposed harmonic impedance model. In the calculation, the coupling between GSC and RSC is omitted, and the calculated results still match well with the simulation results, which verifies the analysis in Section III. In the simulations, IHDs for different harmonics in the ac source were increased up to 20%, and the same result was obtained, which means the model is linear.

Table 5-1 Parameters of studied DFIG system

$V_s$ (kV)	35	$R_{ls}$ (p.u.)	0.023	$H_{RSC\_outer}$	$K_i=0.2, K_p=5$
$Z_s$ ( $\Omega$ )	0.3+j2	$X_{ls}$ (p.u.)	0.18	$H_{RSC\_inner}$	$K_i=0.6, K_p=8$
$R_f$ ( $\Omega$ )	0.0159	$R_r'$ (p.u.)	0.016	$H_{GSC\_outer}$	$K_i=0.1, K_p=5$
$C_f$ ( $\mu F$ )	330	$X_{lr}'$ (p.u.)	0.16	$H_{GSC\_inner}$	$K_i=0.83, K_p=5$
$L_g$ (mH)	0.04	$X_M$ (p.u.)	2.9	$C_{dc}$	5000 $\mu F$
Wind(m/s)	12	$\omega_m$ (p.u.)	1.11	$V_{dc0}$	1150
$P_{nom}$ (MW)	10	$V_{nom}$ (V)	575	rotor/stator	1:1

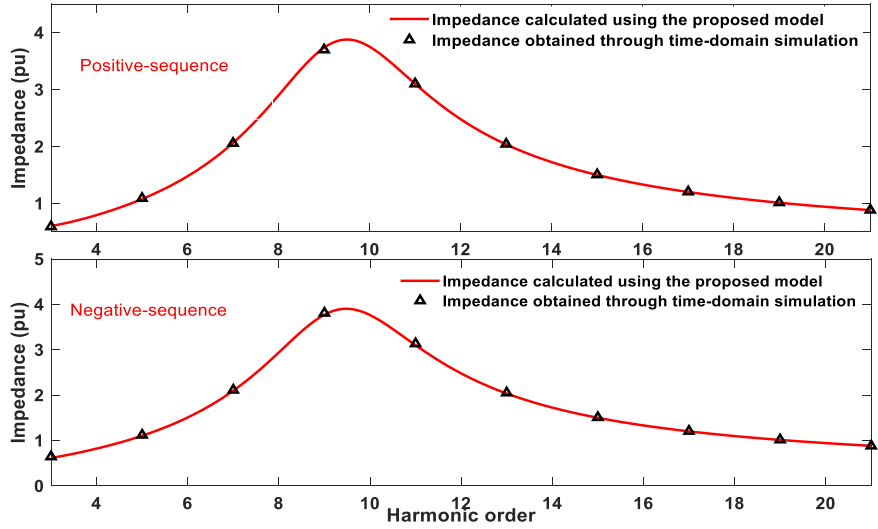
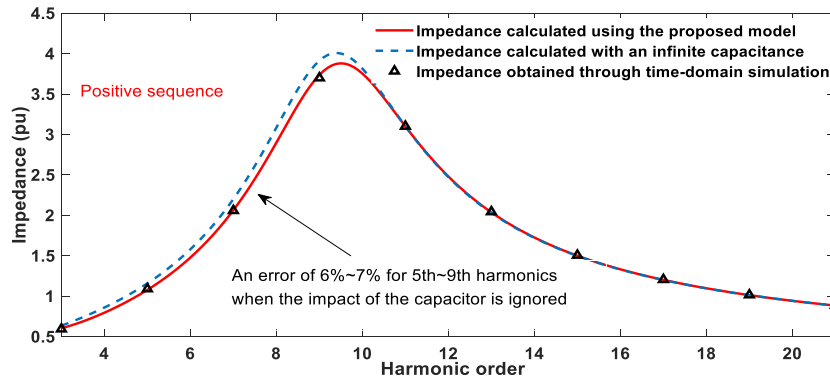


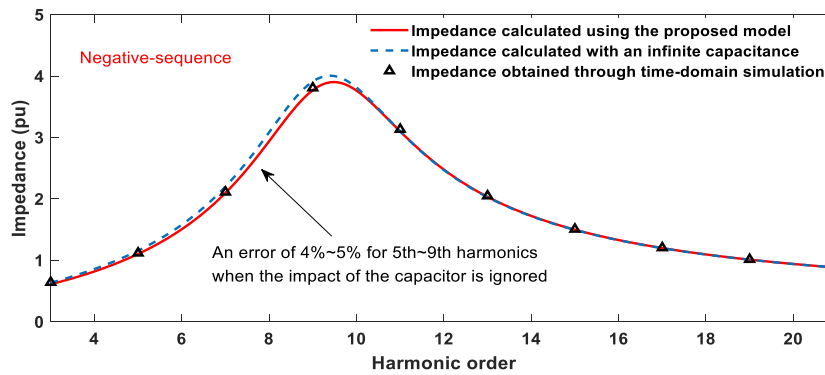
Figure 5-7 Comparison between the impedances calculated using the proposed model and impedances using time-domain simulations

#### 5.4.2 Verification of the Impact of the Dc-link Capacitance

The dc-link capacitor has been shown to affect the impedance of the DFIG by changing the impedance of the GSC and RSC as well as inducing a coupling between the GSC and RSC. In Figure 5-8, the calculated harmonic impedance of the DFIG, which assumed an infinite dc-link capacitance (i.e., the impact of the dc-link capacitor is omitted), was compared to the originally calculated impedance and simulation results. The calculated impedances with an infinite dc-link capacitance deviated from the simulation results with errors of 6%~7% for the positive-sequence impedances and 4%~5% for the negative-sequence impedances under 5<sup>th</sup>~9<sup>th</sup> harmonics, respectively. For the harmonics higher than the 11<sup>th</sup>, the impact of the dc-link capacitance was very limited.



(a) Positive-sequence harmonic impedance of the DFIG



(b) Negative-sequence harmonic impedance of the DFIG

Figure 5-8 Comparison between the impedances calculated using the proposed model and the impedances calculated with an infinite dc-link capacitance

To show whether the dc-link capacitor has a more noticeable impact on the coupling between the GSC and RSC or the impedance of the GSC and RSC, further investigations were conducted. In Table 5-2, the simulated impedance of the GSC and RSC for 3<sup>rd</sup>~7<sup>th</sup> harmonics were compared with the calculated impedance ( $Z_{gh,gh}$  and  $Z_{rh,rh}$ ). In the simulation, the harmonic voltage and current at the ac side of the GSC/RSC were used to obtain the harmonic impedance ( $V_h/I_h$ ). It can be seen that the coupling impedance has limited impacts since the calculated impedances of the GSC and RSC without the coupling impedance did not deviate significantly from the simulated impedances. This is especially true for higher harmonics since a larger dc-link capacitor will lead to a decreased coupling effect according to the equations in (5.20) and (5.24). Compared with the impact on the coupling effect,

the dc-link capacitor has a noticeable impact on  $Z_{rh,rh}$  and  $Z_{gh,gh}$ . The results for  $Z_{gh,gh}$  are shown in Table 5-3. In this table, the calculated impedance with an infinite dc-link capacitance is compared to the simulated impedance of the GSC. Note that the coupling between RSC and GSC also disappears when the dc-link capacitance is infinite. There are large discrepancies between the simulated impedances and calculated impedances of the GSC. Therefore, the main impact of the dc-link is on the harmonic impedance of the GSC and RSC rather than the coupling between the GSC and RSC. But the impact of the dc-link capacitor will decrease when the dc-link capacitance increases. As shown in Table 5-4, the discrepancies between the simulated harmonic impedances and calculated impedances with an infinite dc-link capacitance are significantly decreased when the dc-link capacitor is increased to 10000 $\mu$ F. Although the above results show that the impact of the dc-link capacitor is not very significant, this research has quantified and clarified the degree of the impact of the dc-link on the DFIG harmonic responses. The findings will enable users to confidently model the DFIG with or without the inclusion of the dc-link capacitor.

Table 5-2 Comparison between the simulated impedances and calculated impedances of the GSC and RSC ( $Z_{gh,gh}$  and  $Z_{rh,rh}$ )

	Harmonic	Simulated impedance	Calculated impedance
<b>GSC</b>	3	0.8754 – 0.4792i	0.8327 – 0.5564i
	5	0.8470 – 0.2630i	0.8328 – 0.2359i
	7	0.8249 – 0.1991i	0.8327 – 0.1653i
<b>RSC</b>	3	0.6798-0.0200i	0.5961 - 0.1108i
	5	0.6617 - 0.0130i	0.5927 - 0.0145i
	7	0.6666 - 0.0089i	0.5871 - 0.0079i

Table 5-3 Impact of the dc-link capacitance on the harmonic impedance of the GSC with a dc-link capacitance of 2000 $\mu$ F

<i>Harmonic</i>	Simulated impedance	Calculated impedance with $C_{dc}=\infty$
3	0.8754 – 0.4792i	0.8329 – 0.0137i
5	0.8470 – 0.2630i	0.8329 – 0.0150i
7	0.8249 – 0.1991i	0.8328 – 0.0186i

Table 5-4 Impact of the dc-link capacitance on the harmonic impedance of GSC with a dc-link capacitance of 10000 $\mu$ F

<i>Harmonic</i>	Simulated impedance	Calculated impedance with $C_{dc}=\infty$
3	0.8388 – 0.0542i	0.8329 – 0.0137i
5	0.8368 – 0.0432i	0.8329 – 0.0150i
7	0.8357 – 0.0400i	0.8328 – 0.0186i

### 5.4.3 Significance of the GSC and RSC Block

The main contribution of this research is the harmonic model of the RSC and GSC unit. One of the most interesting findings is how significant is the RSC and GSC for the overall impedance of the DFIG. In Figure 5-9, the calculated impedances of the DFIG that exclude the GSC ( $Z_{gh,gh}=0$ ) or RSC ( $Z_{rh,rh}=0$ ) are compared with the full DFIG impedance. The difference is relatively small when RSC is excluded from the DFIG impedance, while the difference is more noticeable when GSC is excluded from the DFIG impedance. The reason is that, as shown in the final equivalent model in Figure 5-4, the RSC impedance is series-connected with the IG impedance. Since the IG impedance is much larger than the RSC impedance, the impact of the RSC is not obvious. However, the GSC is series-connected with the inductor  $L_g$ , and because  $L_g$  is not as large as the IG impedance, the GSC has a more obvious impact on the overall impedance. In summary, it is suggested that the GSC must be included in the harmonic model of the DFIG while the RSC might be omitted.

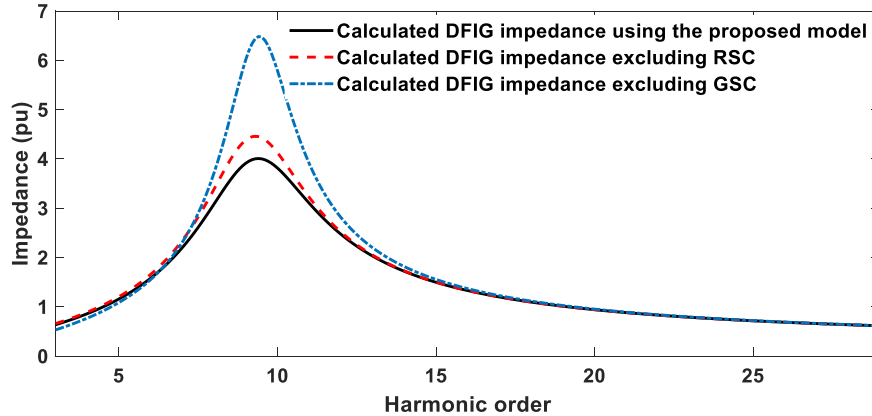
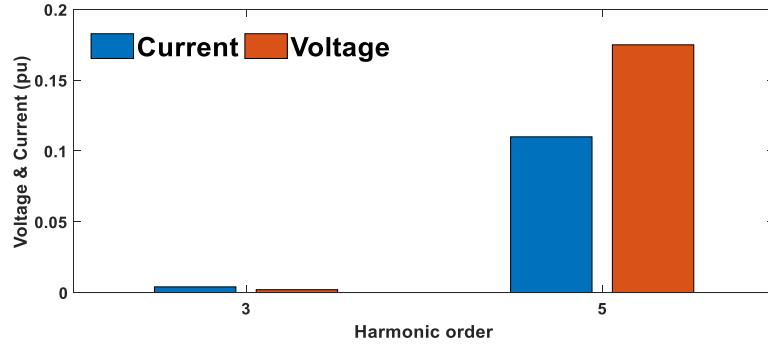


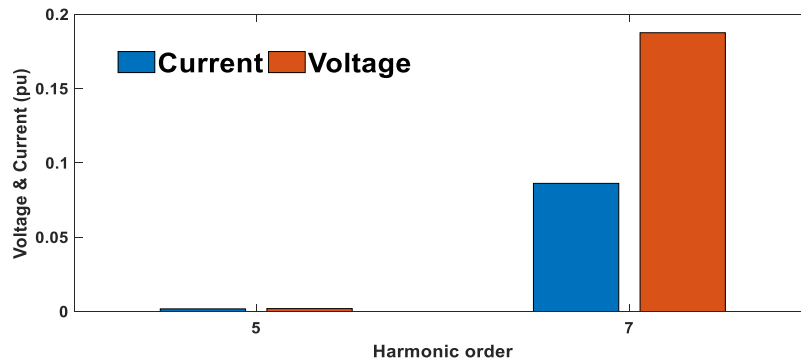
Figure 5-9 The degree of significance of the GSC and RSC impedances

#### 5.4.4 Strength of the Coupling Effect Between Different Harmonics

The results in Figure 5-7 were obtained when multiple harmonics were added to the ac source, but the simulated harmonic impedances match well with the theoretical results. This means that the coupling effect can be omitted. There are two reasons for this phenomenon. The first is that the coupling impedance is not significant inside the GSC and RSC. The second is that the induction generator and  $L_g$  do not have coupling effects that would reduce the coupling effect in the overall model of the DFIG. Figure 5-9 shows the harmonic spectra of the voltage and current at the entrance of the GSC branch when positive-sequence 5<sup>th</sup> and 7<sup>th</sup> harmonics existed in the connected system, which verifies the above analysis. The positive-sequence 5<sup>th</sup> and 7<sup>th</sup> harmonic did introduce coupled 3<sup>rd</sup> and 5<sup>th</sup> harmonics, respectively. This is consistent with the analysis in Section 5.3. Yet, the coupling effect is almost negligible inside the GSC, and the coupling effect for the overall DFIG is much smaller than that in the GSC. Therefore, the coupling effect can be omitted in most cases.



(a) harmonic spectrum when positive 5<sup>th</sup> harmonic is added



(b) harmonic spectrum when negative 7<sup>th</sup> harmonic is added

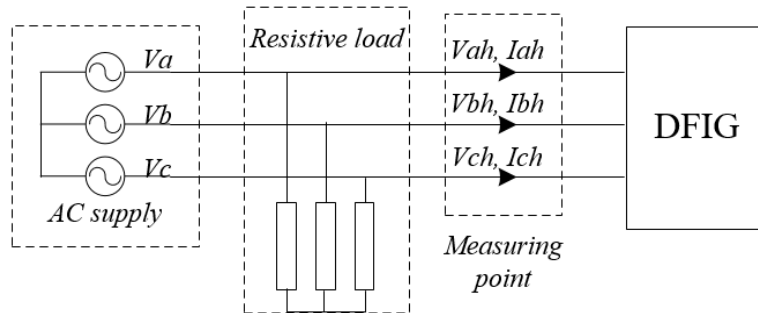
Figure 5-10 Coupling effect in the GSC

## 5.5 Model Verification Based on Lab Experiments

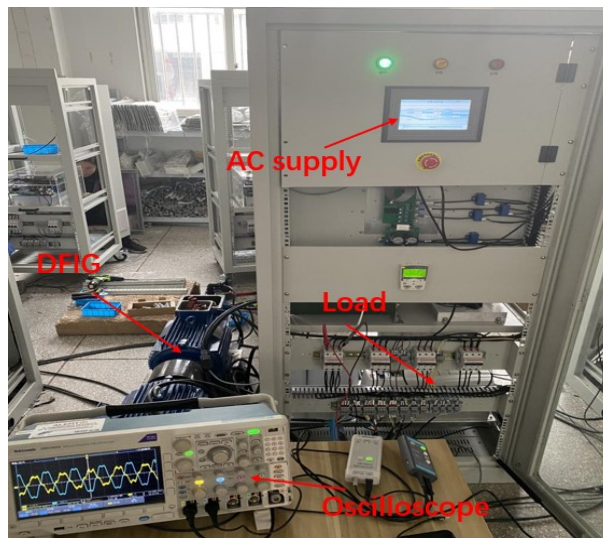
The main finding of this research, that the DFIG can be modeled using an impedance at low order harmonics, has also been verified using the lab experiments shown in Figure 5-11. In this test, a 3kW DFIG operating at its full rating was used. The internal parameters are unknown, so the DFIG is a black box seen from the grid side. Two types of tests were conducted: 1) Single 5<sup>th</sup>, 7<sup>th</sup>, or 11<sup>th</sup> harmonics of different IHDs were added to the AC source; 2) Multiple harmonics including 5<sup>th</sup>, 7<sup>th</sup>, and 11<sup>th</sup> harmonics of different IHDs were added to the AC source. The IHDs of different harmonics were up to 10%. The FFT algorithm was applied to the voltage and current waveforms measured at the PCC of the DFIG. Figure 5-11 showed the exemplary waveforms of the voltage and current at the PCC when the AC source contained 10% of the 5<sup>th</sup>, 7<sup>th</sup>, and 11<sup>th</sup> harmonics. The Fast Fourier

Transform (FFT) results of the voltage and current were used to compute the harmonic impedances. The experimental impedance results for all investigated cases are presented in Table 5-5. The results reveal the following key information:

- The impedance at one harmonic was almost constant regardless of the background harmonic distortion levels. This finding confirms that the DFIG equipment can indeed be modeled as an impedance at each harmonic frequency.
- The coupling effect between different harmonics was negligible. As shown in Table 5-5, the impedance at one harmonic was not affected when multiple harmonics were added.



(a) Schematic diagram of the experimental setup



(b) Experimental setup for the DFIG impedance measurement

Figure 5-11 Experimental test of the harmonic impedance of a VSC

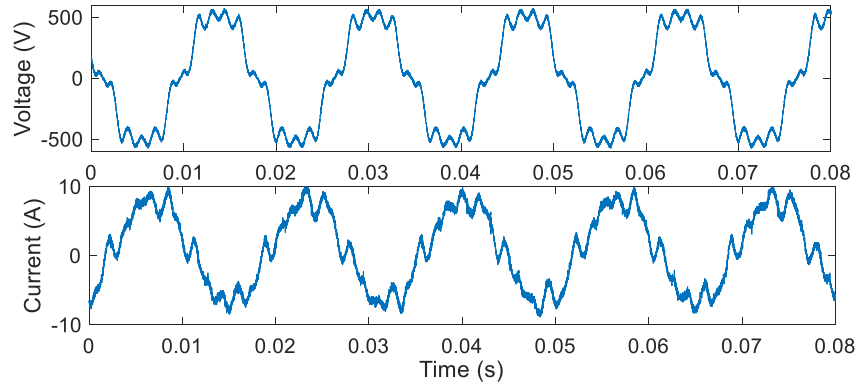


Figure 5-12 Recorded experimental waveforms of phase-A voltage and current at the PCC of the VSC inverter when the 10% 5<sup>th</sup>, 7<sup>th</sup> and 11<sup>th</sup> harmonics were added

Table 5-5 Measured phase-A impedance of a 3kW DFIG under different background harmonics

	IHD	5 <sup>th</sup>	7 <sup>th</sup>	11 <sup>th</sup>
Single harmonic	5%	54.8Ω	56.4Ω	69.1Ω
	10%	53.7Ω	56.8Ω	70Ω
Multiple harmonics	5%	54.1Ω	58Ω	69.4Ω
	10%	52.8Ω	55.2Ω	68.4Ω

The above lab experiments provide a practical approach to determine the harmonic model of the DFIG. In practice, the manufacturers might be reluctant to provide the control parameters or even the detailed control configurations. In such a situation, a measurement-based method can be used to determine the impedance. The measurement-based method takes into account the finding that the DFIG equipment behaves essentially as an impedance at the traditional harmonic frequencies. Thus, the impedance can be determined by simply using  $V_h/I_h$  at the PCC of the DFIG. The measurement method can be the lab experiments as described above or the field data after the DFIG is connected to a power system, taking advantage of the natural harmonic voltage and current at the PCC of the DFIG. Note that the field data-based procedure may require long-term monitoring of the harmonics since it needs abundant harmonics observed at the PCC.

## 5.6 Application of the Proposed Model of DFIG for Harmonic Power Flow Analysis

For this section, a 13-bus IEEE test system [68] was used to show the usefulness of the proposed model for harmonic power flow studies in power systems containing a DFIG, as shown in Figure 5-13. In this system, there is one DFIG at bus 4 and one LCC-based load at bus 7. The harmonic distortion was computed using both time-domain simulations and analytical harmonic power flow. For the time-domain simulations, the system in Figure 5-13 was modeled in Simulink/MATLAB. The DFIG was modeled following the configuration of the DFIG in Figure 5-1. The LCC-based load was a 6-pulse rectifier.

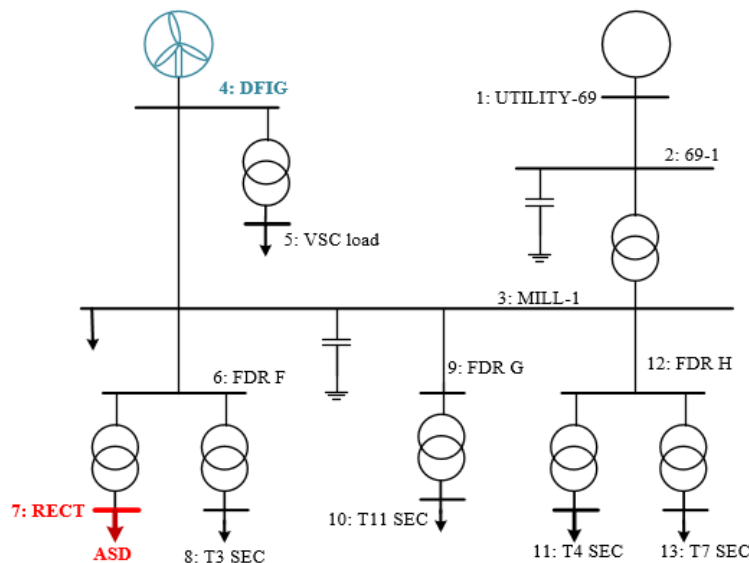


Figure 5-13 Studied system for harmonic power flow

Taking advantage of the developed DFIG model, a non-iterative harmonic power flow was proposed with the following steps:

- 1) Conduct fundamental frequency power flow in the power system by treating the line commutated converter (LCC)-equipment and the DFIG as constant power loads (PQ nodes). Based on the results, the harmonic model of all the components, as well as the harmonic models of the GSC and RSC, were computed. The DFIG and other components were linear and were represented by a harmonically

decoupled matrix as follows:

$$\begin{bmatrix} [I]_3 \\ [I]_5 \\ \dots \\ [I]_H \end{bmatrix} = \begin{bmatrix} [Y]_3 & 0 & \dots & 0 \\ 0 & [Y]_5 & \dots & 0 \\ \dots & \dots & \dots & \dots \\ 0 & 0 & \dots & [Y]_H \end{bmatrix} \begin{bmatrix} [V]_3 \\ [V]_5 \\ \dots \\ [V]_H \end{bmatrix} \quad (5.30)$$

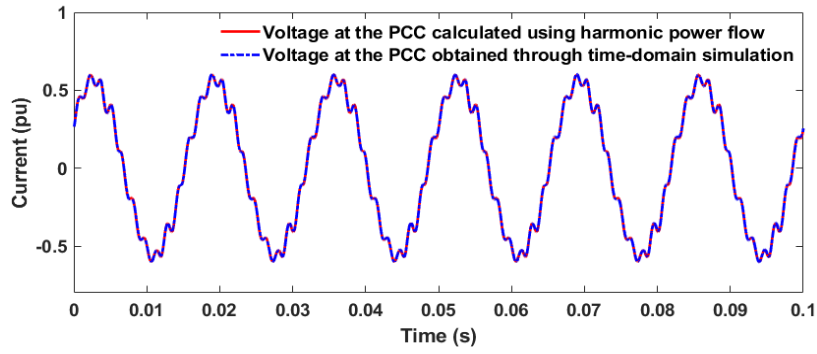
2) The LCC rectifier was modeled as a harmonic current source ( $I_7(H)$ ). The nodal harmonic current injection was expressed as  $I_{bus}(H)=[0,0,0,0,0,0,I_7(H),0,0,0,0,0]$ ;

3) Finally, the above equations were integrated to compute the harmonic voltage as

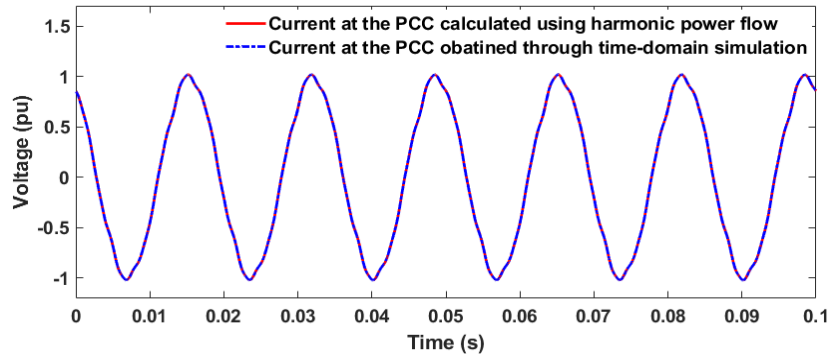
$$V_{bus}(H) = Y_H^{-1} I_{bus}(H) \quad (5.31)$$

where  $V_{bus}$  was the nodal harmonic voltage and  $H$  was the harmonic order of interest. Compared with the iteration-based harmonic power flow method, the harmonic power flow using the proposed model was easier to use.

To verify the usefulness of the developed model, the simulated harmonic voltage and current at the PCC (bus 2) were compared to the voltage and current at the PCC calculated using harmonic power flow. The results of the waveforms of the voltage and current were presented, as they simultaneously provided the magnitudes and angle information of the harmonics. The results are presented in Figure 5-14. The voltage and current at bus 4 where a DFIG is connected, are also presented in Figure 5-15, and the calculated results match with the simulated results as well. The calculated voltage and current at the PCC match perfectly with the simulated voltage and current at the PCC. To show the importance of the developed model, another harmonic power flow was conducted, but in this case, the GSC and RSC were excluded (i.e., only the IG and the inductor connected to the GSC were considered). The calculated spectrum of the current at the PCC was compared to the simulated results in Figure 5-16. When the GSC and RSC were not included, the error for the 5<sup>th</sup> harmonic current at the PCC reached 11%. This shows that the developed model is a meaningful tool to analyze harmonics accurately.

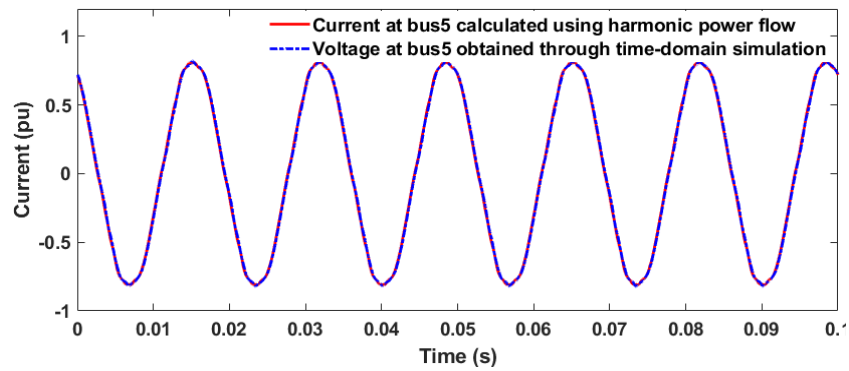


(a) Current waveform

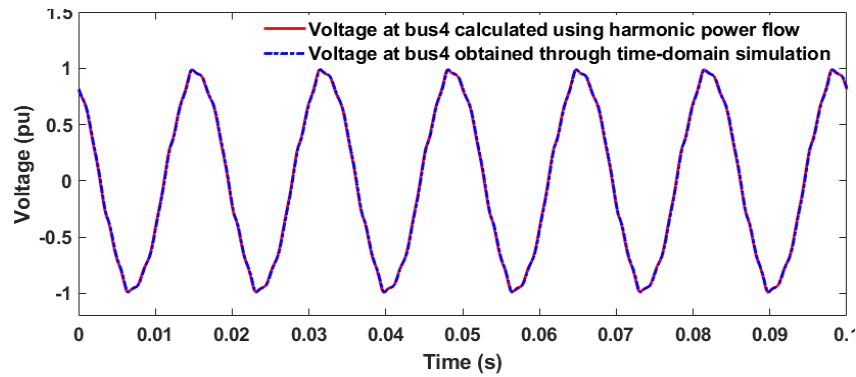


(b) Voltage waveform

Figure 5-14 Calculated and simulated phase-A voltage and current at the PCC



(a) Current waveform



(b) Voltage waveform

Figure 5-15 Calculated and simulated phase-A voltage and current at bus 5

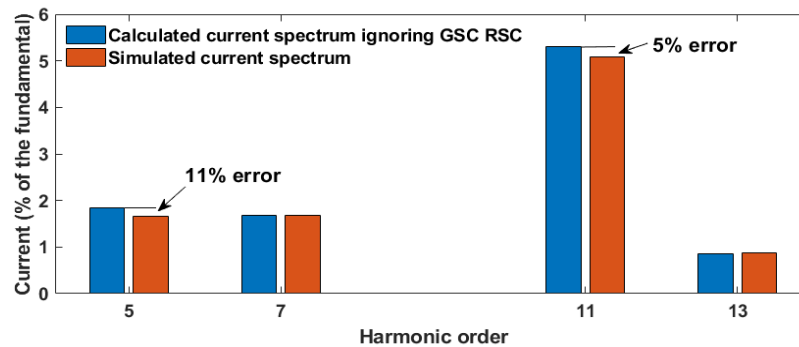


Figure 5-16 Comparison between the simulated current spectrum and the calculated spectrum ignoring the GSC and RSC

## 5.7 An Overall Procedure to Construct a Harmonic Model of the DFIG

Based on the impact and data availability of the three operating segments of a DFIG, the ideal procedure for constructing the harmonic model of the equipment is:

- First, the harmonic model must include the induction generator impedance and the front-end passive filter impedance. These two sections have the most contributions to the overall impedance of the DFIG. In this step, the model can be obtained by assuming the GSC and RSC as short circuits. This approach is very simple, but it may lead to a significant error for some harmonics.

- Second, the GSC and RSC impedance can be included by including the inner current control loop of the GSC and RSC. This requires knowing the  $H_2(s)$  transfer function in addition to the induction generator and the passive-filter parameters. Including the inner current control will make the VSC impedance model acceptable for many cases.
- Third, the harmonic model can include the impact of the power loop. This will lead to further refinement since the coupling between the GSC and RSC will be included. But this model requires knowing more internal parameters of the VSC equipment, and the final expression will be relatively complex.
- If no data is available, the measurement-based approach explained in 5.5 can be used to determine the parameters of the impedance model of a DFIG at the operating point of interest.

## 5.8 Summary

This chapter presents two contributions to the development of a harmonic model for DFIG units. The first is a proposal for a harmonic model of the combined RSC and GSC unit based on a rigorous analytical approach. The second is an actual DFIG model based on the proposal and sensitivity studies.

The combined RSC and GSC unit can be represented using a  $2 \times 2$  coupled impedance matrix. The results prove that the coupling between the RSC and GSC can be omitted under certain practical conditions if the dc-link capacitor is sufficiently large. The degree of coupling and the need to model it has been quantified using the proposed model.

The harmonic model of the DFIG unit is in the form of an impedance because the harmonic currents produced from various coupling mechanisms can be omitted. Equations to compute the model parameters have been established. The research shows that the RSC and GSC unit must be included in the harmonic model of the DFIG to maintain reasonable accuracy, and the GSC has a more noticeable impact than the RSC on the overall impedance. The proposed model is accurate and

effective for harmonic power flow studies, as verified using time-domain simulations. The impedance nature of the DFIG under harmonics was validated in lab experiments.

The proposed model fills in a gap in the modeling of renewable energy sources for harmonic studies. It establishes a technical foundation to upgrade the IEC report on the DFIG harmonic model.

## Chapter 6

### Harmonic Modeling of the VSC-HVDC for Power

#### System Harmonic Analysis

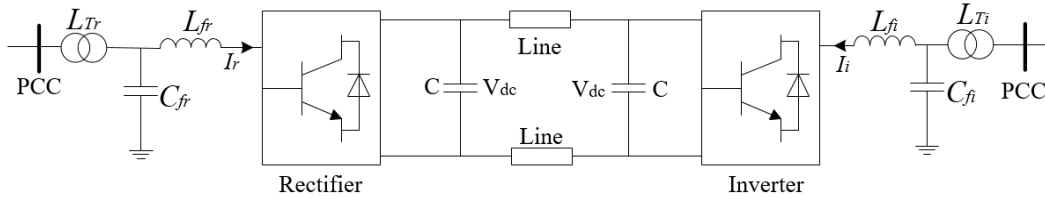
The voltage source converter (VSC) is now also used to construct a type of high-voltage DC (HVDC) transmission system called the VSC-HVDC [6]. This type of HVDC system has a number of advantages, including independent control of active and reactive power, fast control response speeds, and low filtering requirements. It is widely used in power systems. The VSC-HVDC contains two back-to-back VSCs: an inverter and a rectifier. The dc-link capacitors of these two VSCs are connected through a dc transmission line (or cable) [98]. The characteristics of the harmonic response of the VSC-HVDC are similar to those of the combined RSC and GSC unit analyzed in Chapter 5. There is a harmonic coupling effect between the back-to-back VSCs as well. Nevertheless, instead of sharing the same dc-link capacitor, the VSC terminal's dc-link capacitors are connected through the dc transmission line. As a result, the coupling characteristics are different from those of the back-to-back RSC and GSC. In this chapter, the harmonic characteristics of the VSC-HVDC, particularly the harmonic coupling characteristics on the dc-link, are analyzed in order to develop a model that can be used for harmonic analysis.

This chapter is organized as follows: Section 6.1 analyzes the harmonic response of the VSC-HVDC. Section 6.2 presents the derivation of the harmonic model of the VSC-HVDC. Section 6.3 shows the verification of the proposed model via time-domain simulations. Section 6.4 contains the chapter summary.

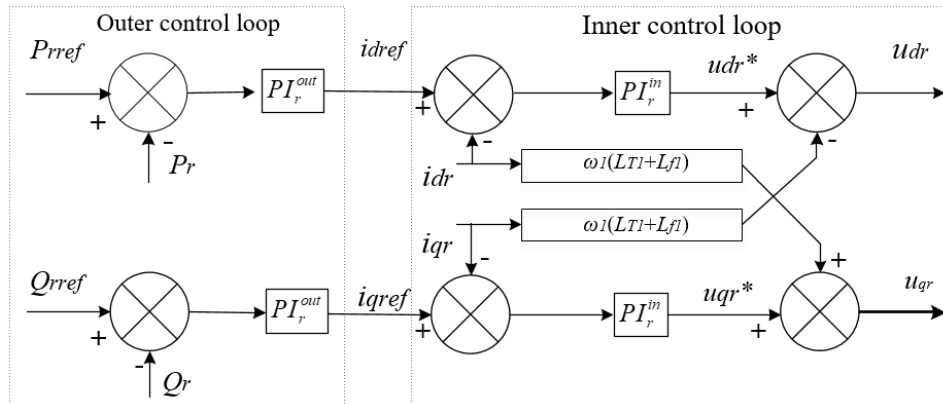
#### 6.1 Harmonic Response of the VSC-HVDC

The typical VSC-HVDC that contains two VSC terminals is shown in Figure 6-1 (a). One VSC terminal acts as the rectifier, controlling the active power and reactive

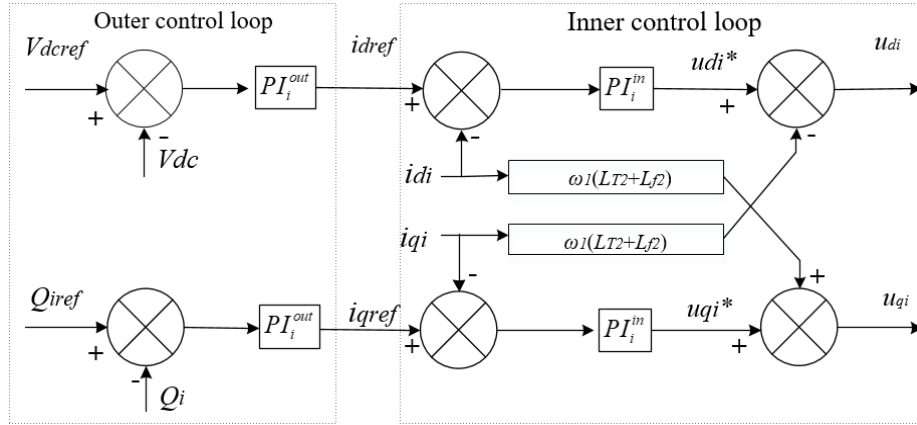
power on the ac side of the VSC established by controlling the VSC's ac side current, as shown in Figure 6-1 (b). The other VSC acts as the inverter, regulating the dc-link voltage and reactive power injected into the grid by the VSC by controlling the ac side current of the VSC, as shown in Figure 6-1 (c). The inner controllers of these two VSCs take the current on the ac side of the converter as the feedback current ( $I_r$  and  $I_i$  in Figure 6-1). On the ac side of each VSC, an LC filter is connected to attenuate the switching harmonics. But a transformer exists between the filter and the PCC, leading to an equivalent LCL filter between the converter and the PCC.



(a) Configuration of the VSC-HVDC



(b) Control of the VSC1



(c) Control of the VSC2

Figure 6-1 Structure of VSC-HVDC and the control diagram

The harmonic response of the VSC-HVDC is similar to that of the combined RSC and GSC unit studied in Chapter 5. But there are two major differences: 1) The two VSCs are connected through the dc transmission line, so the coupling feature is different; 2) The two VSC terminals are exposed to different grid harmonic sources, so the “two-terminal” equipment cannot be represented as a one-terminal impedance. Here, we will focus on the harmonic characteristics on the dc-link, which is shown in Figure 6-2. As seen in the figure, the harmonic on the ac side of both VSCs entering the dc side leads to harmonics on the ac side of the VSC ( $I_{rdch}$  and  $I_{idch}$ ). Instead of all of the current passing through the dc-link capacitor, the harmonic current will also pass through the dc transmission line, and the dc side harmonic currents from the two VSCs will be distributed as shown in Figure 6-2. The critical information is the harmonic ripple in the dc-link voltage, which is determined by the harmonic currents passing through the dc-link capacitor. According to this figure, a set of equations as (6.1) can be established to compute the harmonic currents of the dc-link capacitor.

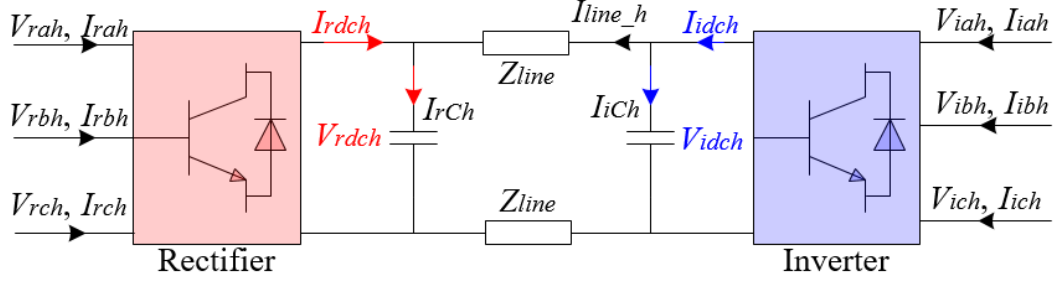


Figure 6-2 Harmonic characteristics on the dc side of the VSC-HVDC

$$\begin{aligned}
 I_{rdch} &= I_{rCh} - I_{line\_h} \\
 I_{idch} &= I_{iCh} + I_{line\_h} \\
 I_{line\_h} &= \frac{V_{idch} - V_{rdch}}{Z_{line}} = \frac{Z_C (I_{idch} - I_{rdch})}{Z_{line}}
 \end{aligned} \tag{6.1}$$

where “r” and “i” stand for rectifier and inverter, respectively;  $Z_C$  is the impedance of the dc-link capacitor;  $Z_{line}$  is the impedance of the dc transmission line. Solving the above equations results in harmonic current passing through the dc line as follows:

$$I_{line\_h} = \frac{Z_C (I_{idch} - I_{rdch})}{2Z_C + 2Z_{line}} \tag{6.2}$$

Accordingly, the harmonic current passing through the dc-link capacitor of the VSC can be written as

$$I_{rCh} = \frac{2Z_{line} + Z_C}{2Z_C + 2Z_{line}} I_{rdch} + \frac{Z_C}{2Z_C + 2Z_{line}} I_{idch} \tag{6.3}$$

$$I_{iCh} = \frac{2Z_{line} + Z_C}{2Z_C + 2Z_{line}} I_{idch} + \frac{Z_C}{2Z_C + 2Z_{line}} I_{rdch} \tag{6.4}$$

As shown in (6.3) and (6.4), the harmonic current passing through the dc-link capacitor comes from both the dc side of the inverter and the rectifier, leading to a coupling between two VSCs. Further, the coupling strength can be defined using the second term of (6.3) and (6.4), which is denoted as the coupling index shown

in (6.5)

$$K_{ri} = \frac{Z_C}{2Z_C + 2Z_{line}} \quad (6.5)$$

A larger  $K_{ri}$  means stronger coupling between the rectifier and the inverter.

## 6.2 Derivation of the Harmonic Model of VSC-HVDC

A full harmonic model of the VSC-HVDC is first presented in this section. Then the model is simplified based on practical considerations.

### 6.2.1 Harmonic Model of the VSC-HVDC

The harmonic model of the VSC-HVDC can be derived in the same way as that of the RSC and GSC unit in Chapter 5. The detailed derivations are not repeated here, and only the harmonics on the dc-link are illustrated. The current entering the dc side of the rectifier and the inverter can be written as (6.6) and (6.7), respectively.

$$\begin{aligned} i_{rdc} &= i_{ra}m_{ra} + i_{rb}m_{rb} + i_{rc}m_{rc} = \frac{3}{2}m_{r1}I_{r1} \cos(\alpha_{r1} - \delta_{r1}) \\ &+ \frac{3}{2}I_{r1} \left\{ \sum m_{rh+} \cos(\omega_{h+}t - \omega_1t + \alpha_{rh+} - \delta_{r1}) + \sum m_{rh-} \cos(\omega_{h-}t + \omega_1t + \alpha_{rh-} + \delta_{r1}) \right\} \\ &+ \frac{3}{2} \sum m_{r1}I_{rh+} \cos(\omega_{h+}t + \delta_{rh+} - \omega_1t - \alpha_{r1}) + \frac{3}{2} \sum_{x,y \in h+} m_{rx}I_{ry} \cos(\omega_xt - \omega_yt + \alpha_{rx} - \delta_{ry}) \\ &+ \frac{3}{2} \sum_{x \in h-, y \in h+} m_{ri}I_{rj} \cos(\omega_xt + \omega_yt + \alpha_{rx} + \delta_{ry}) + \frac{3}{2} \sum m_{r1}I_{rh-} \cos(\omega_{h-}t + \delta_{rh-} + \omega_1t + \alpha_{r1}) \\ &+ \frac{3}{2} \sum_{x \in h+, y \in h-} m_{rx}I_{ry} \cos(\omega_xt + \alpha_{rx} + \omega_yt + \delta_{ry}) + \frac{3}{2} \sum_{x \in h-, y \in h-} m_{rx}I_{ry} \cos(\omega_xt + \alpha_{rx} - \omega_yt - \delta_{ry}) \end{aligned} \quad (6.6)$$

$$\begin{aligned}
i_{idc} &= i_{ia}m_{ia} + i_{ib}m_{ib} + i_{ic}m_{ic} = \frac{3}{2}m_{i1}I_{i1} \cos(\alpha_{i1} - \delta_{i1}) \\
&+ \frac{3}{2}I_{i1} \left\{ \sum m_{ih+} \cos(\omega_{h+}t - \omega_1t + \alpha_{ih+} - \delta_{i1}) + \sum m_{ih-} \cos(\omega_{h-}t + \omega_1t + \alpha_{ih-} + \delta_{i1}) \right\} \\
&+ \frac{3}{2} \sum m_{i1}I_{ih+} \cos(\omega_{h+}t + \delta_{ih+} - \omega_1t - \alpha_{i1}) + \frac{3}{2} \sum_{x,y \in h+} m_{ix}I_{iy} \cos(\omega_x t - \omega_y t + \alpha_{ix} - \delta_{iy}) \\
&+ \frac{3}{2} \sum_{x \in h-, y \in h+} m_{ix}I_{iy} \cos(\omega_x t + \omega_y t + \alpha_{ix} + \delta_{iy}) + \frac{3}{2} \sum m_{21}I_{h-} \cos(\omega_{h-}t + \delta_{2h-} + \omega_1t + \alpha_{21}) \\
&+ \frac{3}{2} \sum_{x \in h+, y \in h-} m_{ix}I_{iy} \cos(\omega_i t + \alpha_{ix} + \omega_y t + \delta_{iy}) + \frac{3}{2} \sum_{x \in h-, y \in h-} m_{ix}I_{iy} \cos(\omega_x t + \alpha_{ix} - \omega_y t - \delta_{iy})
\end{aligned} \tag{6.7}$$

In (6.6) and (6.7), the terms that are induced by different harmonics can be omitted due to the small magnitudes. Based on the results in (6.6) and (6.7), the harmonic currents passing through the dc-link capacitors can be computed based on (6.3) and (6.4). Here we present only the derivation of the harmonic model of the rectifier. The derivation of the inverter can be addressed similarly. Substituting (6.6) and (6.7) into (6.3), the harmonic current passing through the dc-link capacitor of the inverter can be written as

$$\begin{aligned}
i_{rCh} &= \frac{3}{2}K_{11}I_{r1} \left\{ \sum m_{rh+} \cos(\omega_{h+}t - \omega_1t + \phi_{rh+} - \delta_{r1} + \xi_{11}) \right. \\
&\quad \left. + K_{11} \sum m_{rh-} \cos(\omega_{h-}t + \omega_1t + \phi_{rh-} + \delta_{r1} + \xi_{11}) \right\} \\
&+ \frac{3}{2}K_{11}m_{r1} \left\{ \sum I_{rh+} \cos(\omega_{h+}t + \delta_{rh+} - \omega_1t - \phi_{r1} + \xi_{11}) \right. \\
&\quad \left. + \sum I_{rh-} \cos(\omega_{h-}t + \delta_{rh-} + \omega_1t + \phi_{r1} + \xi_{11}) \right\} \\
&\frac{3}{2}K_{12}I_{i1} \left\{ \sum m_{ih+} \cos(\omega_{h+}t - \omega_1t + \phi_{ih+} - \delta_{i1} + \xi_{12}) \right. \\
&\quad \left. + \sum m_{ih-} \cos(\omega_{h-}t + \omega_1t + \phi_{ih-} + \delta_{i1} + \xi_{12}) \right\} \\
&+ \frac{3}{2}K_{12}m_{i1} \left\{ \sum I_{ih+} \cos(\omega_{h+}t + \delta_{ih+} - \omega_1t - \phi_{i1} + \xi_{12}) \right. \\
&\quad \left. + \sum I_{ih-} \cos(\omega_{h-}t + \delta_{ih-} + \omega_1t + \phi_{i1} + \xi_{12}) \right\}
\end{aligned} \tag{6.8}$$

where

$$K_{11} = \text{mag} \left\{ \frac{Z_C + 2Z_{line}}{2Z_C + 2Z_{line}} \right\}, \xi_{11} = \text{angle} \left\{ \frac{Z_C + 2Z_{line}}{2Z_C + 2Z_{line}} \right\}$$

$$K_{12} = \text{mag} \left\{ \frac{Z_C}{2Z_C + 2Z_{line}} \right\}, \xi_{12} = \text{angle} \left\{ \frac{Z_C}{2Z_C + 2Z_{line}} \right\}$$

“mag” and “angle” represent the magnitude and the angle. Based on the harmonic current passing through the dc-link capacitor, the corresponding dc-link voltage of the rectifier can be written as

$$\begin{aligned}
V_{rdc} = & V_{dc0} + \frac{3K_{11}I_{r1}}{2C(\omega_{h+} - \omega_1)} \sum m_{rh+} \cos(\omega_{h+}t - \omega_1t + \alpha_{rh+} - \delta_{r1} + \xi_{11} - \frac{\pi}{2}) \\
& + \frac{3K_{11}I_{r1}}{2C(\omega_{h-} + \omega_1)} \sum m_{rh-} \cos(\omega_{h-}t + \omega_1t + \alpha_{rh-} + \delta_{r1} + \xi_{11} - \frac{\pi}{2}) \\
& + \frac{3K_{11}m_{r1}}{2C(\omega_{h+} - \omega_1)} \sum I_{rh+} \cos(\omega_{h+}t + \delta_{rh+} - \omega_1t - \alpha_{r1} + \xi_{11} - \frac{\pi}{2}) \\
& + \frac{3K_{11}m_{r1}}{2C(\omega_{h-} + \omega_1)} \sum I_{rh-} \cos(\omega_{h-}t + \delta_{rh-} + \omega_1t + \alpha_{r1} + \xi_{11} - \frac{\pi}{2}) \\
& + \frac{3K_{12}I_{i1}}{2C(\omega_{h+} - \omega_1)} \sum m_{ih+} \cos(\omega_{h+}t - \omega_1t + \alpha_{ih+} - \delta_{i1} + \xi_{12} - \frac{\pi}{2}) \\
& + \frac{3K_{12}I_{i1}}{2C(\omega_{h-} + \omega_1)} \sum m_{ih-} \cos(\omega_{h-}t + \omega_1t + \alpha_{ih-} + \delta_{i1} + \xi_{12} - \frac{\pi}{2}) \\
& + \frac{3K_{12}m_{i1}}{2C(\omega_{h+} - \omega_1)} \sum I_{ih+} \cos(\omega_{h+}t + \delta_{ih+} - \omega_1t - \alpha_{i1} + \xi_{12} - \frac{\pi}{2}) \\
& + \frac{3K_{12}m_{i1}}{2C(\omega_{h-} + \omega_1)} \sum I_{ih-} \cos(\omega_{h-}t + \delta_{ih-} + \omega_1t + \alpha_{i1} + \xi_{12} - \frac{\pi}{2})
\end{aligned} \tag{6.9}$$

The above dc-link voltage is related to the ac-side voltage through the switching process of the rectifier, which is written as

$$V_{rah} = \{m_{ra} V_{rdc}\}_h = \{m_{ra}(t)[V_{dc0} + V_{rdch}]\}_h \tag{6.10}$$

Substituting (6.9) for (6.10) can lead to the following model:

$$\begin{bmatrix} V_{rh} \\ V_{ih} \end{bmatrix} = \begin{bmatrix} Z_{rh,rh} & Z_{rh,ih} \\ Z_{ih,rh} & Z_{ih,ih} \end{bmatrix} \begin{bmatrix} I_{rh} \\ I_{ih} \end{bmatrix} \tag{6.11}$$

And the first row of (6.11) can be written as

$$\begin{aligned}
\begin{bmatrix} V_{r3\pm} \\ V_{r5\pm} \\ V_{r7\pm} \\ \dots \\ V_{rh\pm} \end{bmatrix} &= \underbrace{\begin{bmatrix} Z_{r3\pm,r3\pm} & Z_{r3\pm,r5\pm} & 0 & 0 & \dots & 0 \\ Z_{r5\pm,r3\pm} & Z_{r5\pm,r5\pm} & Z_{r5\pm,r7\pm} & 0 & \dots & 0 \\ 0 & Z_{r7\pm,r5\pm} & Z_{r7\pm,r7\pm} & Z_{r7\pm,r9\pm} & \dots & 0 \\ \dots & \dots & \dots & \dots & \dots & 0 \\ 0 & 0 & 0 & 0 & \dots & Z_{rh\pm,rh\pm} \end{bmatrix}}_{Z_{rh,rh}} \begin{bmatrix} I_{r3\pm} \\ I_{r5\pm} \\ I_{r7\pm} \\ \dots \\ I_{rh\pm} \end{bmatrix} \\
&+ \underbrace{\begin{bmatrix} Z_{r3\pm,i3\pm} & Z_{r3\pm,i5\pm} & 0 & 0 & \dots & 0 \\ Z_{r5\pm,i3\pm} & Z_{r5\pm,i5\pm} & Z_{r5\pm,i7\pm} & 0 & \dots & 0 \\ 0 & Z_{r7\pm,i5\pm} & Z_{r7\pm,i7\pm} & Z_{r7\pm,i9\pm} & \dots & 0 \\ \dots & \dots & \dots & \dots & \dots & 0 \\ 0 & 0 & 0 & 0 & \dots & Z_{rh\pm,ih\pm} \end{bmatrix}}_{Z_{rh,ih}} \begin{bmatrix} I_{i3\pm} \\ I_{i5\pm} \\ I_{i7\pm} \\ \dots \\ I_{ih\pm} \end{bmatrix}
\end{aligned} \tag{6.12}$$

where

$$\begin{aligned}
Z_{rh\pm,rh\pm} &= \frac{-j3P_{nom}m_{r1}^2}{4V_{nom}^2 C(\omega_{h\pm} \mp \omega_1)} \\
&+ \left\{ \frac{H_d(s \mp j\omega_1)H_r(s \mp j\omega_1)}{\mp j(L_{T1} + L_{f1})\omega_1} \right\} \left\{ 1 + \frac{\sqrt{3}K_{11}P_{nom}m_{r1}I_{r1}e^{j(\delta_{r1} \mp \alpha_{r1} + \xi_{r1} - \frac{\pi}{2})}}{2\sqrt{2}V_{nom}V_{dc0} C(\omega_{h\pm} \mp \omega_1)} \right\}
\end{aligned} \tag{6.13}$$

$$\begin{aligned}
Z_{rh,rh\pm 2}^{\pm} &= \frac{3P_{nom}K_{11}m_{r1}^2 e^{j(\mp 2\alpha_{r1} + \xi_{11} - \frac{\pi}{2})}}{4V_{nom}^2 C(\omega_{h\pm} \mp \omega_1)} \\
&+ \frac{\sqrt{3}K_{11}P_{nom}m_{r1}I_{r1}e^{j(\mp \alpha_{r1} - \delta_{r1} + \xi_{11} - \frac{\pi}{2})}}{2\sqrt{2}V_{nom}V_{dc0} C(\omega_{h\pm} \mp \omega_1)} \left\{ \frac{H_d(s \mp j\omega_1)H_r(s \mp j\omega_1)}{\mp j(L_{T2} + L_{f1})\omega_1} \right\}
\end{aligned} \tag{6.14}$$

$$\begin{aligned}
Z_{rh,ih}^{\pm} &= \frac{3K_{12}P_{nom}m_{i1}m_{r1}e^{j(\pm \alpha_{r1} - \alpha_{i1} + \xi_{12} - \frac{\pi}{2})}}{4CV_{nom}^2 (\omega_{h\pm} \pm \omega_1)} \\
&+ \left\{ \frac{H_d(s \mp j\omega_1)H_r(s \mp j\omega_1)}{\mp j(L_{T1} + L_{f1})\omega_1} \right\} \left\{ \frac{\sqrt{3}K_{12}P_{nom}m_{r1}I_{i1}e^{j(\delta_{r1} \mp \alpha_{r1} + \xi_{12} - \frac{\pi}{2})}}{2\sqrt{2}V_{nom}V_{dc0} C(\omega_{h\pm} \mp \omega_1)} \right\}
\end{aligned} \tag{6.15}$$

$$Z_{rh,ih\pm 2}^{\pm} = \frac{3K_{12}P_{nom}m_{r1}^2 e^{j(\mp\alpha_{r1}\mp\alpha_{i1}+\xi_{12}-\frac{\pi}{2})}}{4V_{nom}^2 C(\omega_{h\pm}\mp\omega_1)} \quad (6.16)$$

$$+ \frac{\sqrt{3}K_{12}P_{nom}m_{r1}I_{i1} e^{j(\mp\alpha_{r1}+\delta_{r1}+\xi_{12}-\frac{\pi}{2})}}{2\sqrt{2}V_{nom}V_{dc0} C(\omega_{h\pm}\mp\omega_1)} \left\{ \begin{array}{l} H_d(s\mp j\omega_1)H_r(s\mp j\omega_1) \\ \mp j(L_{T2}+L_{f2})\omega_1 \end{array} \right\}$$

where  $L_{T1}$  and  $L_{T2}$  represent the equivalent inductances of the transformers, and  $H_r(s)$  is the PI regulator of the rectifier side. A similar equation can be developed for the inverter side. The above model has proved that the VSCs of the HVDC can be represented by a coupled impedance matrix, which includes coupling between two VSC terminals and coupling between different harmonics.

According to the above equations, the equivalent harmonic model of the VSC-HVDC can be represented using the circuit in Figure 6-3.

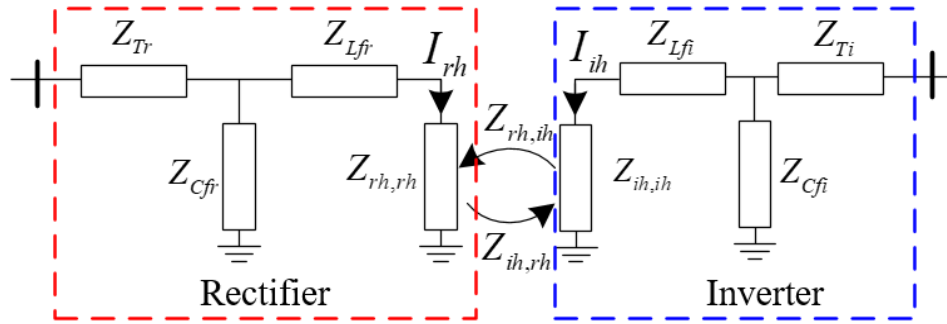


Figure 6-3 Equivalent circuit of VSC-HVDC

## 6.2.2 Simplified Model

Chapters 2 and 3 showed that the coupling between different harmonics in a VSC could be omitted, and in such cases, only the diagonal impedances in (6.12) need to be considered. Further, in practice, the control parameters of the rectifier and the inverter are identical and, as a result,  $Z_{rh,ih}=Z_{ih,rh}$ . Consequently, the harmonic model in (6.11) can be further changed to (6.17), and the VSC-HVDC can be represented using the circuit in Figure 6-4.

$$\begin{bmatrix} V_{rh} \\ V_{ih} \end{bmatrix} = \begin{bmatrix} Z_{rh,rh} - Z_{rh,ih} & 0 \\ 0 & Z_{ih,ih} - Z_{rh,ih} \end{bmatrix} \begin{bmatrix} I_{rh} \\ I_{ih} \end{bmatrix} + \begin{bmatrix} Z_{rh,ih} & Z_{rh,ih} \\ Z_{ih,rh} & Z_{rh,ih} \end{bmatrix} \begin{bmatrix} I_{rh} \\ I_{ih} \end{bmatrix} \quad (6.17)$$

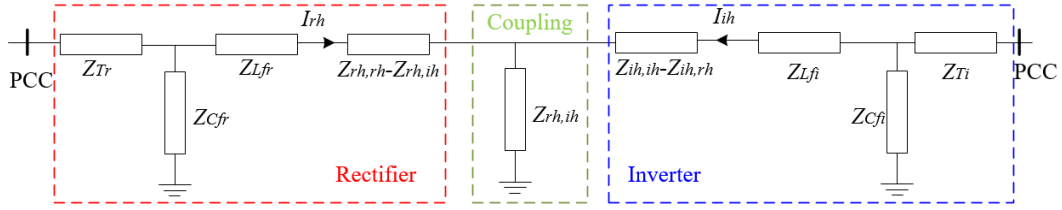


Figure 6-4 Equivalent impedance model of the VSC-HVDC

The circuit in Figure 6-4 presents the full harmonic model of the VSC-HVDC, which can be used for harmonic power flow analysis in the combined two ac systems connected to the VSC terminals. Yet, it is relatively complex to conduct harmonic power flow studies in the two ac systems when the coupling is included. Note that the coupling between the two VSCs is determined by the harmonic current passing through the dc transmission line, i.e., how the coupling impedance  $Z_{rh,ih}$  is compared with  $(Z_{Lfr}+Z_{rh,rh}-Z_{rh,ih})$ . If  $Z_{rh,ih} \ll (Z_{Lfr}+Z_{rh,rh}-Z_{rh,ih})$ , then the coupling strength can be omitted, and the two VSCs can be decoupled from the dc-link. Otherwise, the coupling should be included. As seen in (6.13) and (6.15) the coupling can be evaluated using the index  $K_{ri}$  ( $Z_{rh,ih} \approx K_{ri} \times Z_{rh,rh}$ ). Assuming that the harmonic current is the same on the ac sides of both the VSC terminals of the VSC-HVDC, the coupling effect will lead to a harmonic voltage of  $I_h Z_{rh,ih}$ . This coupling-introduced harmonic voltage can be ignored if it is smaller than 5%. If the criterion  $K_{ri} < 5\%$  is satisfied, the coupling effect between two VSC terminals can be omitted.

In practice, a long transmission line (or cable) is used, and the dc-link capacitor is selected as a relatively large value. Consequently, the impedance of the dc line ( $Z_{line}$ ) is usually much larger than the impedance of the dc-link ( $Z_C$ ), i.e.,  $Z_{line} \gg Z_C$ ,  $K_{11} \approx 1$ ,  $K_{12} \approx 0$ , and  $Z_{rh,ih} \approx 0$ . This means the harmonic current entering the dc side will mainly pass through the dc-link capacitor, and the harmonic current passing through the dc transmission line will be very limited. Under these conditions, the VSC-HVDC's rectifier and inverter can be decoupled from the dc-link (the dc transmission line can be regarded as an open circuit). As a result, the developed harmonic model for the three-phase VSC can be used for each terminal of the VSC-HVDC, i.e., the harmonic impedance of the rectifier can be written as

$$Z_{Rec} = \frac{(Z_{Lfr} + Z_{rh,rh})Z_{Cfr}}{Z_{Lfr} + Z_{rh,rh} + Z_{Cfr}} + Z_{Tr} \quad (6.18)$$

The harmonic impedance of the inverter can be written similarly. Therefore, the harmonic model of the VSC-HVDC can be drawn, as shown in Figure 6-5.

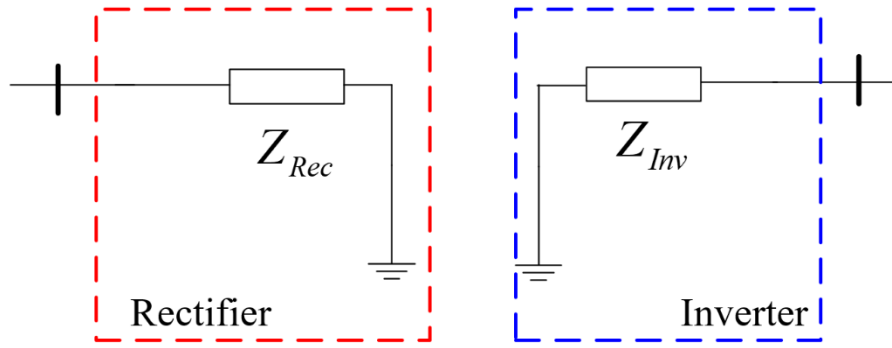


Figure 6-5 Simplified decoupled impedance model of the VSC-HVDC

### 6.3 Verification of the Proposed Model Via Time-Domain Simulations

This section describes how the above-simplified impedance model was verified using time-domain simulations.

#### 6.3.1 Verification of the Harmonic Impedance

The proposed harmonic model for the VSC-HVDC was verified using time-domain simulations in the system, as shown in Figure 6-6. The parameters are listed in Table 6-1. The calculated impedances using the model in (6.18) were compared to the simulated impedance. For the simulation, harmonics were added to the ac voltage source of the ac system connected to the rectifier, and the simulated impedance was obtained at the PCC of the rectifier. The comparison results are presented in Figure 6-7. The calculated results match well with the simulated results, which verifies that the proposed model can be used for the VSC-HVDC.

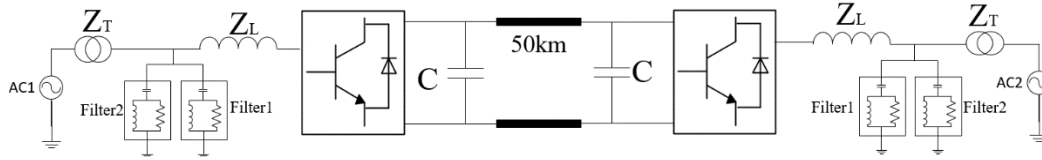


Figure 6-6 VSC-HVDC system for model verification

Table 6-1 Parameters of the VSC-HVDC

$H_1$	$k_p=3, k_i=3$	$H_2$	$k_p=0.6, k_i=6$
Transformer	230kV:100kV	$Z_L$	0.0015+0.15i (pu)
$Z_T$	0.005+0.15i (pu)	Filter1	Reactive power=14MW, $h_i=33, Q=15$
dc cable	0.0139+0.0599i (pu)	Filter2	Reactive power=22MW, $h_i=66, Q=15$

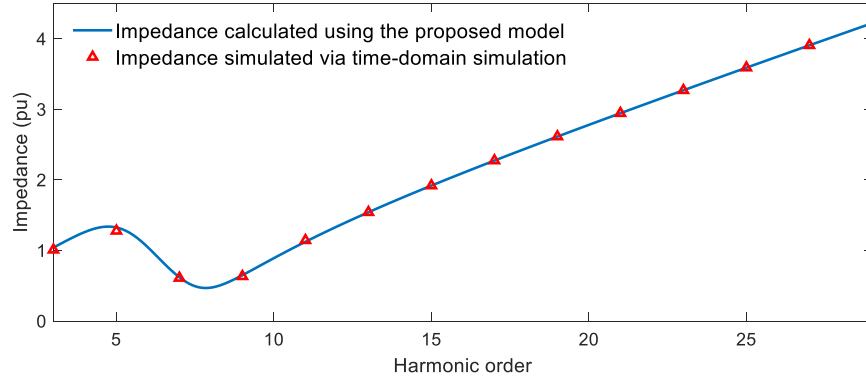


Figure 6-7 Comparisons between the calculated impedances and simulated impedances for the VSC-HVDC

### 6.3.2 Coupling Effect Between Two VSC Terminals

In the above calculation of the harmonic impedances, the coupling effect between these two VSCs was not included, and the simplified harmonic model was used. But the results show that the computed impedances still matched well with the simulated impedances. This means that the coupling between the two VSCs was very limited. To further validate the results, the impedance of the dc-link capacitor was compared with the impedance of the dc cable, as shown in Figure 6-8. The impedance of the dc cable is much larger than the impedance of the dc-link capacitor. The coupling index  $K_{ri}$  is also shown in this figure. The coupling index

is very small, so, the coupling between VSCs in the studied VSC-HVDC system can be omitted with confidence.

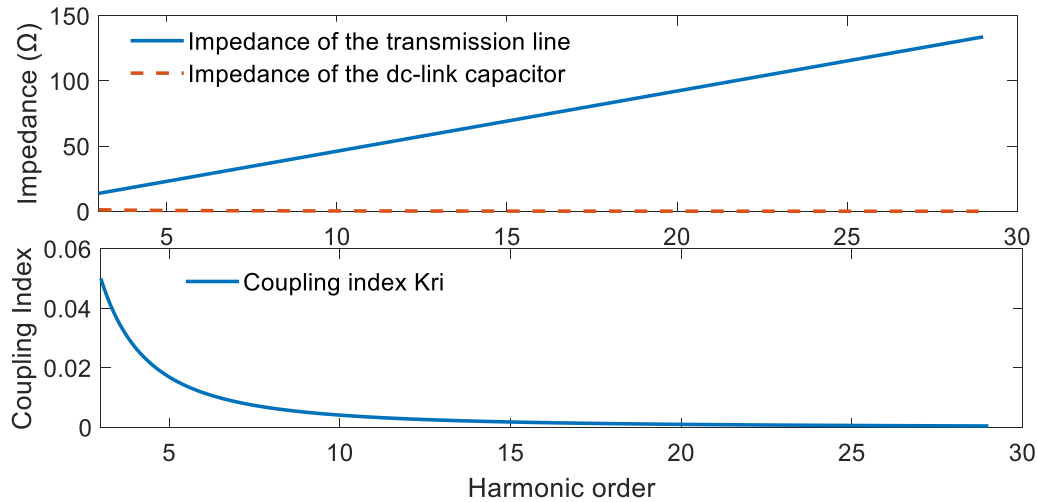


Figure 6-8 Comparison between the impedance of the dc cable and the impedance of the dc-link capacitor

## 6.4 An Overall Procedure to Construct the Harmonic Impedance Model of the VSC-HVDC

The VSC terminals of the VSC-HVDC can be constructed in the same way as those of the three-phase VSC. The detailed procedure can be summarized as follows:

- First, check if the criterion  $K_{ri} < 5\%$  is satisfied. If the criterion is satisfied, the two VSC terminals should be decoupled from the dc-link capacitor. If this criterion is not satisfied, the coupling needs to be included.
- Second, make sure to first include the front-end passive filter in the harmonic model of each VSC terminal of the VSC-HVDC.
- Third, to improve upon the above model, include the VSC's inner current control loop.
- To further refine the model, include the outer control loop and the power loop. This step requires knowing more internal parameters of the VSC equipment.
- If no data is available at all, determine the VSC impedance model using the measurement-based approach.

## 6.5 Summary

In this chapter, a harmonic model of the VSC-HVDC was proposed using mathematical derivations. The analysis of the harmonic response of the VSC-HVDC shows a coupling effect between two VSCs, which is determined by the impedances of the dc transmission line and the dc-link capacitor. According to the harmonic characteristics of the VSC-HVDC, a harmonic model of the VSC-HVDC was developed.

A practical approach was used to determine whether the coupling strength between two VSCs needed to be included: a long dc transmission line was used to connect two VSC terminals and a large dc-link capacitor was used to maintain the dc-link voltage. The harmonic current passing through the dc transmission line was quite small, which means that the coupling effect could be omitted with confidence, leading to a decoupled simplified harmonic model for each VSC terminal. The correctness of the simplified model for the VSC terminal was verified through time-domain simulations.

## Chapter 7

### Conclusions and Future Work

This chapter summarizes the main findings of the thesis and provides suggestions for future work.

#### 7.1 Thesis Conclusions and Contributions

This thesis has presented new analytical harmonic models of various types of VSC equipment that can be used for power system harmonic analysis. First, a harmonic model of a three-phase VSC was proposed for harmonic power flow studies. Then, the harmonic model of the three-phase VSC was extended to the single-phase VSC. Finally, harmonic models for the DFIG and VSC-HVDC for harmonic power flow studies were proposed.

The main conclusions and contributions of this thesis are summarized as follows.

- This thesis presents the analysis of the harmonic characteristics of the three-phase VSC at low-order harmonics. The harmonic features of the VSC were jointly determined by the control loop and power loop of the VSC. An analytical harmonic model of the three-phase VSC was then proposed through rigorous mathematical derivations. The final result showed that the three-phase VSC could be represented using a coupled impedance matrix at low-order harmonics. The coupling effect between different harmonics was induced by the outer control loop and power loop, which is not significant and can be omitted in practice. The three-phase VSC can be represented using an impedance at low-order harmonic frequencies. Time-domain simulations and lab experiments have demonstrated the correctness of the proposed model. Further, comparative studies show that the power loop (i.e., dc-link capacitor) has a more noticeable impact with a smaller dc-link capacitance. The application of the proposed model for harmonic power flow studies has also been validated using time-

domain simulations.

- This thesis also proposed an analytical harmonic model for a single-phase VSC at low-order harmonics. The harmonic model of the single-phase VSC for harmonics higher than the 3<sup>rd</sup> is similar to that of a three-phase VSC, which is in the form of a coupled impedance matrix. But the single-phase VSC also injects the 3<sup>rd</sup> harmonic into the grid, so it can be modeled as a Thevenin circuit at the 3<sup>rd</sup> harmonic. The degree of the 3<sup>rd</sup> harmonic depends on the size of the dc-link capacitor: a smaller dc-link capacitor yields a more noticeable 3<sup>rd</sup> harmonic. The correctness of the proposed model of the single-phase VSC was validated using extensive time-domain simulations and lab experiments. Additionally, considering the practical parameters of the single-phase VSC and the single-phase distribution systems, the 3<sup>rd</sup> harmonic produced in a practical single-phase PV system is proved to be quite limited.
- This thesis proposed the analytical models for the DFIG at low-order harmonics. For the harmonic modeling of the DFIG, the harmonic characteristics of the back-to-back RSC and GSC were analyzed using rigorous mathematical derivations. In addition to the harmonic characteristics of a three-phase VSC, there was a harmonic coupling between the back-to-back RSC and GSC. As a result, the back-to-back RSC and GSC were modeled using a coupled impedance matrix, which contained coupling between the RSC and GSC as well as coupling between different harmonics. The coupling between different harmonics was negligible, so a  $2 \times 2$  impedance matrix was used with confidence to represent the RSC and GSC unit. After integrating this new model with the linear harmonic model of the induction generator, an impedance model was obtained to represent the DFIG. The correctness of the proposed model was verified using time-domain simulations and lab experiments. Furthermore, extensive analyses have shown that the dc-link capacitor was critical to determining the coupling strength between the RSC and GSC. A larger dc-link capacitor led to a smaller coupling strength between the RSC and GSC. The application of the proposed model of the DFIG for harmonic power flow studies

was also validated.

- This thesis proposed a harmonic model for the VSC-HVDC at low-order harmonics. The results showed that there was also coupling between the two VSC terminals of the VSC-HVDC. However, due to the long-distance dc transmission line or cable, the coupling between the two VSC terminals was quite limited. As a result, the VSC terminals were decoupled in practice, and the harmonic model of the three-phase VSC was applied for each terminal of the VSC-HVDC.

## 7.2 Suggestions for Future Work

As with any study, something can always be done to extend the research. Several extensions and modifications of this thesis can be explored as follows:

- In Chapter 2 ~ Chapter 4, the research looked at the harmonic model of the VSC equipment with an outer control loop that regulates the active power, reactive power, and dc-link voltage. The results showed that these outer control loops were linear for harmonic studies. However, some VSC equipment may also apply the ac voltage (magnitude) regulation as the outer control loop, which might be nonlinear for harmonics. For this reason, effort should be made to extend the proposed harmonic model to the VSC equipment with ac voltage control.
- The harmonic modeling approaches for the VSC equipment can also potentially be used to model the VSC equipment under unbalanced conditions, which can be used to compute the noncharacteristic 3<sup>rd</sup> harmonic. In this research, both positive-sequence and negative-sequence fundamental frequency voltage and current were used to compute the 3<sup>rd</sup> harmonic. The main challenge was to compute the negative-sequence fundamental-frequency voltage and current using load flow studies. This research could be more meaningful for distribution systems where the unbalanced degree is generally more significant.

- The proposed harmonic models of different types of VSC equipment were developed with the assumption that the switching harmonics were not a concern. In practice, the switching frequency may be close to some low-order harmonics (e.g., 2kHz close to the 33<sup>rd</sup> harmonic). How the proposed model will be affected in such cases needs further investigation. And also, the switching frequency of VSC could be low when selective harmonic elimination (SHE) is used, how to model this type of VSC equipment is also interesting. Also, the superharmonics (2kHz~150kHz) introduced by PWM switching could also be investigated.
- The research work in this thesis focuses on harmonic models of VSC equipment. The harmonic model of VSC equipment can be further extended to the hybrid ac/dc systems where the diode-bridge rectifier, LCC converter, and VSC converter are jointly employed. For such research, more investigation is needed into how the connection of different types of converters affects the harmonic model.

## References

- [1] G. Séguier (Seguier) and F. Labrique, *Power Electronic Converters: DCAC Conversion*, New York:Springer-Verlag, 1993.
- [2] A. Yazdani and R. Iravani, *Voltage-Sourced Converter in Power Systems: Modelling, Control, and Application*. New York, NY, USA: Wiley, 2010.
- [3] S. Muller, M. Deicke and R. W. De Doncker, "Doubly fed induction generator systems for wind turbines," in *IEEE Industry Applications Magazine*, vol. 8, no. 3, pp. 26-33, May-June 2002.
- [4] M. Chinchilla, S. Arnaltes and J. C. Burgos, "Control of permanent-magnet generators applied to variable-speed wind-energy systems connected to the grid," in *IEEE Transactions on Energy Conversion*, vol. 21, no. 1, pp. 130-135, March 2006.
- [5] J. Smith et al., "Power quality aspects of solar power – results from CIGRE JWG C4/C6.29," in *CIGRE - Open Access Proceedings Journal*, vol. 2017, no. 1, pp. 809-813, 10 2017.
- [6] N. Flourentzou, V. G. Agelidis and G. D. Demetriades, "VSC-Based HVDC Power Transmission Systems: An Overview," in *IEEE Transactions on Power Electronics*, vol. 24, no. 3, pp. 592-602, March 2009.
- [7] B. Wu, *High-Power Converters and AC Drives*, Piscataway, NJ: IEEE Press, 2006, pp. 251-267.
- [8] Task Force on Harmonics Modeling and Simulation, "The modeling and simulation of the propagation of harmonics in electric power networks— Part I: Concepts, models and simulation techniques," *IEEE Trans. Power Del.*, vol. 11, no. 1, pp. 452–465, Jan. 1996.
- [9] W. Xu, J. E. Drakos, Y. Mansour, and A. Chang, "A three-phase converter model for harmonic analysis of HVDC systems," *IEEE Trans. Power Del.*, vol. 9, no. 3, pp. 1724–1731, Jul. 1994.
- [10] S. G. Jalali and R. H. Lasseter, "Harmonic interaction of power system with static switching circuits," in *Proc. 1991 IEEE Power Electronics Specialist Conf.*, pp. 330–337.
- [11] J. G. Mayordomo, L. F. Beites, R. Asensi, F. Orzaez, M. Izzeddine, and L. Zabala, "A contribution for modeling controlled and uncontrolled ac/dc converters in

- harmonic power flows,” *IEEE Trans. Power Del.*, vol. 13, no. 4, pp. 1501–1508, Oct. 1998.
- [12] L. Hu and R. Yacamini, “Harmonic transfer through converters and HVDC links,” *IEEE Trans. Power Electron.*, vol. 7, no. 3, pp. 514–525, Jul. 1992.
- [13] L. T. G. Lima, A. Semlyen, and M. R. Iravani, “Harmonic domain periodic steady state modeling of power electronics apparatus: SVC and TCSC,” *IEEE Trans. Power Del.*, vol. 18, no. 3, pp. 960–967, Jul. 2003.
- [14] IEEE task force on harmonics modeling and simulation.: ‘Harmonic analysis in frequency and time domain’, *IEEE Trans. Power Deliv.*, 2013, 28, (3), pp. 1813–1821.
- [15] Y. Sun, G. Zhang, W. Xu, and J. G. Mayordomo, “A harmonically coupled admittance matrix model for AC/DC converters,” *IEEE Trans. Power Del.*, vol. 22, no. 4, pp. 1574–1582, Oct. 2007.
- [16] K. Jalili and S. Bernet, "Design of LCL Filters of Active-Front-End Two-Level Voltage-Source Converters," in *IEEE Transactions on Industrial Electronics*, vol. 56, no. 5, pp. 1674-1689, May 2009.
- [17] J. Rodriguez, Jih-Sheng Lai and Fang Zheng Peng, "Multilevel inverters: a survey of topologies, controls, and applications," in *IEEE Transactions on Industrial Electronics*, vol. 49, no. 4, pp. 724-738, Aug. 2002.
- [18] H. Abu-Rub, J. Holtz, J. Rodriguez and G. Baoming, "Medium-Voltage Multilevel Converters—State of the Art, Challenges, and Requirements in Industrial Applications," in *IEEE Transactions on Industrial Electronics*, vol. 57, no. 8, pp. 2581-2596, Aug. 2010.
- [19] Hao Tian, “Harmonic Mitigation of Voltage Source Converter Based High-Power Variable Frequency Drives”, Ph.D. dissertation, University of Alberta, 2019.
- [20] F. Blaabjerg, R. Teodorescu, M. Liserre and A. V. Timbus, "Overview of Control and Grid Synchronization for Distributed Power Generation Systems," in *IEEE Transactions on Industrial Electronics*, vol. 53, no. 5, pp. 1398-1409, Oct. 2006.
- [21] M. Liserre, F. Blaabjerg and A. Dell’Aquila, "Step-by-step design procedure for a grid-connected three-phase PWM voltage source converter", *Int. J. Electron.*, vol. 91, no. 98, pp. 445-460, Aug. 2004.
- [22] R. N. Beres, X. Wang, M. Liserre, F. Blaabjerg and C. L. Bak, "A Review of Passive Power Filters for Three-Phase Grid-Connected Voltage-Source

- Converters," in IEEE Journal of Emerging and Selected Topics in Power Electronics, vol. 4, no. 1, pp. 54-69, March 2016.
- [23] J. Sun, "Dynamics and Control of Switched Electronic Systems – Chapter 2: Pulse-Width Modulation," Springer, 2012.
- [24] D. Neacsu, Power-Switching Converters: Medium and High Power, 2nd Ed, Boca Reaton, FL: CRC Press, 2014.
- [25] R. Torquato, G. R. Tessmer Hax, W. Freitas and A. B. Nassif, "Impact Assessment of High-Frequency Distortions Produced by PV Inverters," in IEEE Transactions on Power Delivery. doi: 10.1109/TPWRD.2020.3031375.
- [26] T. Joshi, G. Heydt, R. Ayyanar, "An Analysis Approach for the Assessment of PWM Carrier Frequency Spectral Components in Power Distribution Systems With Photovoltaic Resources," J. Electric Power Components and Systems, 2015.
- [27] C. F. Nascimento et al., "Analysis of Noncharacteristic Harmonics Generated by Voltage-Source Converters Operating Under Unbalanced Voltage," in IEEE Transactions on Power Delivery, vol. 32, no. 2, pp. 951-961, April 2017.
- [28] Wilsun Xu, Julio García-Mayordomo, "Electric energy systems : analysis and operation-chapter 11: Three-phase power flow and harmonic analysis", 2nd edition, Boca Raton: CRC Press, 2018.
- [29] T. S. Parker and L. O. Chua, Practical Numerical Algorithms for Chaotic Systems. Berlin, Germany: Springer-Verlag, 1989.
- [30] H. W. Dommel, "Digital computer solution of electromagnetic transients in single and multiphase networks," IEEE Trans. Power App. Syst., vol. PAS-88, no. 4, pp. 388–399, Apr. 1969.
- [31] A. Semlyen and A. Medina, "Computation of the periodic steady state in systems with nonlinear components using a hybrid time and frequency domain methodology," IEEE Trans. Power Syst., vol. 10, no. 3, pp. 1498–1504, Aug. 1995.
- [32] J. Guckenheimer and P. Holmes, Nonlinear Oscillations, Dynamical Systems, and Bifurcations of Vector Fields. Berlin, Germany: Springer-Verlag, 1997.
- [33] J. Segundo-Ramírez and A. Medina, "An enhanced process for the fast periodic steady state solution of nonlinear systems by poincaré map and extrapolation to the limit cycle," Int. J. Nonlinear Sci. Numer. Simulation, vol. 11, no. 8, pp. 661–670, Aug. 2010.
- [34] J. Segundo-Ramírez and A. Medina, "Computation of the steady-state solution of nonlinear power systems by extrapolation to the limit cycle using a discrete

- exponential expansion method,” *Int. J. Nonlinear Sci. Numer. Simulation*, vol. 11, no. 8, pp. 655–660, Aug. 2010.
- [35] T. N. Trick, F. R. Colon, and S. P. Fan, “Computation of capacitor voltage and inductor current sensitivities with respect to initial conditions for the steady-state analysis of nonlinear periodic circuits,” *IEEE Trans. Circuits Syst.*, vol. CAS-22, no. 5, pp. 391–396, May 1975.
- [36] T. J. Aprille and T. N. Trick, “A computer algorithm to determine the steady state response of nonlinear oscillators,” *IEEE Trans. Circuit Theory*, vol. 19, no. 4, pp. 354–360, Jul. 1972.
- [37] S. Herraiz, L. Sainz and J. Clua, "Review of harmonic load flow formulations," in *IEEE Transactions on Power Delivery*, vol. 18, no. 3, pp. 1079-1087, July 2003.
- [38] H. W. Dommel, A. Yan, and S. Wei, “Harmonics from transformer saturation,” *IEEE Trans. Power Syst.*, vol. PWRD-1, no. 2, pp. 209–214, Apr. 1986.
- [39] C. D. Callaghan and J. Arrillaga, “A double iterative algorithm for iterative harmonic analysis and harmonic flows at ac-dc terminals,” *Proc. Inst. Elect. Eng.*, vol. 136, no. 6, pp. 319–324, 1989.
- [40] D. Xia and G. T. Heydt, “Harmonic power flow studies, part I—Formulation and solution, part II—Implementation and practical application,” *IEEE Trans. Power App. Syst.*, vol. PAS-101, no. 6, pp. 1257–1270, Jun. 1982.
- [41] E. Acha, “Modelling of power system transformers in the complex conjugate harmonic space,” Ph.D. dissertation, Dept. Elect. Comput. Eng., Univ. Canterbury, Christchurch, New Zealand, 1988.
- [42] E. Acha, J. Arrillaga, A. Medina, and A. Semlyen, “General frame of reference for analysis of harmonic distortion in systems with multiple transformer nonlinearities,” *Proc. Inst. Elect. Eng. C*, vol. 136, no. 5, pp. 271–278, Sep. 1989.
- [43] W. Xu, J. R. Marti, and H. W. Dommel, “A multiphase harmonic load flow solution technique,” *IEEE Trans. Power Syst.*, vol. 6, no. 1, pp. 174–182, Feb. 1991.
- [44] J. Arrillaga, A. Medina, M. L. V. Lisboa, M. A. Cavia, and P. Sánchez, “The harmonic domain. A frame of reference for power system harmonic analysis,” *IEEE Trans. Power Syst.*, vol. 10, no. 1, pp. 433–440, Feb. 1995.
- [45] A. Semlyen and M. Shlash, “Principles of modular harmonic power flow methodology,” *Proc. Inst. Elect. Eng. C*, vol. 147, no. 1, pp. 1–6, Jan. 2000.

- [46] J. Usaola-García, "Steady state in power systems with nonlinear elements through a hybrid procedure of analysis in the time and frequency domains," (in Spanish) Ph.D. dissertation, Escuela Universitaria de Ingeniería Técnica Industrial, Univ. Politécnica Madrid, Madrid, Spain, 1990.
- [47] B. Wen, D. Dong, D. Boroyevich, R. Burgos, P. Mattavelli and Z. Shen, "Impedance-Based Analysis of Grid-Synchronization Stability for Three-Phase Paralleled Converters," in *IEEE Transactions on Power Electronics*, vol. 31, no. 1, pp. 26-38, Jan. 2016.
- [48] M. Cespedes and J. Sun, "Impedance Modeling and Analysis of Grid-Connected Voltage-Source Converters," in *IEEE Transactions on Power Electronics*, vol. 29, no. 3, pp. 1254-1261, March 2014.
- [49] Y. Wang, X. Wang, F. Blaabjerg and Z. Chen, "Harmonic Instability Assessment Using State-Space Modeling and Participation Analysis in Inverter-Fed Power Systems," in *IEEE Transactions on Industrial Electronics*, vol. 64, no. 1, pp. 806-816, Jan. 2017.
- [50] F. Wang, J. L. Duarte, M. A. M. Hendrix and P. F. Ribeiro, "Modeling and Analysis of Grid Harmonic Distortion Impact of Aggregated DG Inverters," in *IEEE Transactions on Power Electronics*, vol. 26, no. 3, pp. 786-797, March 2011.
- [51] Cespedes M and Sun J. Impedance Modeling and Analysis of Grid-Connected Voltage-Source Converters. *IEEE Transactions on Power Electronics*, 2014, 29(3): 1254-1261.
- [52] Vieto I and Sun J. Sequence Impedance Modeling and Analysis of Type-III Wind Turbines. *IEEE Transactions on Energy Conversion*, 2018,33(2): 537-545.
- [53] Y. Song and F. Blaabjerg, "Overview of DFIG-Based Wind Power System Resonances Under Weak Networks," *IEEE Transactions on Power Electronics*, vol. 32, no. 6, pp. 4370-4394, June 2017.
- [54] E Acha, M Madrigal, *Power System Harmonics: Computer Modeling and Analysis*, Wiley, 2001.
- [55] A. R. Wood and C. M. Osaukas, "A linear frequency-domain model of a STATCOM," in *IEEE Transactions on Power Delivery*, vol. 19, no. 3, pp. 1410-1418, July 2004.
- [56] C. Collins, N. Watson and A. Wood, "UPFC modeling in the harmonic domain," *IEEE Transactions on Power Delivery*, vol. 21, no. 2, pp. 933-938, April 2006.

- [57] G. Agundis-Tinajero et al., "Harmonic Issues Assessment on PWM VSC-Based Controlled Microgrids Using Newton Methods," in *IEEE Transactions on Smart Grid*, vol. 9, no. 2, pp. 1002-1011, March 2018.
- [58] K. L. Lian and P. W. Lehn, "Steady-state solution of a voltage-source converter with full closed-loop control," in *IEEE Transactions on Power Delivery*, vol. 21, no. 4, pp. 2071-2081, Oct. 2006.
- [59] J. J. Rico, M. Madrigal and E. Acha, "Dynamic harmonic evolution using the extended harmonic domain," in *IEEE Transactions on Power Delivery*, vol. 18, no. 2, pp. 587-594, April 2003.
- [60] J. R. C. Orillaza and A. R. Wood, "Harmonic state-space model of a controlled TCR," *IEEE Trans. Power Del.*, vol. 28, no. 1, pp. 197–205, Apr. 2013.
- [61] P. W. Lehn and K. L. Lian, "Frequency Coupling Matrix of a Voltage-Source Converter Derived From Piecewise Linear Differential Equations," in *IEEE Transactions on Power Delivery*, vol. 22, no. 3, pp. 1603-1612, July 2007.
- [62] F. Yahyaie and P. W. Lehn, "Using Frequency Coupling Matrix Techniques for the Analysis of Harmonic Interactions," in *IEEE Transactions on Power Delivery*, vol. 31, no. 1, pp. 112-121, Feb. 2016.
- [63] X. Zong, P. A. Gray and P. W. Lehn, "New Metric Recommended for IEEE Standard 1547 to Limit Harmonics Injected Into Distorted Grids," in *IEEE Transactions on Power Delivery*, vol. 31, no. 3, pp. 963-972, June 2016.
- [64] IEC 61400-21: 2008, Wind turbines-Part 21: Measurement and assessment of power quality characteristics of grid-connected wind turbines.
- [65] IEC TR 61400-21-3:2019 Wind energy generation systems - Part 21-3: Measurement and assessment of electrical characteristics - Wind turbine harmonic model and its application.
- [66] F. Blaabjerg, R. Teodorescu, M. Liserre and A. V. Timbus, "Overview of Control and Grid Synchronization for Distributed Power Generation Systems," in *IEEE Transactions on Industrial Electronics*, vol. 53, no. 5, pp. 1398-1409, Oct. 2006.
- [67] D. G. Holmes and T. A. Lipo, *Pulse Width Modulation for Power Converters: Principles and Practice*. Hoboken, NJ: Wiley, 2003, pp. 95–257.
- [68] Task Force on Harmonics Modeling and Simulation, "Test systems for harmonics modeling and simulation," in *IEEE Transactions on Power Delivery*, vol. 14, no. 2, pp. 579-587, April 1999.

- [69] S. B. Kjaer, J. K. Pedersen and F. Blaabjerg, "A review of single-phase grid-connected inverters for photovoltaic modules," in *IEEE Transactions on Industry Applications*, vol. 41, no. 5, pp. 1292-1306, Sept.-Oct. 2005.
- [70] S. Kumar and B. Singh, "Seamless Operation and Control of Single-Phase Hybrid PV-BES-Utility Synchronized System," in *IEEE Transactions on Industry Applications*, vol. 55, no. 2, pp. 1072-1082, March-April 2019.
- [71] Y. Yang, K. Zhou and F. Blaabjerg, "Current Harmonics From Single-Phase Grid-Connected Inverters—Examination and Suppression," in *IEEE Journal of Emerging and Selected Topics in Power Electronics*, vol. 4, no. 1, pp. 221-233, March 2016.
- [72] Y. Du, D. D. Lu, G. M. L. Chu and W. Xiao, "Closed-Form Solution of Time-Varying Model and Its Applications for Output Current Harmonics in Two-Stage PV Inverter," in *IEEE Transactions on Sustainable Energy*, vol. 6, no. 1, pp. 142-150, Jan. 2015.
- [73] J. H. R. Enslin and P. J. M. Heskes, "Harmonic interaction between a large number of distributed power inverters and the distribution network," *IEEE Trans. Power Electron.*, vol. 19, no. 6, pp. 1586–1593, Jun. 2004.
- [74] J. He, Y. W. Li, D. Bosnjak, and B. Harris, "Investigation and active damping of multiple resonances in a parallel-inverter-based microgrid," *IEEE Trans. Power Electron.*, vol. 28, no. 1, pp. 234–246, Jan. 2013.
- [75] H. Hu, Q. Shi, Z. He, J. He and S. Gao, "Potential Harmonic Resonance Impacts of PV Inverter Filters on Distribution Systems," in *IEEE Transactions on Sustainable Energy*, vol. 6, no. 1, pp. 151-161, Jan. 2015.
- [76] B. Liu et al., "Input Current Ripple and Grid Current Harmonics Restraint Approach for Single-Phase Inverter Under Battery Input Condition in Residential Photovoltaic/Battery Systems," in *IEEE Transactions on Sustainable Energy*, vol. 9, no. 4, pp. 1957-1968, Oct. 2018.
- [77] S. Jana and S. Srinivas, "An Approach to Mitigate Line Frequency Harmonics in a Single-Phase PV-Microinverter System," in *IEEE Transactions on Power Electronics*, vol. 34, no. 12, pp. 11521-11525, Dec. 2019.
- [78] S. Kan, X. Ruan, H. Dang, L. Zhang and X. Huang, "Second Harmonic Current Reduction in Front-End DC–DC Converter for Two-Stage Single-Phase Photovoltaic Grid-Connected Inverter," in *IEEE Transactions on Power Electronics*, vol. 34, no. 7, pp. 6399-6410, July 2019.

- [79] K. Ma, L. Tutulea, I. Boldea, D. M. Ionel, and F. Blaabjerg, "Power electronic drives, controls, and electric generators for large wind turbines—An overview," *Electr. Power Compon. Syst.*, vol. 43, no. 12, pp. 1406–1421, 2015.
- [80] P. Krause, *Analysis of Electric Machinery*, New York: McGraw-Hill, 1986.
- [81] L. Fan, S. Yuvurajan, and R. Kavasseri, "Harmonic analysis of a DFIG for a wind energy conversion system," *IEEE Trans. Energy Convers.*, vol. 25, no. 1, pp. 181–190, Mar. 2010.
- [82] S. A. Papathanassiou and M. P. Papadopoulos, "Harmonic analysis in a power system with wind generation," in *IEEE Transactions on Power Delivery*, vol. 21, no. 4, pp. 2006-2016, Oct. 2006.
- [83] E. Hernández and M. Madrigal, "A Step Forward in the Modeling of the Doubly-fed Induction Machine for Harmonic Analysis," in *IEEE Transactions on Energy Conversion*, vol. 29, no. 1, pp. 149-157, March 2014.
- [84] F. Ghassemi and K. Koo, "Equivalent Network for Wind Farm Harmonic Assessments," in *IEEE Transactions on Power Delivery*, vol. 25, no. 3, pp. 1808-1815, July 2010.
- [85] Uriel Vargas, Abner Ramirez, George Cristian Lazaroiu, "Flexible extended harmonic domain approach for transient state analysis of switched systems", *Electric Power Systems Research*, Volume 155, 2018.
- [86] M. Esparza, J. Segundo-Ramírez, J. B. Kwon, X. Wang and F. Blaabjerg, "Modeling of VSC-Based Power Systems in the Extended Harmonic Domain," in *IEEE Transactions on Power Electronics*, vol. 32, no. 8, pp. 5907-5916, Aug. 2017.
- [87] Y. Song and F. Blaabjerg, "Overview of DFIG-Based Wind Power System Resonances Under Weak Networks," *IEEE Transactions on Power Electronics*, vol. 32, no. 6, pp. 4370-4394, June 2017.
- [88] Hamed Ghanavati, Łukasz H. Kocewiak, Alireza Jalilian, Oriol Gomis-Bellmunt, "Transfer function-based analysis of harmonic and interharmonic current summation in type-III wind power plants using DFIG sequence impedance modeling", *Electric Power Systems Research*, Volume 199, 2021.
- [89] Zhaosen Chai, Hui Li, Xiangjie Xie, Mohamed Abdeen, Tian Yang, and Kun Wang, "Output impedance modeling and grid-connected stability study of virtual synchronous control-based doubly-fed induction generator wind turbines in weak grids, " in *International Journal of Electrical Power & Energy Systems*, Volume 126, Part A, 2021.

- [90] I. Vieto and J. Sun, "Sequence Impedance Modeling and Analysis of Type-III Wind turbines," in *IEEE Transactions on Energy Conversion*, vol. 33, no. 2, pp. 537-545, June 2018.
- [91] Marc Cheah-Mane, Luis Sainz, Eduardo Prieto-Araujo, and Oriol Gomis-Bellmunt, "Impedance-based analysis of harmonic instabilities in HVDC-connected Offshore Wind Power Plants," in *International Journal of Electrical Power & Energy Systems*, Volume 106, 2019.
- [92] Y. Xu, H. Nian, T. Wang, L. Chen and T. Zheng, "Frequency Coupling Characteristic Modeling and Stability Analysis of Doubly Fed Induction Generator," in *IEEE Transactions on Energy Conversion*, vol. 33, no. 3, pp. 1475-1486, Sept. 2018.
- [93] C. Zhang, X. Cai, M. Molinas, and A. Rygg, "Frequency-domain modelling and stability analysis of a DFIG-based wind energy conversion system under non-compensated AC grids: Impedance modelling effects and consequences on stability," *IET Power Electron.*, vol. 12, no. 4, pp. 907–914, 2019.
- [94] H. Nian, Y. Xu, L. Chen, and M. Zhu, "Modeling and analysis of DC-link dynamics in DFIG system with an indicator function," *IEEE Access*, vol. 7, pp. 125401–125412, 2019.
- [95] Yazhou Lei, A. Mullane, G. Lightbody and R. Yacamini, "Modeling of the wind turbine with a doubly-fed induction generator for grid integration studies," in *IEEE Transactions on Energy Conversion*, vol. 21, no. 1, pp. 257-264, March 2006.
- [96] Ahmed Rashad, Salah Kamel, Francisco Jurado, "Distributed generation systems: design, operation and grid integration – chapter 2: the basic principle of wind farms". London, England: Butterworth-Heinemann, 2017.
- [97] R. Cardenas, R. Pena, S. Alepuz and G. Asher, "Overview of Control Systems for the Operation of DFIGs in Wind Energy Applications," in *IEEE Transactions on Industrial Electronics*, vol. 60, no. 7, pp. 2776-2798, July 2013.
- [98] C. H. Chien and R. W. G. Bucknall, "Analysis of Harmonics in Subsea Power Transmission Cables Used in VSC–HVDC Transmission Systems Operating Under Steady-State Conditions," in *IEEE Transactions on Power Delivery*, vol. 22, no. 4, pp. 2489-2497, Oct. 2007.